Partial-wave analysis and spin observables of antiproton-proton scattering

Zhou, Daren

Partial-Wave Analysis and Spin Observables of Antiproton-Proton Scattering

This PhD project was carried out in the Kernfysisch Versneller Instituut according to the requirements of the Graduate School of Science (Faculty of Mathematics and Natural Sciences, University of Groningen).

PRINTED BY: Ipskamp Drukkers, Enschede, The Netherlands, February 2013

RIJKSUNIVERSITEIT GRONINGEN

Partial-Wave Analysis and Spin Observables of Antiproton-Proton Scattering

Proefschrift

ter verkrijging van het doctoraat in de
Wiskunde en Natuurwetenschappen
aan de Rijksuniversiteit Groningen
op gezag van de
Rector Magnificus, dr. E. Sterken,
in het openbaar te verdedigen op
vrijdag 15 maart 2013
om 14:30 uur

door

Daren Zhou

geboren op 7 oktober 1976
te Hunan, China

Promotor:	Prof. dr. R.G.E. Timmermans
Beoordelingscommissie:	Prof. dr. D. Boer
	Prof. dr. K. Jungmann
	Prof. dr. M. de Roo

ISBN printed version: 978-90-367-6095-9
ISBN electronic version: 978-90-367-6094-2

Contents

Chapter 1

Introduction

The antinucleon-nucleon ($\bar{N}N$) interaction is of fundamental interest and importance. It is related to the nucleon-nucleon (NN) interaction by charge conjugation (antinucleon-nucleon exchange). The study of the low-energy $\bar{N}N$ interaction can be used to test the low-energy effective theory (Chiral Perturbation Theory) of Quantum ChromoDynamics (QCD), which is part of the Standard Model (SM). At low energies, the degrees of freedom in QCD are not quarks and gluons, but baryons and mesons (and possibly some exotic states which are not yet understood well). In this thesis, we will focus on the low-energy antiproton-proton ($\bar{p}p$) scattering.

In the 1980s and the 1990s, there were several facilities for experiments on the $\bar{N}N$ interaction, for instance, the Low-Energy Antiproton Ring (LEAR) at CERN, Brookhaven National Laboratory (BNL) and FermiLab in USA, and KEK in Japan. Unfortunately, the study of antinucleon physics waned experimentally after the shutdown of LEAR in 1996.

At present, there are plans to revive antiproton (or antinucleon) physics also experimentally. For example, the PANDA (antiProton ANnihilation at DArmstadt) project [1] is going on which will be located at the Facility for Antiproton and Ion Research (FAIR) at GSI in Darmstadt, Germany. For the PANDA project, the antiproton beam momentum range in the laboratory frame is of 1.5 - 15 GeV/c which is about 0.8 - 14 GeV in kinetic energy of the antiproton beam. In this energy range, many particles can be produced, such as charmonium, glueballs, and $\bar{c}c$-glue hybrids. These states will give a lot of experimental information to test Chiral Perturbation Theory (ChPT) and Lattice QCD (LQCD). The spin dependence of

the $\bar{N}N$ interaction is of great interest as well. A polarized proton target (usually, it is a hydrogen target) can be realized, and some experimental data have been obtained for the $\bar{p}p$ interaction with a polarized proton target and an unpolarized antiproton beam. A polarized antiproton beam with high intensity (or luminosity) should be produced in order to do better experiments with a polarized antiproton beam and with an unpolarized/polarized proton target. However, this has not been realized so far. (A polarized antiproton beam with low intensity has been produced by FermiLab through the decay of $\bar{\Lambda}$ and the laboratory momentum of the antiproton beam is 185 MeV/c [2]. The measurement of the difference in the total cross section for antiparallel and parallel longitudinal spins has been done with the antiproton beam at the laboratory momentum of 200 MeV/c [3].) The PAX (Polarized Antiproton eXperiments) collaboration has proposed experiments on the polarization of antiproton beams in the low-energy Antiproton Polarizer Ring (APR) at FAIR [4] (the beam laboratory momentum can reach 15 GeV/c in the High Energy Storage Ring (HESR) at FAIR) and in the Antiproton Decelerator ring (AD-ring) at CERN [5] where the beam kinetic energy range is 50 - 450 MeV or about 0.3 - 1 GeV/c in momentum in the laboratory frame. Till now, most of the spin data obtained are the analyzing power (the target is polarized, whereas the spins of the scattered and recoil particles are not measured), depolarization (the target is polarized and the spins of the recoil particles are measured) and very limited spin-transfer (the target is polarized and the spins of the scattered particles are measured) data. (For details of the definitions of these observables and some others, see Chapter 5.) Once the polarization of an antiproton beam can be obtained, more spin observables can be measured, for example the spin-correlation parameters (the beam and target are both polarized, whereas the spins of the scattered and recoil particles are not measured, or the beam and target are both unpolarized, whereas the spins of the scattered and recoil particles are measured) and the higher rank spin-tensors (the spins of three or all four particles, namely beam, target, scattered, and recoil particles, are measured). These spin observables can be used to select a better model out of several models which are used to describe the $\bar{p}p$ interaction. The double-polarized $\bar{p}p$ Drell-Yan process can be used to measure the quark or gluon transversity inside a transversely polarized (anti)proton. Moreover, there might appear some unexpected phenomena by studying the double-polarized $\bar{p}p$ interaction.

The $\bar{N}N$ interaction is more complicated than the NN interaction because it has many annihilation processes and also the (generalized) Pauli principle does not apply, though the $\bar{N}N$ interaction has a close relation with the NN interaction. To

see this, let us count how many phase-shift parameters (including mixing parameters) one needs in a single-energy partial-wave analysis (PWA) for the NN case and for the $\bar{N}N$ case, respectively. In the pp case, the Pauli principle applies and the total isospin is 1 ($\ell + s$ must be even, where ℓ is the orbit angular momentum and s is the total spin). For the total angular momentum $J = 0$, one needs 2 real parameters (for $^1S_0$ and $^3P_0$). For $J = 1$, one needs 1 real parameter (for $^3P_1$); for $J = 2$, one needs 4 real parameters (for $^1D_2$, $^3P_2$, and $^3F_2$); and so on. For each odd $J > 0$ one needs 1 real parameter and for each even $J > 0$ one needs 4 real parameters. Therefore, one needs 2.5 real parameters on average for each $J > 0$. In the np case, the Pauli principle does not apply and the total isospin can be either 0 or 1. For $J = 0$, one needs in total 4 real parameters (for $^1S_0$ and $^3P_0$). For $J = 1$, one needs in total 10 real parameters (for $^1P_1$, $^3P_1$, $^3S_1$, and $^3D_1$); for $J = 2$, one needs in total 10 real parameters (for $^1D_2$, $^3D_2$, $^3P_2$, and $^3F_2$) as well; and so on. Therefore, for each $J > 0$, one needs in total 10 real parameters. If the generalized Pauli principle (including isospin) is used, the number of parameters for each J is reduced by a factor of 2. In the $\bar{N}N$ case, because of the annihilation, all phase-shift parameters become complex, and thus one needs total 8 real parameters for $J = 0$ and 20 real parameters for each $J > 0$. Because too many phase-shift parameters need to be determined at one energy, single-energy PWAs are no longer done for NN. Instead, multi-energy or energy-dependent PWAs are preferred, both for NN and for $\bar{N}N$ scattering.

Lots of work has been done for NN scattering experimentally and theoretically. There are a few models for the low-energy NN interaction that have been used also as the basis for an $\bar{N}N$ model. In particular, the Paris NN model [6–9], the Nijmegen NN model [10], and the Bonn NN model [11]. We will say something about these NN models very briefly here as examples. The Paris NN model contains one-meson (π, ω) exchanges and 2π-exchange. Dispersion relations are used in this model, into which some knowledge from the pion-nucleon interaction and the pion-pion interaction are used as inputs. The short-range potential is described by a phenomenological soft-core (which means the potential is not infinite which is contrast to a hard core which has an infinite potential at some range) in this model. In the Nijmegen NN model, Regge-pole theory is used and the trajectories include the traditional one-boson (π, η, η', ρ, ϕ, ω, δ, ...) exchanges and also the Pomeron, f, f', and A_2. Exponential form factors are used in this model. The Bonn NN model contains the one-meson (π, ρ, ω, δ) exchanges, two-meson ($\pi\pi$, $\pi\rho$, $\pi\omega$) exchanges, 3π exchanges, and other effective 4π exchanges. Virtual Δ-isobars are included as well. Form factors are also used in this model, given by

a conventional monopole form. In this model, the Hamiltonians are treated in an "old-fashioned" perturbation theory [12–14]. All of these three NN models can fit experimental data well with more or less parameters.

The $\bar{N}N$ interaction, as mentioned before, is more complicated, however. The dominant feature (hadronic part) of $\bar{N}N$ scattering at low energy is the annihilation into mesons, a complex multiparticle process that is difficult to model. In pre-LEAR days, some qualitative understanding was obtained by using simplified prescriptions, such as a simple absorptive boundary condition [15–17] or a state-independent two- or three-parameter optical potential (which just means that the potential has an imaginary part) [18–26]. These models can describe the integrated total, annihilation, and charge-exchange cross sections, but not the differential observables. Motivated by the experiments at LEAR, more sophisticated $\bar{N}N$ models were developed in order to attempt a more quantitative fit to the data. Examples are the Paris $\bar{N}N$ (optical-potential) model [27–32], the Nijmegen $\bar{N}N$ (coupled-channels) model [33, 34], and the Pittsburgh $\bar{N}N$ (coupled-channels) model [35].

Here, we will discuss briefly the Paris $\bar{N}N$ model, the Nijmegen $\bar{N}N$ model, and the Jülich $\bar{N}N$ models [24–26, 36, 37] (which have been developed from the Bonn NN model). For the Paris $\bar{N}N$ model, an optical potential is used. The long- (and intermediate-) range ($r \geq 1$ fm) real parts of the optical potential are obtained by the G-parity transformation (which is a combination of charge conjugation and a rotation in isospin space, for details, see Section 2.3) [38–40] of the corresponding Paris NN potentials, while the short-range ($r < 1$ fm) real part is treated phenomenologically. The form of the imaginary part of the optical potential is suggested by the $\bar{N}N$ annihilation into two mesons or resonances. The imaginary part is of short range and depends on the energy and state, and is treated phenomenologically as well. The Nijmegen $\bar{N}N$ model is a phenomenological coupled-channels model. The long-range ($r \geq 0.63$ fm) nuclear part of the diagonal part of the potential is obtained by the G-parity transformation of the Nijmegen-model-D potential [41] and the short-range ($r < 0.63$ fm) part is a modification of the Nijmegen-model-D potential. A phenomenological potential is added to the diagonal part of the potential. The off-diagonal parts of the potential are also phenomenological which describe effective annihilation channels. The Jülich group has developed several $\bar{N}N$ models. The two better models among these Jülich $\bar{N}N$ models are the Jülich model A(BOX) [25] and the Jülich model D [26]. For the Jülich model A(BOX), the elastic part of the potential is obtained by the G-parity transformation of the corresponding parts of the Bonn NN potential, whereas the annihilation part is parametrized by a phenomenological optical potential of Gaussian form and

state- and energy-independent. The Jülich model D has the same elastic potential as that of the Jülich model A(BOX). In the Jülich model D, however, the annihilation potential has two different parts. One part of the annihilation potential is described microscopically and includes not only annihilations into pseudoscalar mesons (π, η, K) but also annihilations into all possible combinations of the light mesons with quantum numbers 0^{++}, 1^{--}, 1^{++}, and 2^{++}. The other part of the annihilation potential is also treated phenomenologically and is similar to that of the Jülich model A(BOX) but has only an imaginary part. With the parameters fitted by experimental data, all of these $\bar{N}N$ models discussed above can generally agree with the integrated observables. As for the differential observables (for example, analyzing powers), the Nijmegen $\bar{N}N$ model and the Paris $\bar{N}N$ model give a better fit.

As mentioned before, there were several facilities which worked on the experiments of the $\bar{p}p$ scattering. However, major steps forward were taken at LEAR in the 1980s and the early 1990s. For the first time, good-quality data became available for the total cross section and the total annihilation cross section as functions of antiproton laboratory momentum ($p_{\rm lab}$), for the analyzing power in antiproton-proton elastic scattering ($\bar{p}p \to \bar{p}p$), and for the differential cross section and analyzing power in charge-exchange scattering ($\bar{p}p \to \bar{n}n$) at antiproton momenta above about 200 MeV/c.

In Refs. [42–44] an energy-dependent PWA of all $\bar{p}p$ scattering data below $p_{\rm lab} = 925$ MeV/c was developed, in order to arrive at a model-independent description of the $\bar{N}N$ interaction. Also, as compared with a single-energy PWA, an energy-dependent PWA "averages" statistical fluctuations over the whole energy range considered. The method of analysis is adapted from the famous Nijmegen PWAs of the pp and np scattering data [45–49]*. These PWAs exploit as much as possible our knowledge about the interaction in the description of the energy dependence of the scattering amplitudes. The long-range interactions, which are responsible for the rapid energy variations of the amplitudes, are included exactly in the relativistic (means with relativistic kinematics) Schrödinger equation, while the slow energy variations due to the essentially unknown short-range interactions are parametrized phenomenologically by an energy-dependent boundary condition at some radius $r = b$. In this way, an economic and model-independent high-quality description of the scattering database is possible. In the $\bar{p}p$ case [42–44], one assumes that the long-range potential is given by the charge-conjugated version of the corresponding nucleon-nucleon potential, and, by implementing a complex boundary condition,

*H. A. Bethe, (Centennial review of) *Nuclear physics*, Rev. Mod. Phys. **71**, S6 (1999).

one bypasses with this strategy as well our lack of knowledge of the short-range annihilation dynamics.

In this thesis, a new energy-dependent PWA of $\bar{p}p$ scattering is presented [50, 51]. There are two important reasons to do this. The first and perhaps main motivation is the renewed experimental interest in $\bar{p}p$ scattering, as mentioned before. The second reason is theoretical and is motivated by the progress reached in the last two decades or so in the understanding of the NN interaction within the framework of chiral effective field theory. In the long-range strong (nuclear) part of the NN interaction, the contributions from the pion exchanges are important. The pions (among others) are the (pseudo-) Goldstone bosons from the spontaneous symmetry breaking of the chiral $SU(3,L) \otimes SU(3,R)$ symmetry. They have nonzero masses because the chiral $SU(3,L) \otimes SU(3,R)$ symmetry is also explicitly broken. The way to construct phenomenological chiral Lagrangians has been presented by Weinberg [52, 53] in the $SU(2,L) \otimes SU(2,R)$ case (this procedure was generalized to arbitrary groups by other authors [54, 55]) and has been used to study nuclear forces [48, 56–61]. In particular, the PWAs of the pp and np scattering data have been updated by including, next to the electromagnetic and the one-pion exchange (OPE) potential, the long-range parts of the chiral two-pion exchange (TPE) potential [48, 49], instead of the phenomenological heavy-boson exchanges of the Nijmegen potential [10, 62], thereby improving even more the model independence and the quality of the NN PWAs of Refs. [45–47]. Motivated by that success, we include here as well the charge-conjugated TPE potential in the long-range $\bar{N}N$ interaction, instead of the phenomenological charge-conjugated heavy-boson exchanges that were used in Ref. [43].

At the same time, we take the opportunity to update the database of $\bar{p}p$ scattering data. The database constructed in Ref. [43] includes all scattering data published in a regular physics journal up to early 1993. A number of high-quality data sets from LEAR became available only later, in particular differential cross sections and analyzing powers for the charge-exchange reaction $\bar{p}p \to \bar{n}n$. Also the first measurements of the depolarization and spin-transfer observables for $\bar{p}p \to \bar{n}n$ were published only later. These data sets can be included now and they provide significant new constraints on the PWA solution.

Higher-rank spin observables are of interest and importance to study the spin dependence of the $\bar{N}N$ interaction, and thus one needs a polarized beam together with a polarized target. However, it is difficult to obtain a polarized antiproton beam with high intensity as compared with the case of a polarized proton beam, which is conventionally done by using, for example, the method of Atomic Beam

Source (ABS). Physicists have tried to obtain polarized antiproton beams with high intensity since 1980s but have not succeeded yet. Recently, the PAX collaboration proposed a program for polarizing an antiproton beam [4, 5]. Some theoretical predictions about the polarization of the antiproton beam have been made based on the Jülich $\bar{N}N$ models [5], the Paris $\bar{N}N$ model [63], and the Nijmegen $\bar{N}N$ model [64], respectively. In all of these cases, a noticeable polarization can be achieved in a reasonable time, although the results are different. The filtering mechanism [65] is used in the calculations in Refs. [5, 63, 64] because it has turned out that the polarization due to the filtering mechanism dominates [66] and the polarization due to the spin-flip mechanism can be ignored, which has also been verified by the experiment at COSY (COoler SYnchrotron) at Jülich [67]. Within a certain scattering angle, which is called the acceptance angle, the (elastic) scattered particles can still remain in the beam and thus can be scattered again in the next revolution. If the cross sections are spin dependent, the number of particles which remain in the beam are different for different spin states and thus after some time the remaining beam has some spin polarization. To obtain a polarized beam in this way is the so-called filtering mechanism. Furthermore, the filtering mechanism for polarizing a proton beam has been realized in the TSR (Test Storage Ring) at Heidelberg by the experiment FILTEX [68], and so there is hope that it will also work experimentally for an antiproton beam. We will give predictions for the polarization of an antiproton beam in $\bar{p}p$ scattering with a polarized proton target.

Based on our PWA, predictions for $\bar{p}p$ spin observables up to rank-two will be given. These can be used to compare with further experimental data hopefully obtained in the future. The higher-rank spin observables could be obtained straightforwardly, although this is not done, because it is difficult to measure even the lower-rank spin observables. The polarization of antineutrons produced through the charge-exchange process $\bar{p}p \to \bar{n}n$ will also be discussed briefly.

The organization of this thesis is as follows: In Chapter 2, the method of analysis, the boundary-condition approach, and the theory of the chiral one- and two-pion potentials are discussed. In Chapter 3, the antiproton-proton database and the statistical methods are discussed. After that, the results of the PWA are shown together with some experimental data as comparison. The S-matrix elements, the phase-shift and inelastic parameters (together with the mixing parameters), and the Argand diagrams are given as well. The statistical quality of the database is also discussed. In Chapter 4, the polarization of an antiproton beam by using the filtering mechanism is discussed. The cross-section differences between the antiparallel- and parallel-spin case in the transverse and longitudinal situation with respect to

the total charge-exchange cross section are shown for the charge-exchange scattering. In Chapter 5, some spin observables for elastic and charge-exchange scattering for several different energies are investigated. The polarization of antineutrons is discussed briefly. Finally, a Summary is given (in both English and Dutch).

Chapter 2

Theory Input for PWA[†]

2.1 The method of analysis

The method of analysis here is adapted from the Nijmegen PWAs of the pp and np scattering data [45–49] and from Refs. [42–44] of the PWA of $\bar{p}p$ scattering data. In this section, we will discuss the relativistic Schrödinger equation (which is just the differential form of the relativistic Lippmann-Schwinger equation [69]), the S matrices, and then the scattering amplitudes for $\bar{p}p$ (or $\bar{N}N$) scattering. The relativistic Schrödinger equation can be solved once we know the boundary conditions. In our case, the boundary condition at infinity are known. The boundary condition at a finite radius $r = b$ will be parametrized (which will be discussed in Section 2.2) and the parameters will be determined by fitting experimental data. In this way, the S matrices can be determined and then the scattering amplitudes.

For states with total angular momentum J, the radial part of the wave function for the antiproton-proton system is obtained by solving the coupled-channels radial Schrödinger equation [70]

$$\left[\frac{d^2}{dr^2} - \frac{L^2}{r^2} + p^2 - 2mV^J(r)\right]\Phi^J(r) = 0 \ , \tag{2.1}$$

which is a differential equation in channel space. We include the channels $\bar{p}p$ and $\bar{n}n$. It is important to use this physical basis instead of the isospin basis, in order to be able to include the long-range electromagnetic interactions and to treat the

[†]Chapters 2 and 3 are based on: D. Zhou and R. G. E. Timmermans, *Energy-dependent partial-wave analysis of all antiproton-proton scattering data below 925 MeV/c*, Phys. Rev. C **86**, 044003 (2012).

threshold for charge-exchange scattering $\bar{p}p \to \bar{n}n$ at $p_{\rm lab} \simeq 99$ MeV/c (or $T_{\rm lab} \simeq 5.2$ MeV) properly, which gives a much better description of the low-energy charge-exchange data. In Eq. (2.1), p is a diagonal matrix with the channel momentum p_a in the center-of-mass system (CMS); m is a diagonal matrix with the reduced mass m_a of the two scattered particles in channel a (so $m_a = M_p/2$ for $\bar{p}p$ scattering or $m_a = M_n/2$ for $\bar{n}n$ scattering); $V^J(r)$ is the potential with matrix elements $\langle \ell' s' a' | V^J(r) | \ell\, s\, a \rangle$; and $\Phi^J(r)$ is the radial part of the wave function. (ℓ and s are the orbit angular momentum and the total spin of the initial state respectively; and ℓ' and s' are the orbit angular momentum and the total spin of the final state respectively.) For partial waves with $\ell = J$, $s = 0$, 1 or $\ell = 1, J = 0$, the matrices are 2×2; and for partial waves with $\ell = J \pm 1$ ($J \geq 1$), $s = 1$, coupled by the tensor force, the matrices are 4×4. The relation between the total energy $\sqrt{s}$ in CMS and the channel momentum is given by the relativistic expression $\frac{1}{4}s = p_a^2 + 4m_a^2$.

The Eq. (2.1) is solved numerically, starting with the boundary condition at $r = b$, up to "$r = \infty$," which in practice is a point outside of the range of the strong interaction. The asymptotic form of $\Phi^J(r)$ for $r = \infty$ can be written as

$$\Phi^J_{\rm as}(r) \overset{r\to\infty}{\sim} \sqrt{\frac{m}{p}} \left[H_1(pr) S^J + H_2(pr) \right] \ , \tag{2.2}$$

where S^J is the partial-wave S matrix; H_1 and H_2 are diagonal matrices. For the $\bar{p}p$ channel, where the Coulomb force acts, the entries (which are proportional to the Coulomb analogues of the ordinary spherical Hankel functions) are given by

$$H^{(1)}_\ell(\eta, pr) = F_\ell(\eta, pr) - iG_\ell(\eta, pr) \ , \tag{2.3a}$$

$$H^{(2)}_\ell(\eta, pr) = F_\ell(\eta, pr) + iG_\ell(\eta, pr) \ , \tag{2.3b}$$

where F_ℓ and G_ℓ are the standard regular and irregular Coulomb wave functions; $\eta = -\alpha/v_{\rm lab}$ is the relativistic Coulomb parameter, where α is the fine-structure constant and $v_{\rm lab}$ is the velocity of the incoming antiproton in the laboratory frame. The asymptotic behavior of F_ℓ and G_ℓ is

$$F_\ell(\eta, pr) \overset{r\to\infty}{\sim} \sin\left[pr - \ell\frac{\pi}{2} + \sigma_\ell - \eta \ln(2pr) \right] \ , \tag{2.4a}$$

$$G_\ell(\eta, pr) \overset{r\to\infty}{\sim} \cos\left[pr - \ell\frac{\pi}{2} + \sigma_\ell - \eta \ln(2pr) \right] \ , \tag{2.4b}$$

where the Coulomb phase shift is $\sigma_\ell = \arg\,\Gamma(\ell + 1 + i\eta)$. For the $\bar{n}n$ channel, $\eta = 0$, and thus

$$F_\ell(0, \rho) = \rho j_\ell(\rho) \ , \qquad G_\ell(0, \rho) = -\rho n_\ell(\rho) \ , \tag{2.5}$$

where $j_\ell(\rho)$ and $n_\ell(\rho)$ are the ordinary spherical Bessel and Neumann functions of order ℓ, respectively. In this case, $H_\ell^{(1)}$ and $H_\ell^{(2)}$ are proportional to the ordinary spherical Hankel functions of the first kind and of the second kind, respectively. The S matrix is obtained from the matching condition

$$W\big(\Phi^J(r_\infty), \Phi^J_{\rm as}(r_\infty)\big) \equiv 0 \ , \tag{2.6}$$

where Φ^J is the numerical solution of Eq. (2.1) and $\Phi^J_{\rm as}$ is given by Eq. (2.2). The Wronskian is defined by

$$W(\Phi_1, \Phi_2) = \Phi_1^{\rm T} \frac{1}{m} \Phi_2' - \Phi_1'^{\rm T} \frac{1}{m} \Phi_2 \ , \tag{2.7}$$

where the prime denotes differentiation with respect to r and "T" means transposition. This gives for the partial-wave S matrix

$$\begin{aligned} S^J \ = \ & - \left[(\Phi^J)'^{\rm T} \frac{1}{\sqrt{mp}} H_1 - (\Phi^J)^{\rm T} \sqrt{\frac{p}{m}} H_1' \right]^{-1} \\ & \left[(\Phi^J)'^{\rm T} \frac{1}{\sqrt{mp}} H_2 - (\Phi^J)^{\rm T} \sqrt{\frac{p}{m}} H_2' \right] \ , \end{aligned} \tag{2.8}$$

where the prime on the Hankel functions denotes differentiation with respect to the argument pr. The parameters which parametrize the boundary condition at $r = b$ are contained in the wave function Φ^J in Eq. (2.8). These parameters will then be determined through the procedure of fitting.

Due to the presence of the long-range electromagnetic interaction, care has to be taken to define the S matrix (i.e., the phase-shift parameters) [43, 45, 71]. We include in the potential the long-range parts of the Coulomb, the magnetic-moment, and the strong (one- and two-pion exchange) interactions, $V = V_C + V_{MM} + V_N$. The Schrödinger equation is integrated up to a point outside the range of the strong interaction, where the solution is matched to the Coulomb (for $\bar{p}p$) and the Bessel (for $\bar{n}n$) wave functions. The S matrix is therefore defined with respect to the Coulomb force that acts in the $\bar{p}p$ channel. Because we need to include the infinite-range Coulomb interaction and part of the magnetic-moment interaction in all partial waves, but the finite-range nuclear interaction only up to some maximum value of J, we decompose the S matrix in order to split off the Coulomb part and the magnetic-moment part as

$$\begin{aligned} S_{C+MM+N} - 1 \ = \ & (S_C - 1) + S_C^{1/2} \left(S^C_{C+MM} - 1 \right) S_C^{1/2} + \\ & S_C^{1/2} \left(S^C_{C+MM} \right)^{1/2} \left(S^{C+MM}_{C+MM+N} - 1 \right) \left(S^C_{C+MM} \right)^{1/2} S_C^{1/2} \ , \end{aligned} \tag{2.9}$$

where S^{C+MM}_{C+MM+N} is the S matrix for the strong interaction in the presence of the Coulomb and magnetic-moment interactions (which means that the boundary condition at infinity is the same as the one in the case when the Coulomb and magnetic-moment interactions are included, and similar for the following). S^{C}_{C+MM} is the S matrix for the magnetic-moment interaction in the presence of the Coulomb interaction. S_C is the Coulomb S matrix with matrix elements $\langle \ell' s' | S_C | \ell\, s \rangle = \delta_{\ell\ell'}\delta_{ss'} \exp(2i\sigma_\ell)$ in the $\bar{p}p$ channel and zero in the $\bar{n}n$ channel. In Eq. (2.9) we used matrix notation, because the magnetic-moment interaction contains a tensor part and the S matrix is not diagonal in orbital angular momentum; its square root is well-defined, however.

The scattering amplitude is correspondingly decomposed as

$$M_{C+MM+N}(\theta) = M_C(\theta) + M^{C}_{C+MM}(\theta) + M^{C+MM}_{C+MM+N}(\theta)\ , \tag{2.10}$$

where $M_C(\theta)$ is the Coulomb scattering amplitude, $M^{C}_{C+MM}(\theta)$ is the magnetic-moment scattering amplitude in the presence of the Coulomb interaction, and $M^{C+MM}_{C+MM+N}(\theta)$ is the scattering amplitude for the strong interaction in the presence of the Coulomb and magnetic-moment interactions. The matrix elements of $M_C(\theta)$ for the $\bar{p}p$ elastic scattering are given by

$$\begin{aligned} \langle s' m' | M_C(\theta) | s\, m \rangle &= -\delta_{ss'}\delta_{mm'}\, \frac{\eta}{p(1-\cos\theta)} e^{-i\eta \ln \frac{1}{2}(1-\cos\theta) + 2i\sigma_0} \\ &= -\delta_{ss'}\delta_{mm'}\, \frac{\eta}{2p} \frac{e^{2i\sigma_0}}{(\sin^2 \frac{1}{2}\theta)^{1+i\eta}}\ , \end{aligned} \tag{2.11}$$

where s and s' denote the initial total spin and the final one respectively; m and m' are the z-components of the initial and final total spin; θ is the scattering angle in CMS; p is the momentum of the beam particle in CMS; σ_0 is the Coulomb phase shift with $\ell = 0$. The exponential term $\exp\left[-i\eta \ln \frac{1}{2}(1-\cos\theta)\right]$ is called the Breit factor [72]. (It is obvious that there is no pure Coulomb contribution to $\bar{p}p$ charge-exchange scattering.) The matrix elements $M^{C}_{C+MM}(\theta)$ of the magnetic-moment interaction are calculated in the Coulomb Distorted-Wave Born Approximation (CDWBA) [43, 71, 73, 74]. In the case of pp scattering, the plane-wave Born Approximation (BA) of the magnetic-moment amplitude did not agree with experimental data well [71, 73]. We assume this is also true in the $\bar{p}p$ case. It turns out that some of the spin-orbit parts of $M^{C}_{C+MM}(\theta)$ converge too slowly and should be summed analytically, instead of term by term with a computer. For the $\bar{p}p$ elastic

scattering, one has

$$\langle 1\,1|M^C_{C+MM}(\theta)|1\,0\rangle = -\frac{e^{2i\sigma_0}}{\sin\theta\sqrt{2}}\frac{(8\mu_p-2)\alpha}{4M_p}\left[e^{-i\eta\ln\frac{1}{2}(1-\cos\theta)}-\frac{1}{2}(1-\cos\theta)\right]$$
$$= -\langle 1\,0|M^C_{C+MM}(\theta)|1\,1\rangle\ . \qquad (2.12)$$

In practice, the η in the square bracket of Eq. (2.12) is set to be zero and it turns out that the difference of the results between the case when the η is zero and the case when the η is nonzero is very small. The other contributions from the magnetic-moment interaction are ignored because the contributions of the magnetic-moment interaction are very small as comparing with the contributions of the Coulomb interaction and the nuclear interaction and also because the data of spin observables are not accurate enough. The partial-wave decomposition of the nuclear scattering amplitude is given by

$$\langle s'm'a'|M^{C+MM}_{C+MM+N}(\theta)|s\,m\,a\rangle = \sum_{\ell\,\ell'\,J}\sqrt{4\pi(2\ell+1)}\,i^{\ell-\ell'}\,C^{\ell\ s\ J}_{0\ m\ m}\,C^{\ell'\ s'\ J}_{m-m'\ m'\ m}\,Y^{\ell'}_{m-m'}$$
$$\langle\ell's'a'|S_C^{1/2}\left(S^C_{C+MM}\right)^{1/2}\left(S^{C+MM}_{C+MM+N}-1\right)\left(S^C_{C+MM}\right)^{1/2}S_C^{1/2}|\ell\,s\,a\rangle/(2ip_a)\ , \quad (2.13)$$

where a denotes the channel $\bar{p}p$ or $\bar{n}n$; C is a Clebsch-Gordan coefficient; Y is a spherical harmonic; and $|\ell'-\ell|=0,\,2$. Because S^{C+MM}_{C+MM+N} is difficult to calculate it is approximated by $S^{C+MM}_{C+MM+N}\simeq S^C_{C+N}$, where S^C_{C+N} is the S matrix for the strong interaction in the presence of the Coulomb interaction and which will be calculated numerically by using Eq. (2.8). From the scattering amplitude on the spin-singlet, spin-triplet basis, all the observables can be calculated [75, 76].

2.2 The boundary-condition approach

In this section, we discuss the boundary-condition or "P-matrix" approach. The P matrix [77–81], defined as the logarithmic derivative of the wave function, is a useful tool to describe the physics at short distance, and has been applied successfully to the PWAs for the NN and $\bar{N}N$ scattering data, as one can see for instance in Refs. [43, 45–47]. Once the value of the P matrix is known the solution of Eq. (2.1), $\Phi^J(r)$, can be determined except for a common normalization factor. The other coefficient thus contains the information of the P matrix, which is therefore included in Eq. (2.8). After fitting, the parameters of the P matrix are fixed.

The short-range part of the $\bar{N}N$ interaction is very complicated and not understood well yet, therefore it is easy to treat this phenomenologically by us-

ing a parametrized boundary condition via the P matrix. The coupled-channels Schrödinger equation, i.e., Eq. (2.1), is solved with the boundary condition at a radius $r = b$ for each energy and for each partial wave (for details, see Ref. [45]). The fit to the data is not very sensitive to the exact value of b, but in our case an optimal value $b = 1.2$ fm was found. The value of b, in some sense, can be regarded as the range in which the annihilation happens because the annihilation processes are "absorbed" within the boundary (of course, not only annihilation happens in this range). For the specific form of the partial-wave boundary condition one defines the P matrix by

$$P^J = b \left[(\Phi^J)^{-1} \left(\frac{d\Phi^J}{dr} \right) \right]_{r=b} , \tag{2.14}$$

where $\Phi^J(r)$ is the radial wave function and the factor b is just to make the P matrix dimensionless. The P matrix parametrizes the complicated short-range interaction of the $\bar{p}p$ system. The coupling of the $\bar{p}p$ and $\bar{n}n$ channels to the mesonic annihilation channels is taken into account by using a complex P matrix.

The P matrix is a powerful tool in a PWA, since it provides the separation between the long-range interaction, which is relatively model independent and taken into account exactly in the Schrödinger equation, and the short-range interaction, which is essentially unknown and parametrized completely phenomenologically. The long-range interaction causes the rapid energy dependence of the scattering amplitudes while the short-range interaction results in slow energy variations, which can be understood by the uncertainty principle. The results, for that reason, do not depend on the details of the short-range interaction. We therefore choose a simple parametrization for the P matrix, which corresponds to a state-dependent, that is, spin- and isospin-dependent, short-range optical potential. We assume that the interaction in each partial wave can be parametrized by a complex spherical well, the depth of which is different for elastic and charge-exchange scattering, i.e., for $I = 0$ and $I = 1$. For a single-channel partial wave with orbital angular momentum ℓ, isospin I, and with the spherical potential well $V_I + iW_I$, the P matrix is given by

$$P_\ell = p'b\, J'_\ell(p'b)/J_\ell(p'b) , \tag{2.15}$$

where $J_\ell(\rho) = \rho j_\ell(\rho)$ and $p'^2 = p^2 - \overline{M}(V_I + iW_I)$, where $\overline{M} = (M_p + M_n)/2$. The prime on $J_\ell(\rho)$ denotes differentiation with respect to the argument ρ. Note that V_I and W_I are independent of r. The spherical potential well can be chosen to be energy dependent, however we chose them to be energy independent here because of slow energy variations in the short range.

The P matrix is calculated on the isospin basis and then transformed to the physical particle basis with the channels $\bar{p}p$, $\bar{n}n$. For the uncoupled partial waves with $\ell = J$, $s = 0$, 1 or $\ell = 1$, $J = 0$, it is therefore a 2×2 matrix. For the partial waves with $\ell = J \pm 1$ ($J \geq 1$), $s = 1$, coupled by the tensor force, we introduce for each value of the isospin I an additional mixing angle θ_{IJ} between the partial waves with $\ell = J - 1$ and $\ell = J + 1$. We write

$$P^J = \begin{pmatrix} \cos\theta_{IJ} & \sin\theta_{IJ} \\ -\sin\theta_{IJ} & \cos\theta_{IJ} \end{pmatrix} \begin{pmatrix} P_{J-1} & 0 \\ 0 & P_{J+1} \end{pmatrix} \begin{pmatrix} \cos\theta_{IJ} & -\sin\theta_{IJ} \\ \sin\theta_{IJ} & \cos\theta_{IJ} \end{pmatrix} , \qquad (2.16)$$

where P_{J-1} and P_{J+1} are the single-channel P matrices of Eq. (2.15) for $\ell = J-1$ and $\ell = J+1$, respectively. On the particle basis, the P matrix for these coupled states is 4×4. The mixing angle θ_{IJ} is energy independent here, as we do for the spherical potential well, though which can be chosen to be energy dependent. In the particle space, the P matrix is symmetric but not Hermitian which is the same as the case of S matrix because of the annihilation.

In Ref. [43], the imaginary parts of the square wells were assumed to be equal for $I = 0$ and $I = 1$ in each partial wave. We take these to be different here, because this choice gives a better fit to the more recent high-quality charge-exchange data. The fitted values of the P-matrix parameters are given in Table 2.1. The fit to 3749 scattering data requires a total of 46 P-matrix parameters. Almost all the short-range square-well potentials are attractive. One can also see that the errors are relatively very small, which is due to the high-quality data fitted. The quoted errors reflect the sensitivity of the fit to variations in the corresponding parameters. These errors are defined as the change in each parameter that gives a rise in $\chi^2_{\rm min}$ of 1 when the remaining parameters are refitted. The lower partial waves all require parameters to obtain a good fit. To decide which parameters to keep in the fit, a three-sigma criterion is used: When the error turns out to be greater than one third of the parameter mean value, it implies that $\chi^2_{\rm min}$ rises by less than 9 when the remaining parameters are refitted. In that case the parameter is set to zero, i.e., it is left out. Because of the centrifugal barrier, the fit becomes progressively less sensitive to short-range parameters for the higher-ℓ partial waves. We assume the parameters in these partial waves to be equal to the ones in similar lower partial waves. For example, the parameters for the ${}^3F_3$ and ${}^3G_4$ waves are taken to be the same as the ones for ${}^3D_2$; the ones for ${}^1G_4$ and ${}^1H_5$ are the same as the ones for ${}^1F_3$; and the ones for ${}^3G_5$ and ${}^3H_6$ are the same as the ones for ${}^3F_4$; and so on. We include the partial waves as high as $J = 12$, which is for instance needed to describe the "spike" at the most forward angles in the charge-exchange differential cross section.

Table 2.1: P-matrix parameters for the different partial waves. V_0 and V_1 are the real parts and W_0 and W_1 are the imaginary parts of the short-range spherical-well potential, for isospin $I = 0$ and $I = 1$, respectively. The values of the mixing angles θ_{IJ} that parametrize the off-diagonal P matrix for the partial waves coupled by the tensor force are: $\theta_{01} = 7.6^\circ \pm 0.4^\circ$ and $\theta_{11} = -10.7^\circ \pm 0.8^\circ$ for the ${}^3S_1$-${}^3D_1$ waves; $\theta_{02} = 0.0^\circ$ and $\theta_{12} = -8.8^\circ \pm 1.6^\circ$ for the ${}^3P_2$-${}^3F_2$ waves; $\theta_{03} = -7.4^\circ \pm 0.4^\circ$ and $\theta_{13} = -6.9^\circ \pm 1.4^\circ$ for the ${}^3D_3$-${}^3G_3$ waves. The quoted errors are defined as the change in each parameter that gives a rise in $\chi^2_{\rm min}$ of 1 when the remaining parameters are refitted.

Partial wave	V_0 (MeV)	W_0 (MeV)	V_1 (MeV)	W_1 (MeV)
${}^1S_0$	0	−161.7(25.2)	−516.1(19.4)	−132.8(19.9)
${}^3S_1$	−135.6(9.5)	−166.9(8.3)	33.6(5.7)	−166.3(8.0)
${}^1P_1$	0	−374.5(29.6)	0	−413.8(40.7)
${}^3P_0$	−114.9(10.1)	−142.8(9.3)	−164.1(4.5)	−71.9(6.9)
${}^3P_1$	−78.0(4.2)	−62.2(3.7)	0	−382.2(27.6)
${}^3P_2$	−114.6(5.7)	−201.4(5.1)	−41.4(3.0)	−135.6(5.4)
${}^1D_2$	−277.8(16.2)	−330.8(27.0)	−319.6(30.4)	−482.8(45.8)
${}^3D_1$	0	−96.6(15.5)	0	−129.4(19.7)
${}^3D_2$	−120.7(17.6)	−95.5(16.8)	0	−338.6(27.3)
${}^3D_3$	−235.7(7.7)	−181.1(8.4)	−102.0(9.1)	−66.6(7.8)
${}^1F_3$	−510.0(22.9)	−312.4(35.6)	0	−335.3(82.0)
${}^3F_2$	0	−356.0(56.6)	−554.0(26.5)	−317.1(27.0)
${}^3F_4$	−498.4(61.0)	−423.2(46.6)	0	0

2.3 The long-range antinucleon-nucleon potential

The long-range potentials of the $\bar{p}p$ interaction (which contain the Coulomb potential, the magnetic-moment potential and the nuclear potential) are discussed in this section. The nuclear potential is obtained from the G-parity transformation of the corresponding nuclear potential of the NN interaction [48, 56–61].

The potential tail for $r > b$ includes the electromagnetic and the strong (nuclear) interaction V_N, where the electromagnetic interaction is the one-photon exchange potential, i.e., the Coulomb potential and the magnetic-moment interaction [71],

$$V = V_C + V_{MM} + V_N \ . \tag{2.17}$$

In contrast to the NN PWAs, we do not include the vacuum-polarization potential, because its effects are negligible, except for very low energies [45], where there are no $\bar{p}p$ scattering data available. Two-photon exchange effects [82] are not taken into account either.

The one-photon–exchange potentials can be obtained from the phenomenological electromagnetic Lagrangian density

$$\mathcal{L}_\gamma = -\,e\,Q\left[i\bar{N}\gamma_\mu N\right]A^\mu \ - \ e\,\frac{\kappa}{4M}\left[\bar{N}\sigma_{\mu\nu}N\right](\partial^\mu A^\nu - \partial^\nu A^\mu) \ , \tag{2.18}$$

where e is the charge of the electron; Q is the nucleon charge in units of the electron charge; κ is the anomalous magnetic moment which is κ_p for proton and κ_n for neutron; M is the mass of the nucleon; N is the proton or neutron field and A^μ the photon field.

The Coulomb potential acts only in the $\bar{p}p$ channel and is given by the expression

$$V_C(r) = -\frac{\alpha'}{r} \ , \tag{2.19}$$

where α' takes care of the main relativistic corrections to the Coulomb potential. It is defined by the relativistic Coulomb factor $\eta = -\alpha' M_p/(2p)$. The magnetic-moment potential in the $\bar{p}p$ channel is given by

$$V_{MM}(r) \ = \ \frac{\mu_p^2}{4M_p^2}\,\frac{\alpha}{r^3}\,S_{12} \ + \ \frac{8\mu_p - 2}{4M_p^2}\,\frac{\alpha}{r^3}\,\boldsymbol{L}\cdot\boldsymbol{S} \ , \tag{2.20}$$

where $\mu_p = 1 + \kappa_p = 2.793$, with κ_p the anomalous magnetic moment of the proton; the tensor operator $S_{12} = 3\,\boldsymbol{\sigma}_1\cdot\widehat{\boldsymbol{r}}\,\boldsymbol{\sigma}_2\cdot\widehat{\boldsymbol{r}} - \boldsymbol{\sigma}_1\cdot\boldsymbol{\sigma}_2$, with $\boldsymbol{\sigma}_1$ and $\boldsymbol{\sigma}_2$ the spin operators of the two nucleons, $\boldsymbol{L}$ is the angular momentum vector in the system, and $\boldsymbol{S} = (\boldsymbol{\sigma}_1 + \boldsymbol{\sigma}_2)/2$ the total spin operator. The tensor force is due to the interaction between the magnetic moments of the two particles. The spin-orbit potential is due to the interaction of the magnetic moment of one particle with the charge of the other particle and includes a relativistic correction from the Thomas precession. The magnetic-moment interaction in the $\bar{n}n$ channel contains only the tensor-force part of Eq. (2.20) with $\mu_n = \kappa_n = -1.913$ and M_n.

The nuclear potential V_N contains the OPE and TPE potentials for $\bar{N}N$ scattering. Since the strong interaction is invariant under charge conjugation C, the $\bar{N}N$

potential can be obtained from the NN potential by using the operator C. If one assumes that isospin symmetry $SU(2,I)$ is exact, one can also use the G-parity operator, which is defined as $G = C\exp(i\pi I_2)$ [39], and thus contains charge conjugation and a rotation in isospin space. The OPE potential is isospin dependent, while the TPE potential contains both isospin-independent and isospin-dependent parts. When one defines the nuclear potential in isospin space for the NN system by

$$V_N(NN) = W_\pi\,\vec{\tau}_1\cdot\vec{\tau}_2 + V_{2\pi} + W_{2\pi}\,\vec{\tau}_1\cdot\vec{\tau}_2\ , \tag{2.21}$$

the potential for the $\bar{N}N$ system is given by

$$V_N(\bar{N}N) = -W_\pi\,\vec{\tau}_1\cdot\vec{\tau}_2 + V_{2\pi} + W_{2\pi}\,\vec{\tau}_1\cdot\vec{\tau}_2\ , \tag{2.22}$$

which implies for elastic and charge-exchange scattering, respectively,

$$V_N(\bar{p}p\to\bar{p}p) = W_\pi + V_{2\pi} - W_{2\pi}\ , \tag{2.23a}$$

$$V_N(\bar{p}p\to\bar{n}n) = 2\,(W_\pi - W_{2\pi})\ , \tag{2.23b}$$

where the factor 2 is due to isospin symmetry.

The pion-exchange potentials (OPE and TPE) for the NN scattering has been derived from the effective nonlinear chiral Lagrangian density, which implements the spontaneously broken $SU(2,L)\otimes SU(2,R)$ chiral symmetry of QCD [48, 58, 61]. The leading order of this effective Lagrangian density is the nonlinear Weinberg model given by

$$\mathcal{L}^{(0)} = -\bar{N}\Big[\gamma_\mu\mathcal{D}^\mu + M + ig_A\gamma_5\gamma_\mu\,\vec{\tau}\cdot\vec{D}^\mu\Big]N\ , \tag{2.24}$$

with the chiral-covariant derivative

$$\mathcal{D}^\mu N = \Big(\partial^\mu + \frac{i}{F_\pi}c_0\,\vec{\tau}\cdot\vec{\pi}\times\vec{D}^\mu\Big)N\ , \tag{2.25}$$

where $\vec{D}^\mu = D^{-1}\partial^\mu\vec{\pi}/F_\pi$ and $D = 1+\vec{\pi}^2/F_\pi^2$; M is the mass of the nucleon; $g_A = 1.269$ is the Gamow-Teller coupling constant in neutron β decay; and $F_\pi = 185$ MeV is the pion decay constant. The subleading-order chiral Lagrangian density is

$$\mathcal{L}^{(1)} = -\bar{N}\big[8c_1D^{-1}m_\pi^2\,\vec{\pi}^2/F_\pi^2 + 4c_3\,\vec{D}_\mu\cdot\vec{D}^\mu + 2c_4\,\sigma_{\mu\nu}\,\vec{\tau}\cdot\vec{D}^\mu\times\vec{D}^\nu\big]N\ . \tag{2.26}$$

The constant $c_0 = 1$ multiplying the Weinberg-Tomozawa $NN\pi\pi$ "seagull" interaction [83, 84] is fixed by chiral symmetry. However, the coupling constants c_j ($j = 1$, 3, 4) are low-energy constants that have to be determined from experimental data. These constants are of order $\mathcal{O}(1/M)$ and their values contain contributions from

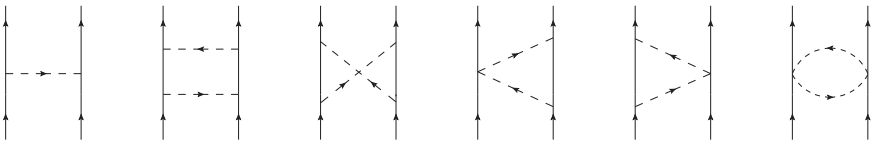

Figure 2.1: The Feynman diagrams for one- and two-pion exchange.

the "integrated-out" heavy hadrons, in particular the N- and Δ-isobars, and the two-pion resonances $\varepsilon(760)$ [43, 85] (which is also called "σ" or $f_0(600)$) and $\rho(770)$. (The constant c_2 does not contribute to NN scattering at this order.)

The Feynman diagrams for the OPE and TPE processes are shown in Figure 2.1, where the OPE diagram and the planar- and crossed-box TPE diagrams come from Eq. (2.24), the "triangle" and "football" TPE diagrams containing the Weinberg-Tomozawa $NN\pi\pi$ "seagull" interaction also come from Eq. (2.24), while the other "triangle" TPE diagrams containing the c_j ($j = 1, 3, 4$) $NN\pi\pi$ interactions come from Eq. (2.26). The pion-exchange potentials of Eq. (2.21) contain isospin-independent and isospin-dependent central, spin-spin, tensor, and spin-orbit terms,

$$\begin{aligned} V_N &= V_C + V_S\,\boldsymbol{\sigma}_1\cdot\boldsymbol{\sigma}_2 + V_T\,S_{12} + V_{SO}\,\boldsymbol{L}\cdot\boldsymbol{S} \\ &\quad + (W_C + W_S\,\boldsymbol{\sigma}_1\cdot\boldsymbol{\sigma}_2 + W_T\,S_{12} + W_{SO}\,\boldsymbol{L}\cdot\boldsymbol{S})\;\vec{\tau}_1\cdot\vec{\tau}_2\;, \end{aligned} \tag{2.27}$$

where for OPE only the coefficients W_S and W_T are nonzero, and TPE contains in leading order only the terms V_S, V_T, and W_C, whereas in subleading order all the terms are nonzero. The coefficients in Eq. (2.27) are written in terms of dimensionless functions as

$$V_i(r) + W_i(r)\,\vec{\tau}_1\cdot\vec{\tau}_2 = f^{2n}\,\xi^{2n}\,[v_i(x) + w_i(x)\vec{\tau}_1\cdot\vec{\tau}_2]\,m_\pi\;, \tag{2.28}$$

with $n = 1$ for OPE and $n = 2$ for TPE, $i = C$, S, T, SO, and $x = m_\pi r$. The conventional rationalized "pseudovector" $NN\pi$ coupling constant f is used here, and which is normalized such that $f^2 \simeq 0.075$ [86, 87]. This means that one introduces the scaling mass m_s, chosen to be numerically equal to the charged-pion mass $m_s = m_{\pi^+}$, and one defines $\xi = m_\pi/m_s$. If the Goldberger-Treiman relation [88] were exact, one would have that $g_A/F_\pi = \sqrt{4\pi}f/m_s$.

The OPE potential contains isospin-dependent spin-spin and tensor parts, with

$$w_S(x) = e^{-x}/3x\;, \tag{2.29a}$$

$$w_T(x) = \left(1 + x + x^2/3\right)e^{-x}/x^3\;. \tag{2.29b}$$

For the leading- and subleading-order TPE potentials, the isospin-independent and the isospin-dependent parts can be written as

$$v_i(x) = \frac{2}{\pi}\, v_{i,1}(x) + \frac{m_\pi}{M_p}\, v_{i,2}(x) \ , \tag{2.30a}$$

$$w_i(x) = \frac{2}{\pi}\, w_{i,1}(x) + \frac{m_\pi}{M_p}\, w_{i,2}(x) \ , \tag{2.30b}$$

where the subscript 1 indicates leading order and the subscript 2 subleading order. The leading-order, static TPE potential contains isospin-independent spin-spin and tensor terms and an isospin-dependent central term, with

$$v_{S,1}(x) = 12K_0(2x)/x^3 + (12+8x^2)K_1(2x)/x^4 \ , \tag{2.31a}$$

$$v_{T,1}(x) = -12K_0(2x)/x^3 - (15+4x^2)K_1(2x)/x^4 \ , \tag{2.31b}$$

$$\begin{aligned} w_{C,1}(x) = {} & \left(\tilde{c}_0^2 + 10\tilde{c}_0 - 23 - 4x^2\right) K_0(2x)/x^3 \\ & + \left[\tilde{c}_0^2 + 10\tilde{c}_0 - 23 + (4\tilde{c}_0 - 12)x^2\right] K_1(2x)/x^4 \ , \end{aligned} \tag{2.31c}$$

where $\tilde{c}_0 = c_0/\tilde{g}_A^2$ with $\tilde{g}_A = F_\pi\sqrt{4\pi}f/m_s$ and $K_n(2x)$ ($n = 0,\ 1$) are the modified Bessel functions (the hyperbolic Bessel functions) of the second kind, which have asymptotic behavior $K_n(2x) \sim \sqrt{\pi/4x}\, e^{-2x}$ for $x \to \infty$. The subleading-order potential contains nonstatic terms from Eq. (2.24) and the leading-order terms from Eq. (2.26), which can be written as

$$v_{i,2}(x) = \sum_{k=1}^{6} a_k\, e^{-2x}/x^k \ , \tag{2.32}$$

and similarly for the $w_{i,2}(x)$ terms. The coefficients a_k are listed in Table 2.2, where one defines $\tilde{c}_j = c_j M_p/\tilde{g}_A^2$ ($j = 1,\ 3,\ 4$) and $\tilde{c}_{04} = \tilde{c}_0 + 4\tilde{c}_4$.

The OPE and TPE potentials for $\bar{p}p \to \bar{p}p$ and for $\bar{p}p \to \bar{n}n$ are now given by Eq. (2.23a) and Eq. (2.23b) respectively. In the OPE potential, we take m_π for $\bar{p}p$ and $\bar{n}n$ elastic scattering to be the neutral-pion mass m_{π^0} and for charge-exchange scattering the charged-pion mass m_{π^+}. In the PWAs of Refs. [42, 43], the pion-nucleon coupling constant $f_c^2 = f_{pn\pi^+} f_{np\pi^-}/2$ was determined from the charge-exchange data. In Ref. [42] $f_c^2 = 0.0751(17)$ was found, and in Ref. [43] $f_c^2 = 0.0732(11)$. The values were consistent with the values for $f_{pp\pi^0}^2$ and f_c^2 found in the pp and np PWAs [86], resulting in the recommended value $f^2 = f_{NN\pi}^2 = 0.0750(9)$ for the pion-nucleon coupling constant, with no significant evidence for isospin breaking [87]. We have taken here the values $f_{pp\pi^0}^2 = 0.075$ and $f_c^2 = 0.075$ for the OPE potential for elastic and charge-exchange scattering, respectively. In the TPE potential we use for m_π the average pion mass $(2m_{\pi^+} + m_{\pi^0})/3 = 138.04$

Table 2.2: The coefficients a_k of the subleading-order TPE potential of Eq. (2.32) for the central, spin-spin, tensor, and spin-orbit terms [48]. $\tilde{c}_0 = c_0/\tilde{g}_A^2$; $\tilde{c}_j = c_j M_p/\tilde{g}_A^2$ for $j = 1$, 3, 4, and $\tilde{c}_{04} = \tilde{c}_0 + 4\tilde{c}_4$.

Coeff.	a_1	a_2	a_3	a_4	a_5	a_6
$v_{C,2}$	3/4	$9 + 48\tilde{c}_1 + 24\tilde{c}_3$	$27 + 96\tilde{c}_1 + 96\tilde{c}_3$	$99/2 + 48\tilde{c}_1 + 240\tilde{c}_3$	$54 + 288\tilde{c}_3$	$27 + 144\tilde{c}_3$
$v_{S,2}$		-3	-9	$-33/2$	-18	-9
$v_{T,2}$		3/2	27/4	15	18	9
$v_{SO,2}$			-12	-36	-48	-24
$w_{C,2}$	3/2	$4 - 2\tilde{c}_0$	$14 - 8\tilde{c}_0$	$31 - 20\tilde{c}_0$	$36 - 24\tilde{c}_0$	$18 - 12\tilde{c}_0$
$w_{S,2}$		$-2/3$	$-14/3 + 8\tilde{c}_{04}/3$	$-31/3 + 20\tilde{c}_{04}/3$	$-12 + 8\tilde{c}_{04}$	$-6 + 4\tilde{c}_{04}$
$w_{T,2}$		1/3	$17/6 - 4\tilde{c}_{04}/3$	$26/3 - 16\tilde{c}_{04}/3$	$12 - 8\tilde{c}_{04}$	$6 - 4\tilde{c}_{04}$
$w_{SO,2}$				$8 - 8\tilde{c}_0$	$16 - 16\tilde{c}_0$	$8 - 8\tilde{c}_0$

MeV and the charge-independent coupling constant $f^2 = f^2_{NN\pi} = 0.075$. The strong potentials for $\bar{n}n \to \bar{n}n$ and $\bar{n}n \to \bar{p}p$ are equal to the ones for $\bar{p}p \to \bar{p}p$ and $\bar{p}p \to \bar{n}n$, respectively.

The values of c_j ($j = 1$, 3, 4) were determined in the pp and np PWAs [48, 49]. The c_1 term in Eq. (2.26) breaks chiral symmetry explicitly, because it is proportional to m_π^2. The value of c_1 cannot be determined accurately from the NN data. It was fixed theoretically at $c_1 = -0.76/\text{GeV}$ by assuming a value for the pion-nucleon sigma term [48]. We take the same value of c_1 here. It is interesting, however, to probe the sensitivity of our results to variations in c_3 and c_4. It is difficult to determine c_3 and c_4 and their statistical errors by a fit to the database. Since they are parameters in the long-range interaction for $r > b$, this would require that for each small step in varying c_3 or c_4, the Schrödinger equation would have to be solved for all the energies. However, we found that very good results were obtained for the values $c_3 = -5.8/\text{GeV}$ and $c_4 = 4.0/\text{GeV}$, where we estimate the uncertainties to be of the order of 0.5. This means that the values we found are remarkably consistent with the values determined in the pp PWA to 350 MeV: $c_3 = -5.08(28)/\text{GeV}$ and $c_4 = 4.70(70)/\text{GeV}$ [48]. In the pp and np PWA to 500 MeV the values $c_3 = -4.78(10)/\text{GeV}$ and $c_4 = 3.96(22)/\text{GeV}$ were found [49]. One could interpret this as a demonstration of charge conjugation invariance of the TPE interaction. We leave a more careful study of the chiral OPE and TPE potential tail in $\bar{N}N$ scattering for the future.

The resulting long-range OPE and TPE potentials should be compared to the ones of Ref. [43] where the charge-conjugated version of the high-quality soft-core Nijmegen one-boson exchange (OBE) potential [10, 62] was used as long-range interaction. In both cases, OPE is included, so one should compare TPE to the exchange of the heavy bosons, in particular the two-pion resonances $\varepsilon(760)$ and $\rho(770)$. Since the vector mesons have negative charge parity, the coupling constants of $\rho(770)$ and $\omega(782)$ change sign when going from nucleons to antinucleons. When one writes schematically for the pp potential

$$V(pp \to pp) = W_\pi + V_\varepsilon + W_\rho + V_\omega + \cdots \ , \tag{2.33}$$

one obtains for the OBE potential for elastic $\bar{p}p \to \bar{p}p$ and charge-exchange $\bar{p}p \to \bar{n}n$ scattering

$$V(\bar{p}p \to \bar{p}p) = W_\pi + V_\varepsilon - W_\rho - V_\omega + \cdots \ , \tag{2.34a}$$

$$V(\bar{p}p \to \bar{n}n) = 2\,(W_\pi - W_\rho + \cdots) \ , \tag{2.34b}$$

respectively. One should compare Eq. (2.34a) and Eq. (2.34b) with Eq. (2.23a) and Eq. (2.23b), respectively. It implies that for the NN case the central potential is relatively weak, because there is a cancellation between the repulsion due to the vector mesons and the attraction due to the scalar mesons; there is a strong coherent spin-orbit force from the exchange of the scalar and vector mesons; and the tensor forces due to OPE and $\rho(770)$ exchange have opposite sign. For the $\bar{N}N$ case, there is a strong coherent central attraction results due to scalar- and vector-meson exchange and a relatively weak spin-orbit potential. Moreover, a strong coherent tensor potential acts in $\bar{N}N$ due to OPE and $\rho(770)$ exchange. This strong tensor force dominates the charge-exchange $\bar{p}p \to \bar{n}n$ and strangeness-exchange $\bar{p}p \to \bar{\Lambda}\Lambda$ processes, where no neutral mesons can be exchanged [89–92].

The chiral TPE potential in subleading order has qualitatively a number of similar features. Because the values of c_3 and c_4 are large, the corresponding "triangle" diagrams with an $NN\pi\pi$ interaction lead to relatively strong potentials. The c_3 term gives rise to a strong central attraction, while the c_4 term gives rise to a strong tensor force with the same sign as the tensor force due to OPE. This results in a strong attractive central force in the elastic process $\bar{p}p \to \bar{p}p$ and a strong coherent tensor force in the charge-exchange process $\bar{p}p \to \bar{n}n$. This can be understood because the c_3 and c_4 terms contain effects from "integrated-out" $\varepsilon(760)$ scalar-isoscalar and $\rho(770)$ vector-isovector mesons, respectively. In fact, these two mesons are prominent broad two-pion resonances. In the potential of Refs. [10, 62] and in the old PWA [43] their widths are treated in a two-pole approximation;

the lowest-mass poles correspond to mesons of masses of about 550 and 650 MeV, respectively, resulting in relatively long-range potentials.

Chapter 3

Database and Results of PWA

3.1 Antiproton-proton database and statistics

In this section, we discuss the antiproton-proton database and the statistical methods used in the PWA, such as the least-squares method, the error matrix, and the criteria for rejecting data.

The antiproton-proton database was constructed for the first time in Ref. [43]. It included all available scattering data below antiproton laboratory momentum 925 MeV/c published up to early 1993 in a regular physics journal, that is, total and annihilation cross sections, differential cross sections and analyzing powers for elastic and charge-exchange scattering, total cross sections for charge-exchange scattering, and (very few) differential depolarizations for elastic scattering. At that time, most of the experiments at LEAR were finished. However, some more data sets were published after the completion of the PWA of Ref. [43]. We include these data sets here, along with a few data sets for which the numerical values were not available back then. The present, new database is summarized in Table 3.1. The data sets that were not included in Ref. [43] are marked with an asterisk in the leftmost column of Table 3.1. We always consult the original publications for information about the data and their statistical and systematic uncertainties.

Statistical tools are an essential part of the data analysis in a PWA. We use exactly the same methods as in the NN PWAs [45]. We mention here only the main relevant points, more details can be found in Refs. [43, 45]. We perform a least-squares fit of the model parameters to the total database, which contains individual data sets labeled by A. One data set contains N_A individual data points

labeled by i. The χ^2 of the fit is correspondingly defined as

$$\chi^2(\boldsymbol{p}) = \sum_A \chi^2_A(\boldsymbol{p}) = \sum_A \min \left[\sum_{i=1}^{N_A} \left(\frac{M_{A,i}(\boldsymbol{p}) - \nu_A E_{A,i}}{\epsilon_{A,i}} \right)^2 + \left(\frac{\nu_A - 1}{\epsilon_{A,0}} \right)^2 \right] , \quad (3.1)$$

where $\boldsymbol{p}$ is the parameter vector with $N_{\rm par}$ entries, $M_{A,i}(\boldsymbol{p})$ is the value predicted by the model for the measured observable $E_{A,i}$ labeled i in set A with statistical error $\epsilon_{A,i}$ (in several cases, point-to-point systematic errors were added in quadrature to the statistical errors in the experimental papers). In most cases, the data sets have an overall normalization uncertainty, denoted by $\epsilon_{A,0}$, specified by the experimentalists. For each of these sets we introduce a normalization parameter ν_A that multiplies the measured values $E_{A,i}$ of the entire set. In the case that the experimental data sets are only relative, or in the case that the normalization error was underestimated, the error $\epsilon_{A,0}$ is taken to be ∞ (in practice very large) and the corresponding normalization parameter ν_A is "floated." The contributions to χ^2 of these normalizations are then zero. In a few cases the normalizations are absolute, i.e., $\epsilon_{A,0} = 0$, and the contributions to χ^2 of these normalizations are again zero.

By using a sophisticated numerical fitting code, the value of $\chi^2(\boldsymbol{p})$ is minimized with respect to the model parameters. By using the definition Eq. (3.1), the normalization parameters are adjusted implicitly. According to the theory of least-squares fitting, the expectation value of the minimum is $\langle \chi^2_{\rm min} \rangle = N_{\rm df} \pm \sqrt{2N_{\rm df}}$, where $N_{\rm df}$ is the number of degrees of freedom, provided the data points are distributed statistically (i.e., they do not contain systematic errors) and provided they are Gaussian (which is the case for counting experiments with enough events per bin). The error matrix E of the model parameters is defined by

$$(E^{-1})_{\alpha\beta} = \frac{\partial^2 \chi^2(\boldsymbol{p})}{2 \partial p_\alpha \partial p_\beta} \Big|_{\boldsymbol{p}=\boldsymbol{p}_{\rm min}} , \quad (3.2)$$

where $\boldsymbol{p}_{\rm min}$ are the values of the model parameters in the minimum value of χ^2. The error matrix allows us to determine the error of the model parameter p_α as $\sqrt{E_{\alpha\alpha}}$. This error corresponds to the variation in that parameter that gives a rise in $\chi^2_{\rm min}$ of 1 when the remaining parameters are refitted. As mentioned in Section 2.2, when the error is more than one-third of the parameter value, it implies that $\chi^2_{\rm min}$ rises by less than 9 when the remaining parameters are refitted. In that case the parameter is set to zero, i.e., it is left out. The error matrix allows us also to provide statistical uncertainties on our predictions for the observables. In the plots of the differential observables below, the PWA result is given as a solid red line with an area bordered by dotted blue lines that indicate the one-standard-deviation uncertainty in the prediction.

Table 3.1: Reference table of the antiproton-proton scattering data with $p_{\rm lab} \leq 923$ MeV/c. The asterisks in the leftmost column indicate the data sets that were not included in Ref. [43], because the data are more recent or because the values of the data points were not available. The meanings of the superscripts in the heading and the comments in the rightmost column are given at the end of the table.

$p_{\rm lab}$ (MeV/c)	No.[a] type[b]	$\chi^2_{\rm min}$	Norm error[v]	Pred. norm[c]	Rejected[d]	Ref.	Comment
119.0–923.0	50 $\sigma_{\rm ce}$	46.5	4%	1.058	$\leq$ 385.0, # = 8; 468.0	[93]	k, m
176.8–396.1	5 $\sigma_{\rm ann}$	9.4	4.4%	0.949	176.8	[94]	
181.0	46 d$\sigma_{\rm el}$	.	5%	.	All	[95, 96]	j, l, o
183.0	13 d$\sigma_{\rm ce}$	13.3	5%	1.002	0.940, −0.170, −0.574	[97]	
194.8	19 d$\sigma_{\rm el}$	.	4%	.	All	[98]	f, i, o
200.0–588.2	48 $\sigma_{\rm ann}$	52.5	2.2%	0.989		[94, 99]	
221.9–413.2	45 $\sigma_{\rm tot}$	55.3	∞	0.961	221.9, 229.6, 254.9, 260.8, 280.3, 289.1, 394.2, Norm	[100]	
233.0	54 d$\sigma_{\rm el}$	.	5%	.	All	[101]	f, j
239.2	20 d$\sigma_{\rm el}$	16.0	4%	1.077	−0.950	[98]	o
272.0	65 d$\sigma_{\rm el}$	61.8	5%	1.005		[101]	j
276.0–922.0	21 $\sigma_{\rm ce}$	26.2	7.5%	1.098		[102]	m
276.9	20 d$\sigma_{\rm el}$	20.9	4%	1.027		[98]	o
287.0	54 d$\sigma_{\rm el}$	.	5%	.	All	[95, 96]	j, l, o
287.0	14 d$\sigma_{\rm ce}$	29.6	5%	1.144		[97]	
310.4	20 d$\sigma_{\rm el}$	30.6	4%	1.024		[98]	o
340.9	20 d$\sigma_{\rm el}$	23.3	4%	1.033	−0.950, −0.850	[98]	o
348.7	38 d$\sigma_{\rm el}$	40.9	4%	0.973		[103]	i, o
353.3	119 d$\sigma_{\rm el}$	117.6	5%	1.007	0.366	[104]	j, o
355.0–923.0	36 $\sigma_{\rm tot}$	.	1.5%	.	All	[105]	e, m
359.0–652.0*	11 d$\sigma_{\rm el}$	.	2%	.	All	[106]	t
369.1	19 d$\sigma_{\rm el}$	16.0	4%	1.015	0.550	[98]	i, o
374.0	39 d$\sigma_{\rm el}$	27.8	5%	1.040		[107]	o

Table 3.1: (Continued.)

p_{lab}	No.[a]		Norm	Pred.			
(MeV/c)	type[b]	χ^2_{min}	error[v]	norm[c]	Rejected[d]	Ref.	Comment
388.0–598.6	29 σ_{tot}	35.2	∞	0.964	504.8, Norm	[108]	
392.4	19 dσ_{el}	.	5%	.	All	[109]	l
392.4	15 dσ_{ce}	8.6	5%(6.4%)	1.103	0.985, 0.954, 0.244, 0.099, -0.059, -0.239, -0.616	[110]	w
395.9–737.4*	28 σ_{tot}	19.4	0.8%	1.007	737.4	[111, 112]	
404.3	38 dσ_{el}	36.3	4%	0.974		[103]	i, o
406.0–922.0	30 dσ_{el}	29.9	∞	0.757	Norm	[113]	h, n
406.0	119 dσ_{el}	100.5	5%	1.002	0.991, 0.750, 0.579	[104]	j, o
411.2	38 dσ_{el}	33.0	5%	0.998	-0.875, -0.925	[107]	i, o
413.4	7 dσ_{el}	4.5	5%	1.043	0.992	[114]	j, o
424.5	7 dσ_{el}	.	5%	.	All	[114]	e, j, o
428.0	10 dσ_{ce}	9.6	20%	1.170		[115]	
435.8	7 dσ_{el}	1.2	5%	1.007	0.992	[114]	j, o
439.0	27 dσ_{el}	.	10%	.	All	[116]	l
439.0	24 $A_{y,\mathrm{el}}$	36.0	∞	1.579		[116]	g, o
439.9	39 dσ_{el}	40.8	5%	1.006		[107]	o
440.8	38 dσ_{el}	48.7	5%	1.024	0.725	[107]	i, o
444.1	38 dσ_{el}	48.2	4%	0.967	-0.875	[103]	i, o
446.0	119 dσ_{el}	115.7	5%	0.998		[104]	j, o
447.1	7 dσ_{el}	6.1	5%	1.038	0.992	[114]	j, o
458.3	8 dσ_{el}	2.2	5%	0.986	0.996	[114]	j, o
467.5	39 dσ_{el}	31.3	4%	1.019	-0.925	[103]	i, o
467.8	39 dσ_{el}	23.5	5%	1.033		[107]	o
469.2	8 dσ_{el}	8.0	5%	1.004	0.996	[114]	j, o
479.3	119 dσ_{el}	109.5	5%	0.982	0.919, 0.873, 0.697	[104]	j, o
480.0	10 dσ_{ce}	10.1	∞	1.113		[117]	g
481.2	8 dσ_{el}	6.5	5%	1.037	0.996	[114]	j, o
490.1	37 dσ_{el}	.	5%	.	All	[109]	l

Table 3.1: (Continued.)

$p_{\rm lab}$	No.[a]		Norm	Pred.			
(MeV/c)	type[b]	$\chi^2_{\rm min}$	error[v]	norm[c]	Rejected[d]	Ref.	Comment
490.1	15 $\mathrm{d}\sigma_{\rm ce}$	13.1	5%(6.9%)	1.001	0.992, −0.193, −0.381, −0.566	[110]	w
490.6	39 $\mathrm{d}\sigma_{\rm el}$	46.3	5%	0.963		[107]	o
492.7	8 $\mathrm{d}\sigma_{\rm el}$	3.9	5%	1.003	0.996	[114]	j, o
497.0	14 $A_{y,\rm el}$	10.3	4.5%	1.004		[118, 119]	
498.7	37 $\mathrm{d}\sigma_{\rm el}$	28.4	4%	0.989		[103]	i, o
503.8	8 $\mathrm{d}\sigma_{\rm el}$	12.6	5%	1.034	0.996	[114]	j, o
504.7	39 $\mathrm{d}\sigma_{\rm el}$	.	5%	.	All	[107]	e, o
505.0	54 $\mathrm{d}\sigma_{\rm el}$	.	5%	.	All	[95, 96]	j, l, o
505.0	14 $\mathrm{d}\sigma_{\rm ce}$	17.3	5%	1.021		[97]	
508.0	119 $\mathrm{d}\sigma_{\rm el}$	106.2	5%	0.998	0.663, 0.530	[104]	j, o
508.9	39 $\mathrm{d}\sigma_{\rm el}$	29.6	5%	1.005		[107]	o
516.0	8 $\mathrm{d}\sigma_{\rm el}$	5.1	5%	1.006	0.996	[114]	j, o
523.0	15 $A_{y,\rm el}$	11.5	4.5%	1.037		[118, 119]	
524.8	36 $\mathrm{d}\sigma_{\rm el}$	32.2	4%	1.004		[103]	i, o
525.9	39 $\mathrm{d}\sigma_{\rm el}$	42.5	5%	1.033		[107]	o
528.2	8 $\mathrm{d}\sigma_{\rm el}$	2.9	5%	0.993	0.996	[114]	j, o
533.6	119 $\mathrm{d}\sigma_{\rm el}$	126.1	5%	1.012	0.892	[104]	j, o
537.0	10 $\mathrm{d}\sigma_{\rm ce}$	12.5	∞	1.179		[117]	g
540.6	8 $\mathrm{d}\sigma_{\rm el}$	10.7	5%	1.004	0.996	[114]	j, o
543.2	39 $\mathrm{d}\sigma_{\rm el}$	43.9	5%	1.051		[107]	o
544.0	33 $\mathrm{d}\sigma_{\rm el}$	.	10%	.	All	[116]	l
544.0	30 $A_{y,\rm el}$	.	5%	.	All	[116]	f, g, o
546.0*	12 $\mathrm{d}\sigma_{\rm ce}$	12.7	15%	1.219		[120]	
546.0*	2 $\mathrm{d}\sigma_{\rm ce}$	1.0	15%	1.024		[120]	
546.0	23 $A_{y,\rm ce}$	23.3	4%	0.966	−0.250	[121]	
546.0*	13 $A_{y,\rm ce}$	.	4%	.	All	[122]	f
546.0*	7 $D_{yy,\rm ce}$	4.9	–	–		[122]	

Table 3.1: (Continued.)

p_{lab} (MeV/c)	No.[a] type[b]	χ^2_{min}	Norm error[v]	Pred. norm[c]	Rejected[d]	Ref.	Comment
549.4	10 dσ_{ce}	5.9	20%	1.219		[115]	
550.0	67 dσ_{el}	80.2	5%	0.978	0.997, 0.996, 0.995, 0.910, 0.883	[123]	j
553.1	34 dσ_{el}	37.1	4%	0.967		[103]	i, o
553.4	8 dσ_{el}	2.2	5%	1.008	0.996, 0.972	[114]	j, o
556.9	119 dσ_{el}	124.1	5%	1.002	0.908	[104]	j, o
558.5	39 dσ_{el}	45.2	5%	1.021		[107]	o
565.5	8 dσ_{el}	5.4	5%	0.994	0.996	[114]	j, o
568.4	37 dσ_{el}	35.4	5%	1.025	-0.675, -0.825	[107]	i, o
577.2	36 dσ_{el}	33.9	4%	0.969		[103]	i, o
578.1	9 dσ_{el}	6.0	5%	1.001	0.999	[114]	j, o
578.3	119 dσ_{el}	133.0	5%	1.022		[104]	j, o
584.0	10 dσ_{ce}	6.3	∞	1.043		[117]	g
590.0	39 dσ_{el}	.	5%	.	All	[95, 96]	j, l, o
590.0	15 dσ_{ce}	23.4	5%	1.030	0.996	[97]	
591.2	9 dσ_{el}	6.1	5%	1.016	0.999	[114]	j, o
591.2	39 dσ_{el}	.	5%	.	All	[109]	l
591.2	15 dσ_{ce}	11.3	5%(7.8%)	1.030	-0.358, -0.545	[110]	w
596.5	38 dσ_{el}	46.0	5%	1.059		[107]	o
599.2	33 dσ_{el}	15.8	4%	0.983		[103]	i, o
601.0*	47 dσ_{ce}	47.5	3%	1.035		[124]	
601.5*	47 dσ_{ce}	37.8	3%	1.074		[125]	
604.0	9 dσ_{el}	8.3	5%	0.975	0.999	[114]	j, o
615.0	38 dσ_{el}	55.0	5%	1.036		[107]	o
617.0	9 dσ_{el}	8.0	5%	0.944	0.998	[114]	j, o
630.0	10 dσ_{ce}	7.1	∞	1.046		[117]	g
630.9	9 dσ_{el}	4.5	5%	0.991	0.999	[114]	j, o
639.6	38 dσ_{el}	.	5%	.	All	[107]	e, o

Table 3.1: (Continued.)

$p_{\rm lab}$ (MeV/c)	No.[a] type[b]	$\chi^2_{\rm min}$	Norm error[v]	Pred. norm[c]	Rejected[d]	Ref.	Comment
644.7	9 $d\sigma_{\rm el}$	9.2	5%	0.961	0.998	[114]	j, o
656.0*	10 $d\sigma_{\rm ce}$	12.9	15%	1.220		[120]	
656.0*	7 $d\sigma_{\rm ce}$	14.6	15%	1.165		[120]	
656.0	17 $A_{y,\rm ce}$	11.2	4%	0.982		[126]	
656.0	21 $A_{y,\rm ce}$	23.5	4%	0.956		[121]	
658.1	38 $d\sigma_{\rm el}$	44.6	5%	0.963	0.225, −0.675	[107]	o
658.6	9 $d\sigma_{\rm el}$	8.9	5%	0.999	0.998	[114]	j, o
670.0	10 $d\sigma_{\rm ce}$	6.2	∞	1.150		[117]	g
671.5	9 $d\sigma_{\rm el}$	3.8	5%	0.981	0.998	[114]	j, o
679.0	26 $d\sigma_{\rm el}$	.	∞	.	All	[119]	h, l
679.0	27 $A_{y,\rm el}$	25.1	4.5%	1.005	0.540	[118, 119]	
679.0	1 $D_{yy,\rm el}$	3.2	–	–		[127]	q
679.1	4 $A_{y,\rm el}$	4.1	5%	0.984		[128]	o
680.1	38 $d\sigma_{\rm el}$	39.2	5%	0.990		[107]	o
686.1	9 $d\sigma_{\rm el}$	4.3	5%	0.980	0.998	[114]	j, o
689.0	39 $d\sigma_{\rm el}$	.	5%	.	All	[109]	l
689.0	16 $d\sigma_{\rm ce}$	17.9	5%(7.6%)	0.961	0.998, 0.981	[110]	w
690.0	89 $d\sigma_{\rm el}$	94.5	4%	0.978	0.370	[129]	
693.0	24 $d\sigma_{\rm ce}$	37.8	10%	1.103		[126]	r
693.0	17 $d\sigma_{\rm ce}$	20.4	10%	1.041		[126]	r
696.1	21 $d\sigma_{\rm el}$	18.5	4%	1.016		[130]	
696.1	16 $d\sigma_{\rm ce}$	15.3	4%	1.031		[130]	
697.0	24 $d\sigma_{\rm el}$	.	10%	.	All	[131]	l
697.0	33 $A_{y,\rm el}$	20.8	∞	1.213	0.629, Norm	[131]	o
698.0	10 $d\sigma_{\rm ce}$	7.0	∞	1.195		[117]	g
700.0	4 $A_{y,\rm el}$	1.3	5%	0.997		[132]	o
701.1	9 $d\sigma_{\rm el}$	3.8	5%	0.994	0.998	[114]	j, o
715.3	9 $d\sigma_{\rm el}$	10.6	5%	0.997	0.998	[114]	j, o

Table 3.1: (Continued.)

$p_{\rm lab}$ (MeV/c)	No.[a] type[b]	$\chi^2_{\rm min}$	Norm error[v]	Pred. norm[c]	Rejected[d]	Ref.	Comment
728.0	10 d$\sigma_{\rm ce}$	3.1	∞	1.065		[117]	g
730.0*	40 d$\sigma_{\rm ce}$	.	5%	.	All	[133]	f, s, u
757.0	72 d$\sigma_{\rm el}$	81.4	5%	1.023	0.999, 0.997, 0.996, 0.991	[123]	j
760.0*	24 d$\sigma_{\rm ce}$	.	5%	.	All	[134]	f, s
767.0*	10 d$\sigma_{\rm ce}$	9.1	15%	1.441		[120]	
767.0*	8 d$\sigma_{\rm ce}$	9.6	15%	1.231		[120]	
767.0	22 $A_{y,\rm ce}$	28.0	4%	1.106		[121]	
780.5	39 d$\sigma_{\rm el}$	.	5%	.	All	[109]	l
780.5	15 d$\sigma_{\rm ce}$	6.7	5%(7.1%)	0.963	0.982, −0.143	[110]	w
783.0	30 d$\sigma_{\rm el}$	.	∞	.	All	[119]	h, l
783.0	30 $A_{y,\rm el}$	36.2	4.5%	1.068	−0.300, −0.420	[118, 119]	
783.0	3 $D_{yy,\rm el}$	6.4	–	–		[127]	q
790.0	95 d$\sigma_{\rm el}$	95.3	4%	1.020		[129]	
860.0	95 d$\sigma_{\rm el}$	61.0	4%	1.019	0.510	[129]	
875.0*	10 d$\sigma_{\rm ce}$	8.1	15%	1.366		[120]	
875.0*	10 d$\sigma_{\rm ce}$	20.9	15%	1.183		[120]	
875.0*	12 d$\sigma_{\rm ce}$	8.4	15%	1.417		[135]	
875.0	23 $A_{y,\rm ce}$	12.1	4%	1.050		[121]	
875.0*	19 $A_{y,\rm ce}$	19.2	4%	0.972		[135]	
875.0*	13 $A_{y,\rm ce}$	14.0	15%	1.089		[135]	
875.0*	9 $D_{yy,\rm ce}$	5.1	–	–		[122, 136]	q
875.0*	5 $K_{yy,\rm ce}$	5.9	–	–		[137]	q
886.0	34 d$\sigma_{\rm el}$	.	∞	.	All	[119]	h, l
886.0	34 $A_{y,\rm el}$	34.1	4.5%	1.023		[118, 119]	
886.0	1 $D_{yy,\rm el}$	1.5	–	–		[127]	q
910.0	19 d$\sigma_{\rm el}$	.	∞	.	All	[138]	f, g
910.0	21 $A_{y,\rm el}$	12.9	5%	0.990		[138]	

a The number includes all published data, except those given as 0.0±0.0 (see Comment i), and those having $p_{\rm lab} > 923$ MeV/c (see Comment m).

b The subscripts "el" and "ce" denote observables in the elastic $\bar{p}p \to \bar{p}p$ and charge-exchange $\bar{p}p \to \bar{n}n$ reactions, respectively. "dσ" denotes a differential cross section dσ/dΩ, "A_y" a polarization-type datum (asymmetry or analyzing power), "D_{yy}" a depolarization type datum, and "K_{yy}" a spin-transfer type datum. "$\sigma_{\rm tot}$" stands for total cross section, "$\sigma_{\rm ann}$" for total annihilation cross section, and "$\sigma_{\rm ce}$" for total charge-exchange cross section.

c Normalization, predicted by the analysis, with which the experimental values should be multiplied before comparison with the theoretical values.

d Tabulated is $p_{\rm lab}$ in MeV/c, $\cos\theta$, "Norm" or "All." The notation "$\leq$ 385.0, # = 8," e.g., means that the 8 points with $p_{\rm lab} \leq 385.0$ MeV/c are rejected. The "Norm" means that the given normalization is rejected and a "floated" normalization is used instead. The "All" means that all of the data points in this set are rejected.

e Group rejected due to improbable low $\chi^2_{\rm min}$.

f Group rejected due to improbable high $\chi^2_{\rm min}$.

g "Floated" normalization. Data are relative only.

h Normalization "floated" by us, since the norm contributes much more than 9 to $\chi^2_{\rm min}$.

i Data point given as 0.0±0.0 not included.

j Coulomb-nuclear interference measurement. Data point in the extreme forward angular region is rejected when it contains multiple-scattering effects.

k Data point at low momenta rejected.

l Problematic differential cross sections. Not included in the database. For detailed explanations, see Sec. VIII of Ref. [43].

m Part of a group of data with points having $p_{\rm lab} > 923$ MeV/c.

n Elastic differential cross sections as a function of momentum taken at backward angle $\cos\theta = -0.994$.

o Normalization error assumed by us, since no clear number is stated in the reference.

p Depolarization data. Not included in the fit, in view of the large error bars.

q Normalization error taken to be zero, in view of the large error bars of these data.

r Data points taken at the same angles averaged.

s Data taken from the website `http://hepdata.cedar.ac.uk`.

t Data not available.

u The momentum is the average of 700 MeV/c and 760 MeV/c.

v Normalization error used in the fitting, as deduced from the experimental article; when not explicitly given, a reasonable value was assumed by us.

w The $x\%(y\%)$ notation means that $x\%$ is the overall normalization error and $y\%$ is the point-to-point systematic error.

The total $\chi^2_{\rm min}$ is only a global measure for the quality of the fit. In Section 3.4, we discuss in more detail the statistical quality of the final database, by examining the final χ^2 distribution of the data points and how it compares to theoretical expectations.

Data selection is a necessary ingredient of a PWA. In PWAs of large amounts of scattering data, a significant minority of the data sets turns out to be inconsistent with the rest of the database and with the PWA solution. In these cases, the data sets usually suffer from large systematic errors, which cannot be traced and corrected for. Examples in our case are the elastic differential cross sections measured at LEAR, which are inconsistent among themselves and with earlier measurements, and which in many cases cannot even be fitted properly with Legendre polynomials, as discussed at length in Ref. [43]. Including these flawed data sets would seriously bias the PWA solution. To decide whether a data set or an individual data point is acceptable, we use the standard statistical criteria outlined in Ref. [45] and already applied in Ref. [43]. They are generalized three-sigma criteria: Any single data point with $\chi^2_{A,i} > 9$ is rejected, as well as any data set with significantly too high or too low χ^2_A, according to the limits given in Ref. [45]. The chance to reject a correct datum or data set is at most 0.27% under these criteria. In Table 3.2, some of the values of χ^2 used in the generalized three-sigma criteria for rejecting a

Table 3.2: Some of the values of χ^2 used in the generalized three-sigma criteria for rejecting a data set. N equals $N_{\rm fp}$, $N_{\rm df}$, N_A, or $N_A - 1$ of the data set [45].

N	1	2	3	4	5	7	10	12	15	20	25	30
$\chi^2_{\rm high}(N)$	9.0	11.8	14.2	16.3	18.2	21.8	26.9	30.1	34.7	42.1	49.2	56.0
$\chi^2_{\rm low}(N)$				0.15	0.32	0.81	1.9	2.7	4.1	6.8	9.7	12.9
N	33	35	40	45	50	55	60	65	70	80	95	110
$\chi^2_{\rm high}(N)$	60.1	62.8	69.4	75.8	82.3	88.7	95.0	101.2	107.4	119.7	137.8	155.8
$\chi^2_{\rm low}(N)$	14.8	16.2	19.6	23.1	26.6	30.3	34.0	37.7	41.5	49.3	61.1	73.2

data set are given as an example. We use a multi-energy (or energy-dependent) fit therefore some of the criteria in Ref. [45] for a single-group fit (which is different from a single-energy fit) do not apply here. In our case, we take $N = N_A$ if the data set considered is not relative or $N = N_A - 1$ if the data set considered is relative. The χ^2 in Table 3.2 should be multiplied by a factor $N_{\rm df}/(N_{\rm df} + N_{\rm par})$ (which is 0.987 in our case with $N_{\rm df}$ the number of degrees of freedom and $N_{\rm par}$ the number of model parameters) before comparing with the corresponding χ^2 obtained from the fit. The reason is that each data point except the "floated" normalization ones should give a contribution to $\chi^2_{\rm min}$ by 1 whereas ideally $\langle\chi^2_{\rm min}\rangle = N_{\rm df}$ because of the parameters fitted. Some data or data groups are rejected because of other reasons, as mentioned also in the comment column of Table 3.1.

3.2 Description of the data

In this section, we give some of the results of the PWA. The values of the χ^2 are given. The partial-wave cross sections for both elastic and charge-exchange at some energies are presented. The comparisons between some of the experimental data and the corresponding results obtained from the PWA are shown in the figures plotted.

The final $\bar{p}p$ database contains $N_{\rm obs} = 3636$ data points of scattering observables. The details for each of the data sets can be found in Table 3.1. We need $N_{\rm par} = 46$ model (P-matrix) parameters for an optimal fit. In the fit we must determine at the same time $N_{\rm n}$ normalization parameters, so the total number of

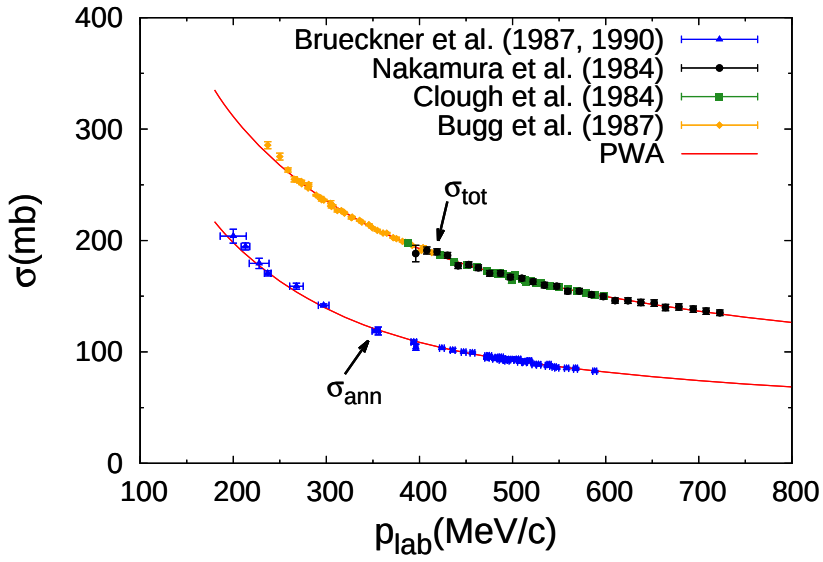

Figure 3.1: Total cross sections and total annihilation cross sections as functions of antiproton laboratory momentum. The PWA results are given by the solid red lines. The PWA fit has for Brückner *et al.* [94, 99] $\chi^2_{\rm min} = 9.4$ for 4 points $\sigma_{\rm ann}$ and $\chi^2_{\rm min} = 52.5$ for 48 points $\sigma_{\rm ann}$; for Nakamura *et al.* [112] $\chi^2_{\rm min} = 19.4$ for 27 points $\sigma_{\rm tot}$; for Clough *et al.* [108] $\chi^2_{\rm min} = 35.2$ for 28 points $\sigma_{\rm tot}$; for Bugg *et al.* [100] $\chi^2_{\rm min} = 55.3$ for 38 points $\sigma_{\rm tot}$.

free parameters is $N_{\rm fp} = N_{\rm par} + N_{\rm n}$. Of the $N_{\rm n}$ normalization parameters $N_{\rm ne}$ have a finite (but not zero) error, while the rest, $N_{\rm nf} = N_{\rm n} - N_{\rm ne}$, is the number of "floated" normalizations. In our case, the total number of normalizations is 131, but we fixed the normalizations for the five depolarization D_{yy} and for the one spin transfer K_{yy} measurements, because these data sets have relatively large error bars. Therefore, $N_{\rm n} = 125$. Of these, $N_{\rm nf} = 12$ normalizations are "floated," either because the data sets are relative only, or because the normalization errors were underestimated in the experimental articles. Thus, the number of normalizations with errors is $N_{\rm ne} = N_{\rm n} - N_{\rm nf} = 113$. This implies that the total number of free parameters is $N_{\rm fp} = N_{\rm par} + N_{\rm n} = 171$, the total number of data is $N_{\rm dat} = N_{\rm obs} + N_{\rm ne} = 3749$, and the number of degrees of freedom is $N_{\rm df} = N_{\rm dat} - N_{\rm fp} = 3578$. The fit results in a minimum χ^2 value of $\chi^2_{\rm min} = 3750.6$. (The total minimum χ^2 from the scattering observables is $\chi^2_{\rm obs} = 3671.97$, and the total minimum χ^2 from the normalizations is $\chi^2_{\rm norm} = 78.66$.) Therefore, the minimum χ^2 per datum is $\chi^2_{\rm min}/N_{\rm dat} = 1.000$, and the minimum χ^2 per degree of freedom is $\chi^2_{\rm min}/N_{\rm df} = 1.048$. When the model is perfect and the database is

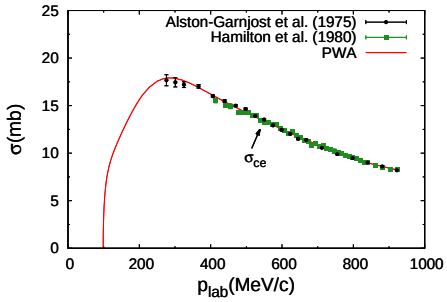

Figure 3.2: Total charge-exchange cross sections $\sigma_{\rm ce}$ as functions of antiproton laboratory momentum. The PWA result is given by the solid red line. The PWA fit has for Alston-Garnjost *et al.* [102] $\chi^2_{\rm min} = 26.2$ for 21 points; for Hamilton *et al.* [93] $\chi^2_{\rm min} = 46.5$ for 41 points.

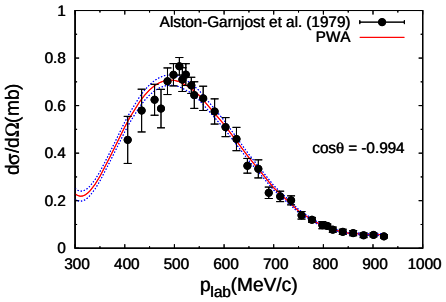

Figure 3.3: Elastic differential cross sections $d\sigma/d\Omega$ at backward angle, $\cos\theta = -0.994$, as functions of antiproton laboratory momentum. The PWA result is given by the solid red line and the dotted blue lines indicate the one-sigma uncertainty region. The fit has for Alston-Garnjost *et al.* [113] $\chi^2_{\rm min} = 29.9$ for 30 points.

a perfect statistical ensemble, one expects $\langle \chi^2_{\rm min}/N_{\rm df} \rangle = 1.000 \pm 0.024$; hence, our result for $\chi^2_{\rm min}/N_{\rm df}$ is only two standard deviations too high. The quality of the fit implies, in particular, that the charge-conjugated chiral OPE and TPE potential provides an excellent long-range $\bar{N}N$ interaction.

A detailed discussion of most of the data sets can be found in Ref. [43]. Here we show the results for a number of important data sets, and in particular address the high-quality data sets that were not available in Ref. [43]. The data sets in the figures have been multiplied by the predicted normalization factors given in Table 3.1. The rejected outliers are not plotted in the figures. In case point-to-point systematic errors were added in quadrature to the statistical errors, we plot these total errors.

In Figure 3.1 the total cross sections $\sigma_{\rm tot}$ (which is obtained from the optical theorem) and the total annihilation cross sections $\sigma_{\rm ann}$ are plotted as functions of $p_{\rm lab}$, the antiproton momentum in the laboratory frame. For the annihilation cross sections, we introduced two different normalization parameters for the data taken with a thin and with a thick target (cf. Table 3.1). In Figure 3.2 the total charge-exchange cross sections $\sigma_{\rm ce}$ are plotted as functions of $p_{\rm lab}$. Unfortunately, there are no good data that map out the rise of the cross section above the $\bar{p}p \to \bar{n}n$ threshold at $p_{\rm lab} \simeq 99$ MeV/c. In Figure 3.3 the elastic differential cross sections $d\sigma/d\Omega$ at backward angles with $\cos\theta = -0.994$ are plotted as functions of the momentum in

the laboratory frame. These data are described well, but the normalization of the data set was "floated." At low energies, the theoretical uncertainty of the PWA is significantly smaller than the errors of the data points.

The partial-wave cross sections for both elastic and charge-exchange scattering, the total cross sections and the total annihilation cross sections at $p_{\rm lab} = 200$, 400, 600, and 800 MeV/c are given in Table 3.3. It is clear that, in contrast to NN scattering, many partial waves contribute to $\bar{N}N$ scattering already at low energies. The reason is that the $\bar{N}N$ potentials, in particular the central and tensor components, are very strong. The dominance of the tensor force is seen, in particular, in the charge-exchange $\bar{p}p \to \bar{n}n$ reaction. For low energies of the final-state $\bar{n}n$ system the strong tensor force leads to large cross sections for the transitions $\ell(\bar{n}n) = \ell(\bar{p}p) - 2$, in particular, ${}^3D_1 \to {}^3S_1$ and ${}^3F_2 \to {}^3P_2$. This is similar to the strangeness-exchange reaction $\bar{p}p \to \bar{\Lambda}\Lambda$, where these off-diagonal tensor-force transitions due to $K(494)$ and $K^*(892)$ exchange dominate the cross section in the $\bar{\Lambda}\Lambda$ threshold region [91, 92]. For these transitions, there is a large overlap between the wave functions of the initial $\bar{p}p$ state and the final $\bar{n}n$ or $\bar{\Lambda}\Lambda$ state [92] at low energy. From Table 3.3 one can also see that the contributions from the spin-triplet states are much larger than the contributions from the spin-singlet states, especially in the $\bar{p}p \to \bar{n}n$ case. The total elastic cross section is about 1/3 of the total cross section in the energy range considered here. The total charge-exchange cross section is much smaller as compared with the total elastic cross section. The total charge-exchange cross section is about 5% of the total cross section at $p_{\rm lab} = 200$ MeV/c and about 8% of the total cross section at $p_{\rm lab} = 800$ MeV/c. The total annihilation cross section is large, and decreases from a fraction of about 2/3 of the total cross section at $p_{\rm lab} = 200$ MeV/c to about 1/2 of the total cross section at $p_{\rm lab} = 800$ MeV/c.

In Figures 3.4, 3.5, and 3.6 the differential cross sections $d\sigma/d\Omega$ and the analyzing powers A_y are shown for elastic scattering $\bar{p}p \to \bar{p}p$ at momenta near 690, 790, and 860 MeV/c, respectively. One can see that the data of the differential cross sections are relatively more accurate than the ones of the analyzing powers except for some data points, especially the data of the differential cross sections shown in Figure 3.5 and 3.6 are very accurate. In general, the uncertainty on the PWA prediction for the differential cross sections is determined by the accuracy of the data. For the analyzing powers, however, the theoretical uncertainties are, in general, smaller than the errors of the data points. The theoretical uncertainty is very small at forward angles. For backward angles, where there are no data available, this uncertainty increases. Figure 3.7 shows the very limited data available

Table 3.3: Partial-wave elastic and charge-exchange cross sections, total cross sections, and total annihilation cross sections, in mb, for $p_{\rm lab}$ = 200, 400, 600, and 800 MeV/c.

	$\bar{p}p \to \bar{p}p$				$\bar{p}p \to \bar{n}n$			
$p_{\rm lab}$ (MeV/c)	200	400	600	800	200	400	600	800
$^1S_0$	15.7	7.9	4.1	2.1	0.7	0.1		
$^1P_1$	0.9	2.5	4.5	5.6	0.8	0.1		
$^1D_2$	0.1	0.4	1.4	3.1	0.1	0.3	0.1	
$^1F_3$		0.1	0.2	0.5		0.1	0.1	0.1
$^1G_4$				0.1			0.1	0.1
$^3P_0$	4.9	5.4	5.0	3.5	1.5	0.8	0.1	
$^3P_1$	1.8	4.9	4.0	3.5	4.9	2.9	0.2	0.1
$^3D_2$	0.1	0.3	1.0	1.5	0.3	2.4	2.5	1.0
$^3F_3$		0.1	0.1	0.2		0.4	1.1	1.4
$^3G_4$			0.1	0.1		0.1	0.3	0.5
$^3S_1$	66.1	26.0	13.2	8.8	3.0	1.0	0.5	0.2
$^3S_1 \to {}^3D_1$	0.3	0.4	0.2	0.1	0.8	1.5	1.1	0.6
$^3D_1 \to {}^3S_1$	0.3	0.4	0.2	0.1	2.0	2.0	1.2	0.7
$^3D_1$	0.1	0.5	0.8	1.0	0.1	0.5	0.6	0.4
$^3P_2$	7.0	17.0	13.9	9.6	0.9	1.4	0.4	0.1
$^3P_2 \to {}^3F_2$	0.1	0.1	0.1		0.1	0.5	0.5	0.5
$^3F_2 \to {}^3P_2$	0.1	0.1	0.1		0.3	0.8	0.6	0.5
$^3F_2$			0.1	0.4			0.1	0.1
$^3D_3$		1.6	5.9	7.0		0.5	1.3	0.6
$^3D_3 \to {}^3G_3$		0.1	0.1			0.2	0.3	0.3
$^3G_3 \to {}^3D_3$		0.1	0.1			0.3	0.5	0.4
$^3G_3$								0.1
$^3F_4$			0.3	0.8			0.1	0.3
$^3F_4 \to {}^3H_4$				0.1			0.2	0.2
$^3H_4 \to {}^3F_4$				0.1		0.1	0.2	0.3
$^3H_4$								
Rest			0.1	0.3		0.1	0.4	0.8
Singlet	16.7	10.9	10.2	11.3	1.6	0.6	0.4	0.3
Triplet	80.8	56.9	45.1	37.1	14.0	15.6	12.1	9.2
Sum	97.5	67.9	55.3	48.4	15.6	16.2	12.5	9.4
	$\bar{p}p \to$ all				$\bar{p}p \to$ mesons			
$p_{\rm lab}$ (MeV/c)	200	400	600	800	200	400	600	800
Total	311.2	192.6	149.8	126.4	198.1	108.5	81.9	68.6

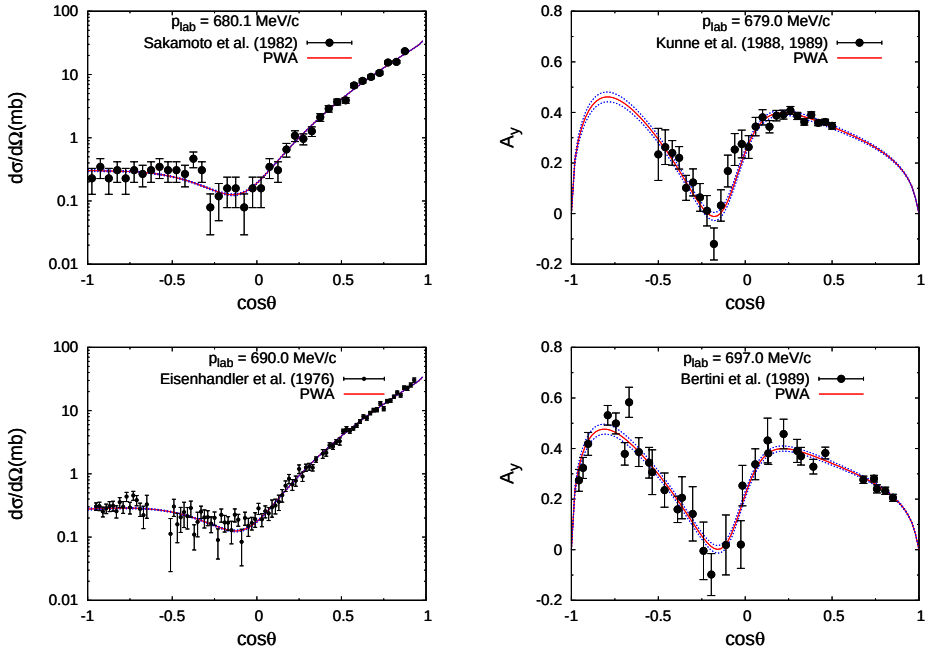

Figure 3.4: Differential cross sections and analyzing powers for elastic scattering as functions of angle in the center-of-mass system. The PWA result is given by the solid red line and the dotted blue lines indicate the one-sigma uncertainty region. The fit has for Sakamoto *et al.* [107] $\chi^2_{\rm min} = 39.2$ for 38 points $d\sigma/d\Omega$; for Kunne *et al.* [118, 119] $\chi^2_{\rm min} = 25.1$ for 26 points A_y; for Eisenhandler *et al.* [129] $\chi^2_{\rm min} = 94.5$ for 88 points $d\sigma/d\Omega$; for Bertini *et al.* [131] $\chi^2_{\rm min} = 20.8$ for 32 points A_y.

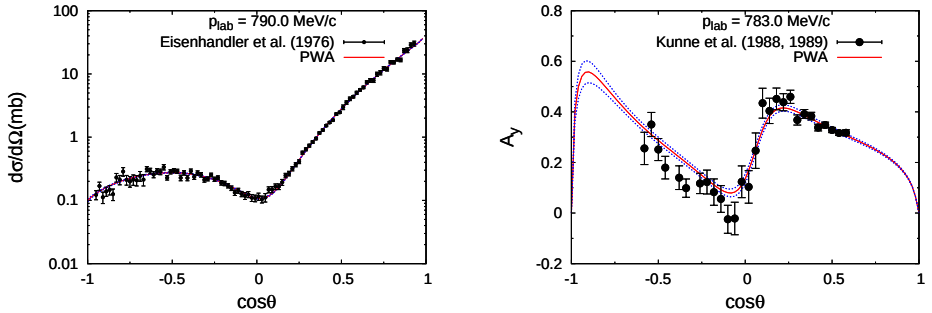

Figure 3.5: Differential cross sections and analyzing powers for elastic scattering as functions of angle in the center-of-mass system. The PWA result is given by the solid red line and the dotted blue lines indicate the one-sigma uncertainty region. The fit has for Eisenhandler *et al.* [129] $\chi^2_{\rm min} = 95.3$ for 95 points $d\sigma/d\Omega$; for Kunne *et al.* [118, 119] $\chi^2_{\rm min} = 36.2$ for 28 points A_y.

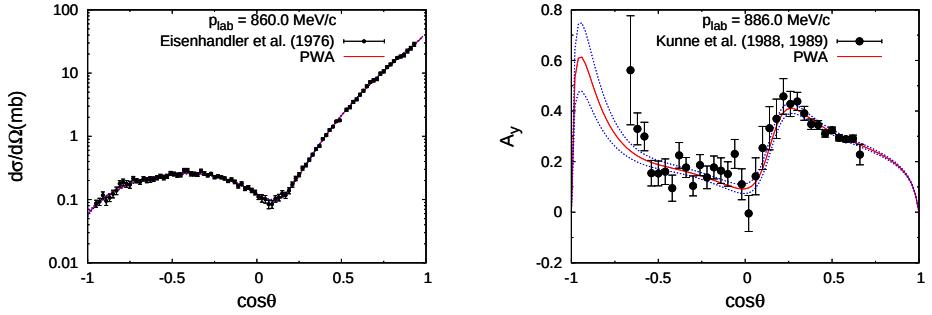

Figure 3.6: Differential cross sections and analyzing powers for elastic scattering as functions of angle in the center-of-mass system. The PWA result is given by the solid red line and the dotted blue lines indicate the one-sigma uncertainty region. The fit has for Eisenhandler *et al.* [129] $\chi^2_{\rm min} = 61.0$ for 94 points $d\sigma/d\Omega$; for Kunne *et al.* [118, 119] $\chi^2_{\rm min} = 34.1$ for 34 points A_y.

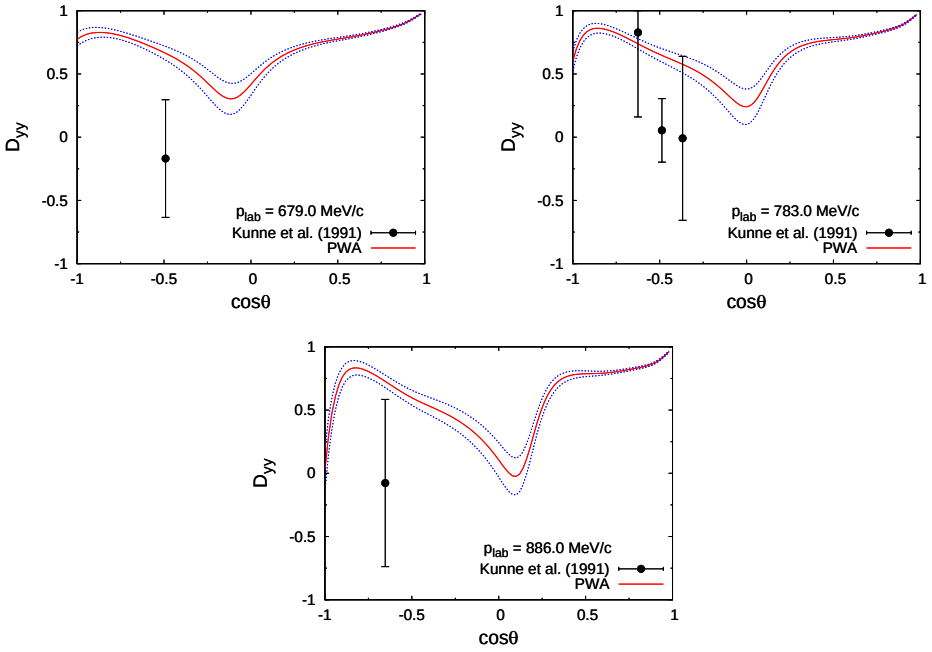

Figure 3.7: Differential depolarizations D_{yy} for elastic scattering as functions of angle in the center-of-mass system. The PWA result is given by the solid red line and the dotted blue lines indicate the one-sigma uncertainty region. The fit has for Kunne *et al.* [127] at $p_{\rm lab} = 679.0$ MeV/c $\chi^2_{\rm min} = 3.2$ for 1 point, at $p_{\rm lab} = 783.0$ MeV/c $\chi^2_{\rm min} = 6.4$ for 3 points, at $p_{\rm lab} = 886.0$ MeV/c $\chi^2_{\rm min} = 1.5$ for 1 point.

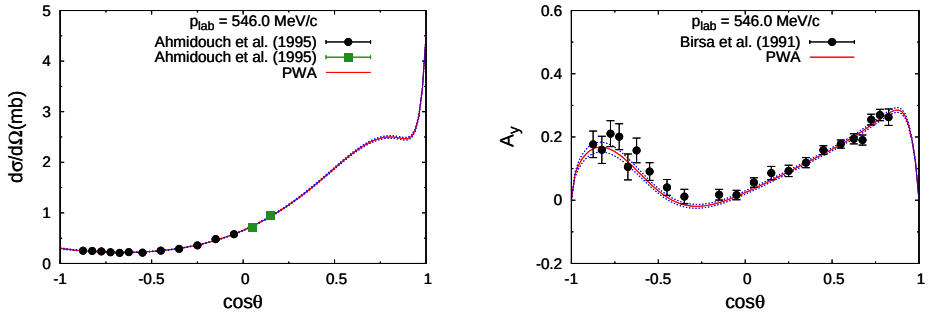

Figure 3.8: Differential cross sections and analyzing powers for charge-exchange scattering as functions of angle in the center-of-mass system. The PWA result is given by the solid red line and the dotted blue lines indicate the one-sigma uncertainty region. The fit has for Ahmidouch *et al.* [120] $\chi^2_{\rm min} = 12.7$ for 12 points $d\sigma/d\Omega$ at backward angles, $\chi^2_{\rm min} = 1.0$ for 2 points $d\sigma/d\Omega$ at forward angles; for Birsa *et al.* [121] $\chi^2_{\rm min} = 23.3$ for 22 points A_y.

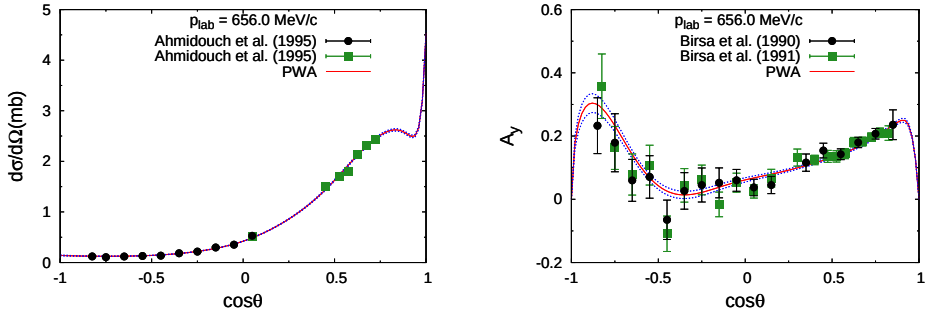

Figure 3.9: Differential cross sections and analyzing powers for charge-exchange scattering as functions of angle in the center-of-mass system. The PWA result is given by the solid red line and the dotted blue lines indicate the one-sigma uncertainty region. The fit has for Ahmidouch *et al.* [120] $\chi^2_{\rm min} = 12.9$ for 10 points $d\sigma/d\Omega$ at backward angles, $\chi^2_{\rm min} = 14.6$ for 7 points $d\sigma/d\Omega$ at forward angles; for Birsa *et al.* [126] $\chi^2_{\rm min} = 11.2$ for 17 points A_y; for Birsa *et al.* [121] $\chi^2_{\rm min} = 23.5$ for 21 points A_y.

for the depolarization D_{yy} for elastic scattering at 679, 783, and 886 MeV/c. There are only a few data points in the backward hemisphere and the data points have large error bars. In this case, the theoretical uncertainties of the PWA prediction are much smaller than the corresponding error bars, which implies that there is little new information in these data and that the fit would not change significantly if they were left out of the fit. The theoretical uncertainty is again very small at forward angles.

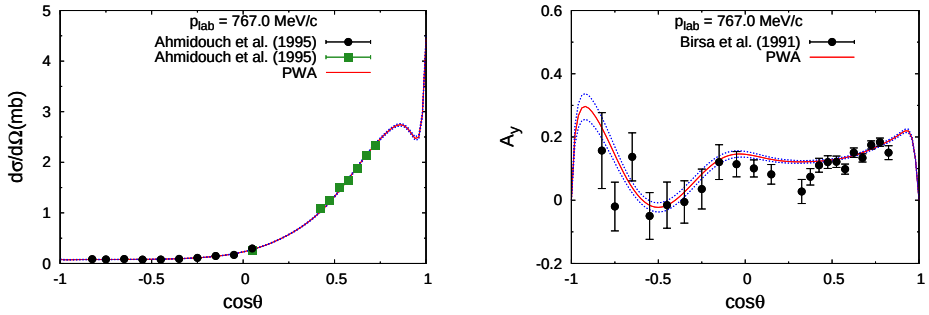

Figure 3.10: Differential cross sections and analyzing powers for charge-exchange scattering as functions of angle in the center-of-mass system. The PWA result is given by the solid red line and the dotted blue lines indicate the one-sigma uncertainty region. The fit has for Ahmidouch *et al.* [120] $\chi^2_{\rm min} = 9.1$ for 10 points $d\sigma/d\Omega$ at backward angles, $\chi^2_{\rm min} = 9.6$ for 8 points $d\sigma/d\Omega$ at forward angles; for Birsa *et al.* [121] $\chi^2_{\rm min} = 28.0$ for 22 points A_y.

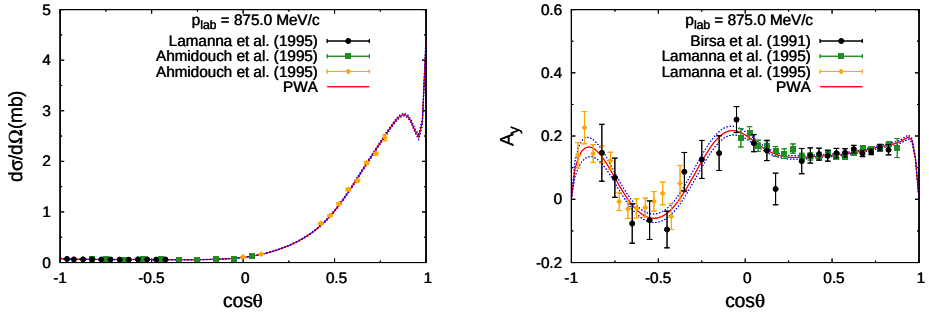

Figure 3.11: Differential cross sections and analyzing powers for charge-exchange scattering as functions of angle in the center-of-mass system. The PWA result is given by the solid red line and the dotted blue lines indicate the one-sigma uncertainty region. The fit has for Lamanna *et al.* [135] $\chi^2_{\rm min} = 8.4$ for 12 points $d\sigma/d\Omega$; for Ahmidouch *et al.* [120] $\chi^2_{\rm min} = 8.1$ for 10 points $d\sigma/d\Omega$ at backward angles, $\chi^2_{\rm min} = 20.9$ for 10 points $d\sigma/d\Omega$ at forward angles; for Birsa *et al.* [121] $\chi^2_{\rm min} = 12.1$ for 23 points A_y; for Lamanna *et al.* [135] $\chi^2_{\rm min} = 19.2$ for 19 points A_y at forward angles, $\chi^2_{\rm min} = 14.0$ for 13 points A_y at backward angles.

Figures 3.8, 3.9, 3.10, and 3.11 show the differential cross sections $d\sigma/d\Omega$ and the analyzing powers A_y for charge-exchange scattering $\bar{p}p \to \bar{n}n$ at 546, 656, 767, and 875 MeV/c, respectively. One can see that the data of the differential cross sections are relatively more accurate than the ones of the analyzing powers. Just as for the elastic case, one observes that, in general, the uncertainty on the PWA prediction for the differential cross sections is determined by the accuracy of the data. For the analyzing powers, however, the theoretical uncertainties are, in gen-

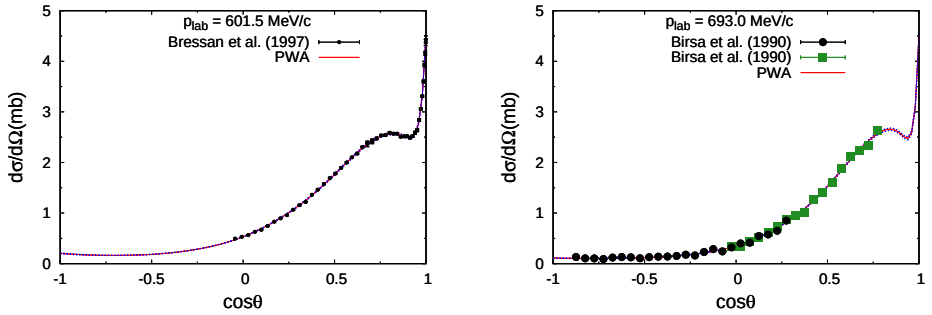

Figure 3.12: Differential cross sections $d\sigma/d\Omega$ for charge-exchange scattering as functions of angle in the center-of-mass system. The PWA result is given by the solid red line and the dotted blue lines indicate the one-sigma uncertainty region. The fit has for Bressan *et al.* [125] $\chi^2_{\rm min} = 37.8$ for 47 points; for Birsa *et al.* [126] $\chi^2_{\rm min} = 37.8$ for 24 points at backward angles, $\chi^2_{\rm min} = 20.4$ for 17 points at forward angles.

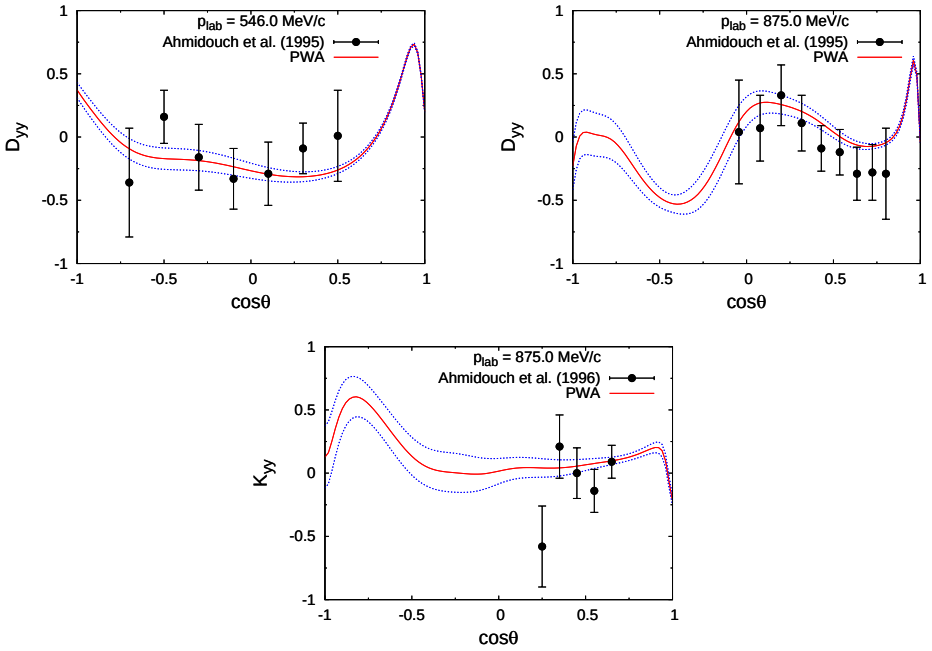

Figure 3.13: Differential depolarizations and spin transfers for charge-exchange scattering as functions of angle in the center-of-mass system. The PWA result is given by the solid red line and the dotted blue lines indicate the one-sigma uncertainty region. The fit has for Ahmidouch *et al.* [122] at $p_{\rm lab} = 546.0$ MeV/c $\chi^2_{\rm min} = 4.9$ for 7 points D_{yy}; for Ahmidouch *et al.* [122] (Birsa *et al.* [136]) at $p_{\rm lab} = 875.0$ MeV/c $\chi^2_{\rm min} = 5.1$ for 9 points D_{yy}; for Ahmidouch *et al.* [137] at $p_{\rm lab} = 875.0$ MeV/c $\chi^2_{\rm min} = 5.9$ for 5 points K_{yy}.

eral, smaller than the errors of the data points. At forward angles the theoretical uncertainty is again very small as in the elastic case. For some of the differential cross-section measurements, we introduced different normalization parameters for the data in the forward and in the backward hemisphere, which were taken with different detectors. The charge-exchange differential cross section is highly anisotropic, because of the contributions of many, high-ℓ partial waves. It has a "spike" at the most forward angles and it is flat at backward angles. It exhibits a very typical dip-bump structure at forward angles, which is due to the interference of the OPE interaction with a background due to short-range interactions [139]. The precise form of this structure evolves rapidly as a function of energy, from a rather flat plateau structure at 546 MeV/c to a pronounced dip-bump structure at 875 MeV/c. The structure was measured accurately at 601 MeV/c by the PS206 experiment at the end of the LEAR era [124, 125]. The high-quality charge-exchange differential cross sections from Ref. [125] are shown in Figure 3.12. At the time of Ref. [43], only the data at 693 MeV/c shown in Figure 3.12 were available [126], but these differential cross sections did not pin down the dip-bump structure. The PWA of Ref. [43] predicted a more pronounced structure for this data set.

In Figure 3.13 the few data sets available (although there are more data points than the elastic case) for the depolarization D_{yy} at 546 and 875 MeV/c and the spin transfer K_{yy} at 875 MeV/c in charge-exchange scattering are shown. The data points have large error bars, and also in this case the theoretical uncertainty for the PWA prediction is much smaller than these error bars. This demonstrates that spin observables are, of course, important, but they improve a good energy-dependent PWA only if they are precise enough [44]. The theoretical uncertainty is again very small at forward angles.

3.3 Phase-shift and inelasticity parameters

In this section we present the results of the S matrix, the phase-shift and inelastic parameters (together with the mixing parameters) for the lowest partial waves at some energies for $\bar{p}p$ scattering. The Argand diagrams for the lowest partial waves of $\bar{p}p$ scattering are also shown.

The S matrix for the coupled $\bar{p}p$ and $\bar{n}n$ channels from our PWA suffices to construct the complete scattering amplitudes and hence the observables. For the uncoupled partial waves with $\ell = J$, $s = 0$, 1 or $\ell = 1$, $J = 0$, the S matrix is 2×2, while for the coupled partial waves with $\ell = J \pm 1$ ($J \geq 1$), $s = 1$, it is a

4×4 matrix. We give numerical values at a number of momenta. Other results are available upon request. The matrix elements of S^C_{C+N} for different partial waves for the elastic and charge-exchange reactions are given in Tables 3.4, 3.5, and 3.6 for $p_{\rm lab} = 100$ to 1000 MeV/c. The S matrices are symmetric for the coupled partial waves in the case of elastic $\bar{p}p$ and $\bar{n}n$ scattering, but they are not symmetric in the case of charge-exchange scattering $\bar{p}p \leftrightarrow \bar{n}n$, as examples one can see from Table 3.5 for $\bar{p}p \to \bar{p}p$ and from Table 3.6 for $\bar{p}p \to \bar{n}n$.

For illustrative purposes we also present phase-shift and inelasticity parameters assuming that isospin symmetry is exact (we take then the average nucleon and pion mass and set the electromagnetic interaction to zero, however, the S matrix is still calculated in the presence of Coulomb force and which means that the S matrix is S^C_{C+N}). In this case, the parametrization of the S matrix can be done in a transparent way, similar to the procedures used for NN scattering (above the pion-production threshold).

For the uncoupled partial waves with $\ell = J$, $s = 0$, 1 or $\ell = 1$, $J = 0$, the S matrix, for isospin $I = 0$ or $I = 1$, is a 1×1 matrix that can be written as

$$S^J = \eta \exp(2i\delta) \ , \tag{3.3}$$

where δ is the phase shift and η ($0 \le \eta \le 1$) is the inelasticity due to the annihilation into mesonic channels. The S matrix for the uncoupled waves is thus given in terms of two real parameters, which are functions of energy. For high values of ℓ, where there is almost no annihilation, $\eta \to 1$.

For the partial waves with $\ell = J \pm 1$ ($J \ge 1$), $s = 1$, coupled by a tensor force, the S-matrix, for isospin $I = 0$ or $I = 1$, is now a symmetric 2×2 matrix that can be parametrized by the generalized "bar-phase" convention [140]

$$S^J = \exp(i\bar{\delta}) \, \exp(i\bar{\varepsilon}_J \sigma_x) \, H^J \, \exp(i\bar{\varepsilon}_J \sigma_x) \, \exp(i\bar{\delta}) \ , \tag{3.4}$$

where $\bar{\delta}$ is a 2×2 diagonal matrix with real entries $\bar{\delta}_{J-1,J}$ and $\bar{\delta}_{J+1,J}$, and $\bar{\varepsilon}_J$ is the mixing angle for the coupled partial waves; σ_x is the first Pauli matrix. The matrix H^J (which is real and symmetric) is used to parametrize the inelasticity. Different ways to write H^J can be found in literatures. We will follow the parametrization of Ref. [141], in which one writes

$$H^J = \exp(-i\omega_J \sigma_y) \begin{pmatrix} \eta_{J-1,J} & 0 \\ 0 & \eta_{J+1,J} \end{pmatrix} \exp(i\omega_J \sigma_y) \ , \tag{3.5}$$

where $\eta_{J-1,J}$ and $\eta_{J+1,J}$ are real numbers with $0 \le \eta_{J\mp1,J} \le 1$, and ω_J is the mixing angle for the inelasticity; σ_y is the second Pauli matrix. The S matrix for these coupled waves is thus given in terms of six real parameters.

From the numerical results of the PWA, one has to extract for each energy the phase-shift and inelasticity parameters from the numerical values of the S matrix. For the uncoupled partial waves this is easy. In order to obtain the phase-shift and inelasticity parameters for the coupled partial waves, the algorithm of Ref. [140] is used. One can write the S matrix as

$$S^J = \begin{pmatrix} R_{11}\exp(2i\delta_{11}) & iR_{12}\exp(2i\delta_{12}) \\ iR_{12}\exp(2i\delta_{12}) & R_{22}\exp(2i\delta_{22}) \end{pmatrix} , \tag{3.6}$$

where R_{ij} and δ_{ij} are real numbers. When one defines the auxiliary phases

$$\theta_a \equiv \delta_{11} - \bar{\delta}_{J-1,J} , \tag{3.7a}$$
$$\theta_b \equiv \delta_{22} - \bar{\delta}_{J+1,J} , \tag{3.7b}$$
$$\delta' \equiv \delta_{11} + \delta_{22} - 2\delta_{12} , \tag{3.7c}$$

it follows that

$$\tan 2(\theta_a + \theta_b) = \frac{R_{12}^2 \sin 2\delta'}{R_{11}R_{22} + R_{12}^2 \cos 2\delta'} , \tag{3.8a}$$
$$\tan(\theta_a - \theta_b) = \frac{R_{22} - R_{11}}{R_{11} + R_{22}} \tan(\theta_a + \theta_b) . \tag{3.8b}$$

From this the phase-shift parameters $\bar{\delta}_{J-1,J}$ and $\bar{\delta}_{J+1,J}$ can be obtained. The mixing angle $\bar{\varepsilon}_J$ is given by

$$\tan 2\bar{\varepsilon}_J = \frac{2R_{12}\cos(\theta_a + \theta_b - \delta')}{R_{11}\cos 2\theta_a + R_{22}\cos 2\theta_b} . \tag{3.9}$$

The elements of the matrix H^J can then be related to the parameters obtained. One finds

$$2H_{11}\cos 2\bar{\varepsilon}_J = R_{11}(1 + \cos 2\bar{\varepsilon}_J)\cos 2\theta_a + R_{22}(1 - \cos 2\bar{\varepsilon}_J)\cos 2\theta_b , \tag{3.10a}$$
$$2H_{22}\cos 2\bar{\varepsilon}_J = R_{11}(1 - \cos 2\bar{\varepsilon}_J)\cos 2\theta_a + R_{22}(1 + \cos 2\bar{\varepsilon}_J)\cos 2\theta_b , \tag{3.10b}$$
$$H_{12}\cos 2\bar{\varepsilon}_J = R_{12}\sin(\delta' - \theta_a - \theta_b) , \tag{3.10c}$$

from which one can determine the values of H_{11}, H_{22}, and H_{12}. By using Eq. (3.5), the remaining parameters $\eta_{J-1,J}$, $\eta_{J+1,J}$, and ω_J can be obtained via

$$\eta_{J-1,J} + \eta_{J+1,J} = \mathrm{Tr}\, H^J , \tag{3.11a}$$
$$\eta_{J-1,J}\,\eta_{J+1,J} = \det H^J , \tag{3.11b}$$
$$\tan 2\,\omega_J = 2H_{12}/(H_{11} - H_{22}) . \tag{3.11c}$$

If one extracts the values of the parameters for one single energy, there can be ambiguities [44]. In order to ensure continuity as a function of energy one can always change the values of these parameters in such a way that the corresponding S-matrix elements are not changed. In the case of uncoupled partial waves, one can change δ by 180° and keep η unchanged, as can be seen from Eq. (3.3). In the case of the coupled partial waves, for instance, one can change $\bar{\delta}_{J-1,J}$ or $\bar{\delta}_{J+1,J}$ by 180° and at the same time change the signs of both $\bar{\varepsilon}_J$ and ω_J, while keeping $\eta_{J-1,J}$ and $\eta_{J+1,J}$ unchanged; one can also change both $\bar{\delta}_{J-1,J}$ and $\bar{\delta}_{J+1,J}$ by 180° at the same time and keep $\eta_{J-1,J}$, $\eta_{J+1,J}$, $\bar{\varepsilon}_J$, and ω_J unchanged. In the limit where $\eta_{J\mp1,J} = 1$, $\bar{\delta}_{J\mp1,J} = 0$, and $\bar{\varepsilon}_J = 0$, one can choose $\omega_J = 0$ in order to keep continuity, although ω_J can take any value in this case while the corresponding S-matrix elements are unchanged. The results of the phase-shift and inelasticity parameters are given in Table 3.7 for $J \leq 4$ for the uncoupled partial waves, and in Table 3.8 for $J = 1$, 2 and in Table 3.9 for $J = 3$, 4 for the coupled partial waves for $p_{\rm lab} = 100$ to 1000 MeV/c.

A convenient way to plot the S matrix, or equivalently the T-matrix, defined by $T = (S-1)/i$, as a function of energy is to use Argand diagrams. Argand diagrams can be used to judge whether there is a resonance or not. However, only Argand diagrams are not enough, one needs to check "speed plots" (which show the absolute value of the derivative of the scattering amplitude with respect to the center-of-mass energy as a function of the center-of-mass energy) to see if there is a resonance. Here, we will not go further into this topic, and we just give some of the Argand diagrams which are also relatively easy to be compared qualitatively with results from other models. In Figure 3.14 Argand diagrams are shown of the uncoupled S, P, and D partial waves and in Figure 3.15 of the coupled S-D, P-F, and D-G partial waves for the laboratory momenta running from 1 to 1000 MeV/c by assuming isospin symmetry. All of these diagrams are within a unitary circle centering at the point $(0, 1)$.

Table 3.4: S-matrix elements of the uncoupled partial waves for $\bar{p}p \to \bar{p}p$ and $\bar{p}p \to \bar{n}n$.

	$p_{\rm lab}$(MeV/c)	100	200	300	400	500
$\bar{p}p \to \bar{p}p$	$^1S_0$	$0.596 - 0.193i$	$0.351 - 0.296i$	$0.162 - 0.300i$	$0.032 - 0.242i$	$-0.033 - 0.157i$
	$^3P_0$	$0.883 - 0.023i$	$0.657 - 0.199i$	$0.450 - 0.287i$	$0.216 - 0.248i$	$-0.007 - 0.145i$
	$^1P_1$	$0.987 + 0.023i$	$0.916 + 0.054i$	$0.806 + 0.015i$	$0.688 - 0.076i$	$0.563 - 0.181i$
	$^3P_1$	$0.989 - 0.030i$	$0.898 - 0.093i$	$0.745 - 0.173i$	$0.618 - 0.238i$	$0.524 - 0.253i$
	$^1D_2$	$1.000 + 0.002i$	$0.996 + 0.020i$	$0.977 + 0.050i$	$0.925 + 0.074i$	$0.835 + 0.072i$
	$^3D_2$	$1.000 - 0.003i$	$0.998 - 0.025i$	$0.981 - 0.050i$	$0.938 - 0.064i$	$0.869 - 0.071i$
	$^1F_3$	$1.000 + 0.000i$	$1.000 + 0.004i$	$0.999 + 0.015i$	$0.997 + 0.031i$	$0.989 + 0.051i$
	$^3F_3$	$1.000 + 0.000i$	$1.000 - 0.006i$	$0.999 - 0.021i$	$0.995 - 0.039i$	$0.985 - 0.052i$
	$^1G_4$	$1.000 + 0.000i$	$1.000 + 0.001i$	$1.000 + 0.005i$	$1.000 + 0.012i$	$0.999 + 0.020i$
	$^3G_4$	$1.000 + 0.000i$	$1.000 - 0.001i$	$1.000 - 0.008i$	$0.999 - 0.018i$	$0.998 - 0.030i$
$\bar{p}p \to \bar{n}n$	$^1S_0$	$-0.021 + 0.090i$	$0.068 + 0.131i$	$0.100 + 0.035i$	$0.070 - 0.041i$	$0.009 - 0.077i$
	$^3P_0$	$-0.007 + 0.002i$	$-0.220 - 0.020i$	$-0.301 - 0.082i$	$-0.303 - 0.120i$	$-0.247 - 0.115i$
	$^1P_1$	$0.000 + 0.003i$	$-0.007 + 0.093i$	$0.004 + 0.099i$	$0.027 + 0.066i$	$0.041 + 0.029i$
	$^3P_1$	$0.000 - 0.006i$	$0.026 - 0.228i$	$0.045 - 0.347i$	$0.043 - 0.345i$	$0.038 - 0.258i$
	$^1D_2$	$0.000 + 0.000i$	$0.000 + 0.025i$	$-0.004 + 0.063i$	$-0.008 + 0.084i$	$-0.010 + 0.087i$
	$^3D_2$	$0.000 + 0.000i$	$0.000 - 0.046i$	$-0.002 - 0.141i$	$0.004 - 0.246i$	$0.023 - 0.327i$
	$^1F_3$	$0.000 + 0.000i$	$0.000 + 0.005i$	$0.000 + 0.023i$	$-0.002 + 0.042i$	$-0.007 + 0.058i$
	$^3F_3$	$0.000 + 0.000i$	$0.000 - 0.008i$	$-0.001 - 0.040i$	$-0.003 - 0.089i$	$-0.006 - 0.145i$
	$^1G_4$	$0.000 + 0.000i$	$0.000 + 0.001i$	$0.000 + 0.008i$	$0.000 + 0.019i$	$-0.001 + 0.031i$
	$^3G_4$	$0.000 + 0.000i$	$0.000 - 0.001i$	$0.000 - 0.013i$	$-0.001 - 0.034i$	$-0.002 - 0.062i$
	$p_{\rm lab}$(MeV/c)	600	700	800	900	1000
$\bar{p}p \to \bar{p}p$	$^1S_0$	$-0.042 - 0.076i$	$-0.013 - 0.019i$	$0.036 + 0.007i$	$0.085 + 0.002i$	$0.123 - 0.026i$
	$^3P_0$	$-0.162 - 0.024i$	$-0.236 + 0.098i$	$-0.245 + 0.207i$	$-0.213 + 0.294i$	$-0.159 + 0.356i$
	$^1P_1$	$0.429 - 0.271i$	$0.289 - 0.330i$	$0.151 - 0.349i$	$0.027 - 0.331i$	$-0.075 - 0.280i$
	$^3P_1$	$0.443 - 0.222i$	$0.360 - 0.167i$	$0.281 - 0.110i$	$0.215 - 0.056i$	$0.170 - 0.007i$
	$^1D_2$	$0.721 + 0.032i$	$0.601 - 0.035i$	$0.482 - 0.110i$	$0.366 - 0.176i$	$0.253 - 0.223i$
	$^3D_2$	$0.789 - 0.081i$	$0.714 - 0.090i$	$0.648 - 0.090i$	$0.585 - 0.077i$	$0.521 - 0.056i$
	$^1F_3$	$0.971 + 0.077i$	$0.934 + 0.105i$	$0.874 + 0.126i$	$0.794 + 0.130i$	$0.703 + 0.112i$
	$^3F_3$	$0.969 - 0.057i$	$0.944 - 0.055i$	$0.910 - 0.048i$	$0.870 - 0.041i$	$0.826 - 0.036i$
	$^1G_4$	$0.998 + 0.030i$	$0.996 + 0.042i$	$0.992 + 0.058i$	$0.984 + 0.077i$	$0.969 + 0.101i$
	$^3G_4$	$0.994 - 0.041i$	$0.990 - 0.048i$	$0.983 - 0.052i$	$0.974 - 0.051i$	$0.962 - 0.047i$
$\bar{p}p \to \bar{n}n$	$^1S_0$	$-0.057 - 0.071i$	$-0.111 - 0.030i$	$-0.138 + 0.035i$	$-0.136 + 0.109i$	$-0.104 + 0.180i$
	$^3P_0$	$-0.171 - 0.084i$	$-0.100 - 0.061i$	$-0.043 - 0.058i$	$-0.006 - 0.076i$	$0.008 - 0.106i$
	$^1P_1$	$0.039 - 0.001i$	$0.027 - 0.019i$	$0.012 - 0.026i$	$-0.002 - 0.024i$	$-0.012 - 0.016i$
	$^3P_1$	$0.039 - 0.125i$	$0.044 + 0.014i$	$0.063 + 0.127i$	$0.100 + 0.202i$	$0.149 + 0.242i$
	$^1D_2$	$-0.009 + 0.078i$	$-0.007 + 0.065i$	$-0.007 + 0.054i$	$-0.009 + 0.045i$	$-0.011 + 0.040i$
	$^3D_2$	$0.050 - 0.362i$	$0.073 - 0.348i$	$0.084 - 0.294i$	$0.082 - 0.213i$	$0.071 - 0.123i$
	$^1F_3$	$-0.017 + 0.065i$	$-0.035 + 0.062i$	$-0.063 + 0.046i$	$-0.097 + 0.016i$	$-0.129 - 0.024i$
	$^3F_3$	$-0.006 - 0.204i$	$-0.001 - 0.258i$	$0.012 - 0.303i$	$0.032 - 0.330i$	$0.056 - 0.337i$
	$^1G_4$	$-0.001 + 0.041i$	$-0.003 + 0.048i$	$-0.005 + 0.052i$	$-0.008 + 0.053i$	$-0.015 + 0.053i$
	$^3G_4$	$-0.004 - 0.095i$	$-0.006 - 0.129i$	$-0.007 - 0.163i$	$-0.007 - 0.197i$	$-0.004 - 0.230i$

Table 3.5: S-matrix elements of the coupled partial waves for $\bar{p}p \to \bar{p}p$.

$p_{\rm lab}$(MeV/c)		100	200	300	400	500
$^3S_1 - {}^3D_1$	S_{11}	$0.514 - 0.307i$	$0.207 - 0.290i$	$0.039 - 0.195i$	$-0.039 - 0.096i$	$-0.071 - 0.015i$
	S_{22}	$0.998 + 0.003i$	$0.974 + 0.015i$	$0.926 + 0.025i$	$0.865 + 0.034i$	$0.798 + 0.044i$
	S_{12}	$0.004 - 0.015i$	$-0.010 - 0.058i$	$-0.031 - 0.093i$	$-0.056 - 0.108i$	$-0.077 - 0.103i$
$^3P_2 - {}^3F_2$	S_{11}	$0.971 + 0.021i$	$0.807 + 0.089i$	$0.558 + 0.111i$	$0.355 + 0.101i$	$0.220 + 0.095i$
	S_{22}	$1.000 + 0.000i$	$0.998 + 0.003i$	$0.991 + 0.008i$	$0.980 + 0.012i$	$0.964 + 0.018i$
	S_{12}	$0.000 - 0.003i$	$0.007 - 0.022i$	$0.016 - 0.038i$	$0.014 - 0.047i$	$0.004 - 0.055i$
$^3D_3 - {}^3G_3$	S_{11}	$1.000 + 0.000i$	$0.998 + 0.010i$	$0.981 + 0.055i$	$0.919 + 0.146i$	$0.791 + 0.247i$
	S_{22}	$1.000 + 0.000i$	$1.000 + 0.000i$	$0.999 + 0.003i$	$0.996 + 0.007i$	$0.991 + 0.010i$
	S_{12}	$0.000 + 0.000i$	$0.000 - 0.005i$	$0.002 - 0.020i$	$0.008 - 0.037i$	$0.019 - 0.046i$
$^3F_4 - {}^3H_4$	S_{11}	$1.000 + 0.000i$	$1.000 + 0.001i$	$1.000 + 0.005i$	$0.998 + 0.018i$	$0.990 + 0.045i$
	S_{22}	$1.000 + 0.000i$	$1.000 + 0.000i$	$1.000 + 0.001i$	$0.999 + 0.003i$	$0.998 + 0.005i$
	S_{12}	$0.000 + 0.000i$	$0.000 - 0.001i$	$0.000 - 0.007i$	$0.000 - 0.015i$	$0.002 - 0.026i$
$p_{\rm lab}$(MeV/c)		600	700	800	900	1000
$^3S_1 - {}^3D_1$	S_{11}	$-0.087 + 0.047i$	$-0.107 + 0.095i$	$-0.141 + 0.141i$	$-0.191 + 0.193i$	$-0.244 + 0.254i$
	S_{22}	$0.734 + 0.051i$	$0.671 + 0.047i$	$0.605 + 0.026i$	$0.526 - 0.016i$	$0.432 - 0.077i$
	S_{12}	$-0.092 - 0.078i$	$-0.097 - 0.040i$	$-0.095 - 0.001i$	$-0.089 + 0.027i$	$-0.082 + 0.037i$
$^3P_2 - {}^3F_2$	S_{11}	$0.141 + 0.097i$	$0.097 + 0.103i$	$0.073 + 0.110i$	$0.059 + 0.116i$	$0.051 + 0.121i$
	S_{22}	$0.938 + 0.031i$	$0.892 + 0.048i$	$0.822 + 0.066i$	$0.725 + 0.074i$	$0.610 + 0.063i$
	S_{12}	$-0.009 - 0.060i$	$-0.024 - 0.058i$	$-0.042 - 0.050i$	$-0.062 - 0.038i$	$-0.085 - 0.027i$
$^3D_3 - {}^3G_3$	S_{11}	$0.642 + 0.315i$	$0.518 + 0.354i$	$0.437 + 0.369i$	$0.401 + 0.357i$	$0.403 + 0.315i$
	S_{22}	$0.986 + 0.014i$	$0.981 + 0.021i$	$0.971 + 0.033i$	$0.952 + 0.055i$	$0.914 + 0.087i$
	S_{12}	$0.022 - 0.045i$	$0.014 - 0.041i$	$-0.003 - 0.037i$	$-0.026 - 0.032i$	$-0.055 - 0.023i$
$^3F_4 - {}^3H_4$	S_{11}	$0.972 + 0.085i$	$0.940 + 0.132i$	$0.897 + 0.177i$	$0.855 + 0.211i$	$0.822 + 0.229i$
	S_{22}	$0.996 + 0.008i$	$0.994 + 0.012i$	$0.990 + 0.015i$	$0.987 + 0.019i$	$0.981 + 0.026i$
	S_{12}	$0.005 - 0.037i$	$0.009 - 0.046i$	$0.012 - 0.052i$	$0.013 - 0.056i$	$0.012 - 0.059i$

Table 3.6: S-matrix elements of the coupled partial waves for $\bar{p}p \to \bar{n}n$.

	$p_{\rm lab}$(MeV/c)	100	200	300	400	500
$^3S_1 - {}^3D_1$	S_{11}	$-0.021 - 0.071i$	$-0.154 - 0.091i$	$-0.191 + 0.010i$	$-0.172 + 0.102i$	$-0.123 + 0.165i$
	S_{22}	$0.000 + 0.000i$	$-0.014 + 0.025i$	$-0.049 + 0.069i$	$-0.091 + 0.114i$	$-0.129 + 0.154i$
	S_{12}	$0.008 - 0.021i$	$0.003 - 0.148i$	$-0.042 - 0.228i$	$-0.098 - 0.269i$	$-0.146 - 0.280i$
	S_{21}	$0.000 + 0.000i$	$-0.012 - 0.093i$	$-0.055 - 0.179i$	$-0.108 - 0.229i$	$-0.154 - 0.248i$
$^3P_2 - {}^3F_2$	S_{11}	$-0.001 + 0.000i$	$-0.077 + 0.013i$	$-0.162 - 0.026i$	$-0.181 - 0.058i$	$-0.170 - 0.053i$
	S_{22}	$0.000 + 0.000i$	$-0.001 + 0.003i$	$-0.005 + 0.015i$	$-0.011 + 0.032i$	$-0.016 + 0.050i$
	S_{12}	$0.000 + 0.000i$	$0.008 - 0.045i$	$0.027 - 0.099i$	$0.035 - 0.135i$	$0.026 - 0.162i$
	S_{21}	$0.000 + 0.000i$	$0.005 - 0.028i$	$0.019 - 0.073i$	$0.024 - 0.110i$	$0.015 - 0.141i$
$^3D_3 - {}^3G_3$	S_{11}	$0.000 + 0.000i$	$-0.001 + 0.005i$	$-0.013 + 0.030i$	$-0.058 + 0.072i$	$-0.145 + 0.087i$
	S_{22}	$0.000 + 0.000i$	$0.000 + 0.000i$	$-0.001 + 0.004i$	$-0.003 + 0.012i$	$-0.006 + 0.021i$
	S_{12}	$0.000 + 0.000i$	$0.000 - 0.008i$	$0.002 - 0.037i$	$0.009 - 0.075i$	$0.023 - 0.107i$
	S_{21}	$0.000 + 0.000i$	$0.000 - 0.006i$	$0.001 - 0.029i$	$0.008 - 0.062i$	$0.021 - 0.092i$
$^3F_4 - {}^3H_4$	S_{11}	$0.000 + 0.000i$	$0.000 + 0.001i$	$0.000 + 0.005i$	$-0.002 + 0.015i$	$-0.009 + 0.032i$
	S_{22}	$0.000 + 0.000i$	$0.000 + 0.000i$	$0.000 + 0.001i$	$0.000 + 0.004i$	$-0.001 + 0.010i$
	S_{12}	$0.000 + 0.000i$	$0.000 - 0.001i$	$0.000 - 0.012i$	$0.000 - 0.030i$	$0.002 - 0.052i$
	S_{21}	$0.000 + 0.000i$	$0.000 - 0.001i$	$0.000 - 0.009i$	$0.000 - 0.025i$	$0.002 - 0.045i$
	$p_{\rm lab}$(MeV/c)	600	700	800	900	1000
$^3S_1 - {}^3D_1$	S_{11}	$-0.064 + 0.195i$	$-0.004 + 0.199i$	$0.050 + 0.180i$	$0.093 + 0.146i$	$0.120 + 0.105i$
	S_{22}	$-0.147 + 0.186i$	$-0.136 + 0.206i$	$-0.091 + 0.215i$	$-0.021 + 0.215i$	$0.059 + 0.207i$
	S_{12}	$-0.177 - 0.274i$	$-0.188 - 0.264i$	$-0.185 - 0.255i$	$-0.174 - 0.242i$	$-0.165 - 0.216i$
	S_{21}	$-0.183 - 0.251i$	$-0.193 - 0.247i$	$-0.189 - 0.244i$	$-0.177 - 0.235i$	$-0.166 - 0.211i$
$^3P_2 - {}^3F_2$	S_{11}	$-0.152 - 0.030i$	$-0.129 - 0.003i$	$-0.102 + 0.018i$	$-0.073 + 0.032i$	$-0.045 + 0.038i$
	S_{22}	$-0.019 + 0.067i$	$-0.015 + 0.083i$	$0.001 + 0.097i$	$0.031 + 0.113i$	$0.073 + 0.136i$
	S_{12}	$0.007 - 0.185i$	$-0.020 - 0.204i$	$-0.048 - 0.214i$	$-0.074 - 0.213i$	$-0.096 - 0.195i$
	S_{21}	$-0.003 - 0.166i$	$-0.028 - 0.187i$	$-0.055 - 0.201i$	$-0.080 - 0.202i$	$-0.100 - 0.187i$
$^3D_3 - {}^3G_3$	S_{11}	$-0.217 + 0.047i$	$-0.227 - 0.010i$	$-0.186 - 0.046i$	$-0.121 - 0.063i$	$-0.051 - 0.077i$
	S_{22}	$-0.009 + 0.031i$	$-0.011 + 0.043i$	$-0.014 + 0.056i$	$-0.020 + 0.073i$	$-0.035 + 0.089i$
	S_{12}	$0.034 - 0.128i$	$0.035 - 0.144i$	$0.026 - 0.160i$	$0.009 - 0.179i$	$-0.016 - 0.204i$
	S_{21}	$0.030 - 0.111i$	$0.029 - 0.128i$	$0.020 - 0.145i$	$0.002 - 0.165i$	$-0.022 - 0.190i$
$^3F_4 - {}^3H_4$	S_{11}	$-0.025 + 0.054i$	$-0.053 + 0.073i$	$-0.086 + 0.082i$	$-0.110 + 0.078i$	$-0.115 + 0.068i$
	S_{22}	$-0.003 + 0.016i$	$-0.005 + 0.022i$	$-0.007 + 0.029i$	$-0.010 + 0.036i$	$-0.013 + 0.043i$
	S_{12}	$0.005 - 0.075i$	$0.010 - 0.097i$	$0.014 - 0.116i$	$0.016 - 0.134i$	$0.014 - 0.151i$
	S_{21}	$0.005 - 0.067i$	$0.009 - 0.088i$	$0.013 - 0.106i$	$0.014 - 0.123i$	$0.012 - 0.140i$

Table 3.7: Phase-shift and inelasticity parameters of the uncoupled partial waves assuming isospin symmetry. δ is given in degrees.

$p_{\rm lab}$(MeV/c)		100	200	300	400	500	600	700	800	900	1000
$^{11}S_0$	η	0.61	0.48	0.39	0.31	0.24	0.18	0.13	0.11	0.13	0.16
	δ	179.28	169.97	157.96	145.40	132.28	117.71	99.83	77.61	56.50	41.44
$^{31}S_0$	η	0.73	0.51	0.34	0.20	0.09	0.02	0.10	0.18	0.25	0.31
	δ	−14.44	−26.94	−38.41	−49.03	−57.58	−4.58	4.39	−3.48	−11.88	−20.11
$^{13}P_0$	η	0.82	0.50	0.39	0.36	0.35	0.35	0.34	0.33	0.31	0.29
	δ	179.87	168.27	148.53	139.70	113.53	99.67	87.73	77.52	68.97	62.10
$^{33}P_0$	η	0.99	0.95	0.81	0.55	0.25	0.05	0.21	0.33	0.43	0.49
	δ	−1.31	−4.79	−6.79	−6.48	−4.03	40.24	67.02	64.93	60.66	55.86
$^{11}P_1$	η	0.99	0.93	0.83	0.72	0.63	0.54	0.47	0.41	0.36	0.31
	δ	1.63	4.71	4.03	−0.24	−6.81	−14.75	−23.54	−32.88	−42.63	−52.76
$^{31}P_1$	η	0.99	0.93	0.81	0.68	0.56	0.48	0.41	0.35	0.31	0.27
	δ	−0.43	−1.43	−2.83	−5.73	−10.51	−16.86	−24.39	−32.75	−41.74	−51.22
$^{13}P_1$	η	1.00	0.99	0.96	0.89	0.76	0.59	0.43	0.34	0.35	0.40
	δ	−2.70	−10.23	−16.84	−20.52	−21.74	−17.29	−9.54	2.48	13.45	19.05
$^{33}P_1$	η	0.98	0.88	0.73	0.59	0.49	0.42	0.36	0.32	0.28	0.24
	δ	1.34	5.24	7.05	5.13	0.27	−6.53	−14.57	−23.42	−32.84	−42.76
$^{11}D_2$	η	1.00	1.00	0.98	0.93	0.84	0.73	0.60	0.48	0.38	0.31
	δ	0.13	1.42	3.34	4.89	5.42	4.40	1.51	−3.28	−9.93	−18.44
$^{31}D_2$	η	1.00	1.00	0.98	0.94	0.85	0.73	0.62	0.52	0.44	0.37
	δ	−0.04	−0.34	−0.52	−0.38	−0.47	−1.67	−4.53	−9.07	−15.06	−22.19
$^{13}D_2$	η	1.00	1.00	1.00	0.99	0.98	0.95	0.91	0.83	0.73	0.62
	δ	−0.20	−2.28	−5.76	−9.30	−12.17	−13.97	−14.52	−13.70	−11.56	−8.11
$^{33}D_2$	η	1.00	1.00	0.99	0.95	0.88	0.79	0.69	0.60	0.52	0.46
	δ	0.08	0.99	3.00	5.76	8.54	10.44	10.92	9.91	7.65	4.44
$^{11}F_3$	η	1.00	1.00	1.00	1.00	0.99	0.97	0.92	0.83	0.71	0.58
	δ	0.01	0.31	1.11	2.12	3.15	4.21	5.23	5.95	5.85	4.32
$^{31}F_3$	η	1.00	1.00	1.00	1.00	1.00	0.99	0.97	0.94	0.90	0.85
	δ	0.00	−0.10	−0.30	−0.41	−0.24	0.31	1.25	2.44	3.67	4.69
$^{13}F_3$	η	1.00	1.00	1.00	1.00	1.00	1.00	1.00	0.99	0.98	0.96
	δ	−0.01	−0.47	−1.85	−3.76	−5.78	−7.67	−9.28	−10.49	−11.25	−11.50
$^{33}F_3$	η	1.00	1.00	1.00	1.00	1.00	0.99	0.97	0.93	0.89	0.83
	δ	0.00	0.17	0.71	1.62	2.86	4.41	6.19	8.00	9.59	10.71
$^{11}G_4$	η	1.00	1.00	1.00	1.00	1.00	1.00	1.00	0.99	0.98	0.97
	δ	0.00	0.06	0.39	0.90	1.47	2.03	2.59	3.17	3.81	4.55
$^{31}G_4$	η	1.00	1.00	1.00	1.00	1.00	1.00	1.00	1.00	0.99	0.99
	δ	0.00	−0.02	−0.12	−0.26	−0.36	−0.36	−0.20	0.14	0.68	1.39
$^{13}G_4$	η	1.00	1.00	1.00	1.00	1.00	1.00	1.00	1.00	1.00	1.00
	δ	0.00	−0.09	−0.61	−1.53	−2.69	−3.92	−5.13	−6.26	−7.26	−8.10
$^{33}G_4$	η	1.00	1.00	1.00	1.00	1.00	1.00	1.00	1.00	0.99	0.98
	δ	0.00	0.03	0.21	0.56	1.05	1.66	2.42	3.30	4.33	5.45

Table 3.8: Phase-shift and inelasticity parameters of the coupled partial waves with $J = 1, 2$ assuming isospin symmetry. $\bar{\delta}$, $\bar{\varepsilon}_J$ and ω_J are given in degrees.

$p_{\rm lab}$(MeV/c)		100	200	300	400	500	600	700	800	900	1000
$^{13}S_1$	η_S	0.63	0.37	0.22	0.15	0.14	0.14	0.16	0.17	0.19	0.22
	$\bar{\delta}_S$	160.16	141.90	125.45	111.64	99.16	86.70	76.21	69.19	65.54	64.21
–	ω_1	3.71	9.61	15.24	20.32	24.93	29.08	31.90	33.49	34.89	37.29
	$\bar{\varepsilon}_1$	1.62	6.90	12.60	17.51	20.74	21.16	19.42	16.88	14.46	12.61
$^{13}D_1$	η_D	1.00	1.00	0.99	0.98	0.96	0.92	0.88	0.84	0.79	0.74
	$\bar{\delta}_D$	0.17	2.01	5.83	11.08	16.81	21.13	22.53	21.15	17.91	13.54
$^{33}S_1$	η_S	0.63	0.43	0.32	0.25	0.20	0.17	0.14	0.12	0.13	0.18
	$\bar{\delta}_S$	173.41	166.53	159.57	152.23	144.07	134.41	121.85	104.94	87.16	76.85
–	ω_1	−0.91	−1.57	−1.60	−1.83	−3.08	−6.20	−12.04	−20.87	−30.83	−41.24
	$\bar{\varepsilon}_1$	−0.71	−2.87	−5.09	−7.00	−8.64	−10.00	−10.48	−8.07	−1.29	4.78
$^{33}D_1$	η_D	1.00	1.00	1.00	0.99	0.97	0.94	0.89	0.83	0.76	0.69
	$\bar{\delta}_D$	−0.03	−0.49	−1.42	−2.43	−3.20	−3.60	−3.79	−5.09	−10.94	−21.33
$^{13}P_2$	η_P	0.96	0.74	0.42	0.21	0.10	0.07	0.06	0.06	0.05	0.04
	$\bar{\delta}_P$	0.70	3.82	6.18	7.70	14.21	27.68	35.57	37.95	41.92	51.99
–	ω_2	−0.76	−2.19	−2.36	−1.09	2.34	8.38	13.50	17.31	20.64	22.71
	$\bar{\varepsilon}_2$	−0.18	−2.11	−5.30	−8.55	−11.14	−11.37	−9.80	−7.77	−3.92	3.71
$^{13}F_2$	η_F	1.00	1.00	1.00	1.00	1.00	0.99	0.97	0.94	0.89	0.84
	$\bar{\delta}_F$	0.01	0.23	0.82	1.44	1.68	1.49	2.06	3.35	5.59	9.60
$^{33}P_2$	η_P	0.99	0.91	0.75	0.57	0.42	0.32	0.26	0.21	0.17	0.15
	$\bar{\delta}_P$	0.38	2.34	5.48	8.41	10.48	11.72	12.32	12.79	14.08	17.35
–	ω_2	0.28	0.85	1.01	0.65	−0.11	−1.18	−2.49	−3.96	−5.49	−6.91
	$\bar{\varepsilon}_2$	0.06	0.67	1.74	2.89	4.01	5.19	6.58	8.31	10.38	12.49
$^{33}F_2$	η_F	1.00	1.00	1.00	1.00	0.99	0.97	0.93	0.85	0.73	0.58
	$\bar{\delta}_F$	0.00	−0.06	−0.29	−0.64	−1.00	−1.26	−1.40	−1.63	−2.48	−5.12

Table 3.9: Phase-shift and inelasticity parameters of the coupled partial waves with $J = 3$, 4 assuming isospin symmetry. $\bar{\delta}$, $\bar{\varepsilon}_J$ and ω_J are given in degrees.

$p_{\rm lab}$(MeV/c)		100	200	300	400	500	600	700	800	900	1000
$^{13}D_3$	η_D	1.00	1.00	0.97	0.89	0.74	0.58	0.47	0.42	0.41	0.41
	$\bar{\delta}_D$	0.02	0.47	2.52	7.07	13.52	19.85	24.11	24.78	21.37	14.52
–	ω_3	−0.24	−1.04	−1.71	−1.68	−0.63	1.37	4.05	7.18	10.92	15.92
	$\bar{\varepsilon}_3$	−0.01	−0.41	−1.59	−3.29	−5.03	−6.37	−7.10	−7.34	−7.44	−7.86
$^{13}G_3$	η_G	1.00	1.00	1.00	1.00	1.00	1.00	1.00	0.99	0.99	0.96
	$\bar{\delta}_G$	0.00	0.03	0.23	0.57	0.94	1.26	1.61	2.16	3.07	4.40
$^{33}D_3$	η_D	1.00	1.00	1.00	0.99	0.96	0.91	0.84	0.76	0.68	0.61
	$\bar{\delta}_D$	0.00	0.08	0.56	1.97	4.68	8.61	13.05	16.96	19.53	20.49
–	ω_3	0.10	0.42	0.71	0.79	0.57	0.01	−0.85	−1.96	−3.23	−4.57
	$\bar{\varepsilon}_3$	0.00	0.14	0.51	1.05	1.67	2.33	3.04	3.86	4.92	6.38
$^{33}G_3$	η_G	1.00	1.00	1.00	1.00	1.00	1.00	1.00	0.99	0.99	0.97
	$\bar{\delta}_G$	0.00	−0.01	−0.07	−0.20	−0.37	−0.56	−0.71	−0.79	−0.71	−0.35
$^{13}F_4$	η_F	1.00	1.00	1.00	1.00	0.99	0.96	0.92	0.87	0.82	0.79
	$\bar{\delta}_F$	0.00	0.04	0.29	0.96	2.25	4.16	6.50	8.79	10.48	11.18
–	ω_4	−0.10	−0.45	−0.93	−1.23	−1.20	−0.76	0.15	1.59	3.63	6.36
	$\bar{\varepsilon}_4$	0.00	−0.08	−0.52	−1.26	−2.19	−3.19	−4.18	−5.10	−5.91	−6.64
$^{13}H_4$	η_H	1.00	1.00	1.00	1.00	1.00	1.00	1.00	1.00	1.00	1.00
	$\bar{\delta}_H$	0.00	0.00	0.06	0.21	0.43	0.70	0.99	1.27	1.57	1.88
$^{33}F_4$	η_F	1.00	1.00	1.00	1.00	1.00	1.00	1.00	0.99	0.98	0.95
	$\bar{\delta}_F$	0.00	0.00	−0.01	0.05	0.29	0.80	1.62	2.69	3.86	4.86
–	ω_4	−0.93	−2.63	−3.95	−4.78	−5.30	−5.65	−5.91	−6.14	−6.36	−6.57
	$\bar{\varepsilon}_4$	0.00	0.03	0.17	0.41	0.72	1.05	1.41	1.77	2.15	2.56
$^{33}H_4$	η_H	1.00	1.00	1.00	1.00	1.00	1.00	1.00	1.00	1.00	1.00
	$\bar{\delta}_H$	0.00	0.00	−0.02	−0.07	−0.15	−0.25	−0.36	−0.46	−0.54	−0.59

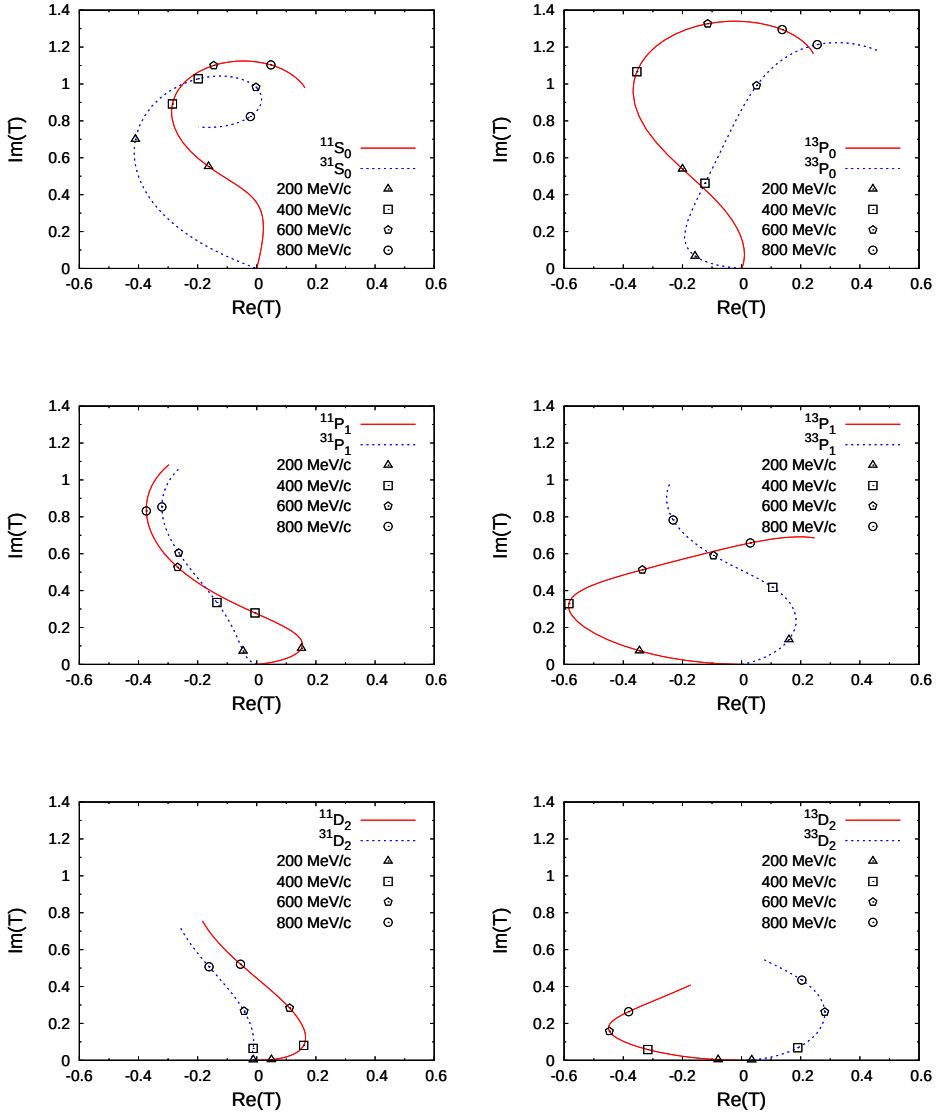

Figure 3.14: The Argand diagrams for the uncoupled S, P, and D waves, assuming isospin symmetry. The solid red line indicates the isospin singlet part and the dotted blue line indicates the isospin triplet part. The symbols on the lines denote the values of the antiproton laboratory momenta. The laboratory momentum runs from 1 to 1000 MeV/c.

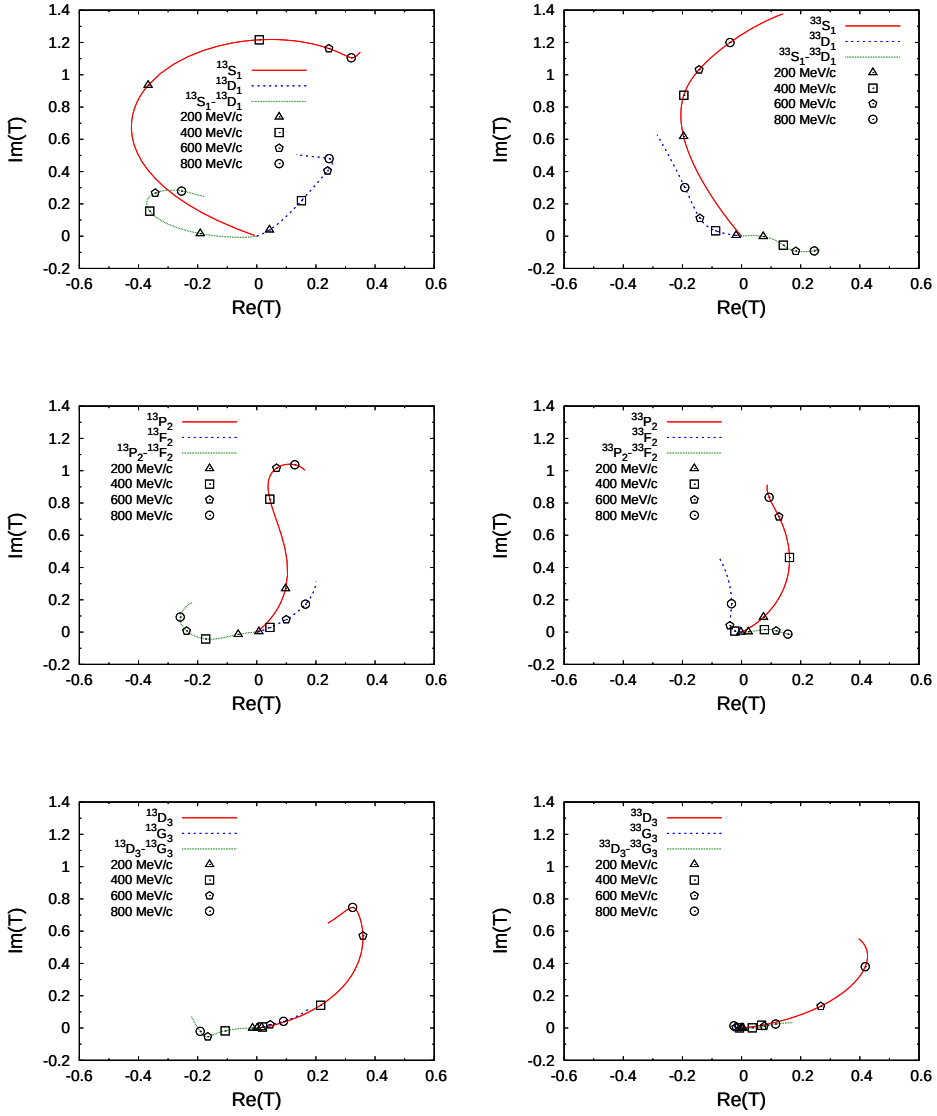

Figure 3.15: The Argand diagrams for the coupled S-D, P-F, and D-G waves, assuming isospin symmetry. The solid red line and the dotted blue line indicate the diagonal parts and the small-dotted green line indicates the mixing part. The symbols on the lines denote the values of the antiproton laboratory momenta. The laboratory momentum runs from 1 to 1000 MeV/c.

3.4 Quality of the database

In this section, we study in more detail the statistical quality of the final database of antiproton-proton scattering, by investigating the distribution of the contributions of the individual data points to the total χ^2, $\chi^2_{\rm tot}$ and the lowest moments and central moments together with their errors [45].

In the PWA, the distribution of the contributions of the ($N_{\rm dat} = 3749$) individual data points to the total χ^2 is given by

$$P_{1,\rm analysis}(\chi^2) = \frac{1}{N_{\rm dat}} \sum_{i=1}^{N_{\rm dat}} \delta(\chi^2 - \chi^2_i) \ . \tag{3.12}$$

In Figure 3.16 we plot this distribution as a histogram and compare it to the theoretical χ^2 distribution for 1 degree of freedom

$$P_1(\chi^2) = \frac{1}{\sqrt{2\pi}} (\chi^2)^{-1/2} e^{-\chi^2/2} \ . \tag{3.13}$$

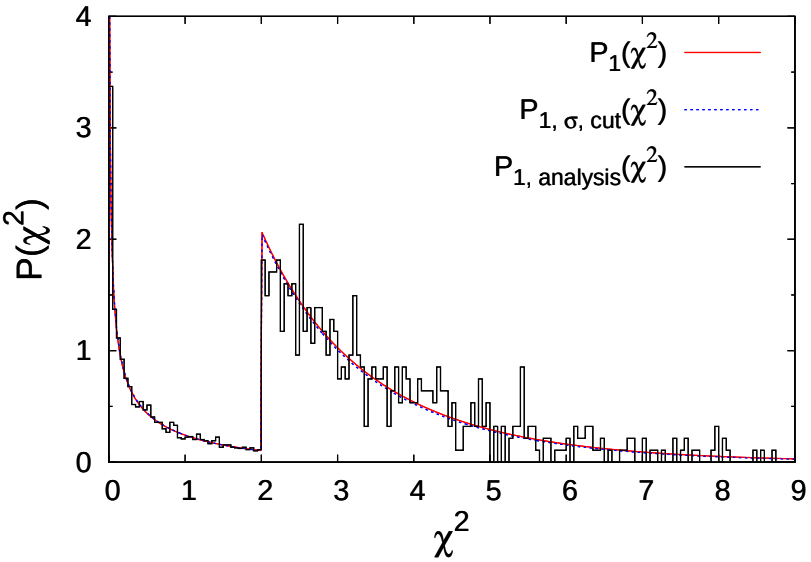

Figure 3.16: Probability distribution functions versus χ^2. The solid red line indicates $P_1(\chi^2)$; the dotted blue line indicates $P_{1,\sigma,\rm cut}(\chi^2)$; and the solid black histogram-line indicates $P_{1,\rm analysis}(\chi^2)$. The tails, with the values $\chi^2 > 2$, are enlarged by a factor of 20. The histogram contains 3749 data points in bins with $\Delta\chi^2 = 0.05$.

Table 3.10: Moments μ'_n and central moments μ_n of the database of the PWA and of the two theoretical probability distribution functions. The errors are given for $N_{\rm dat} = 3749$, where the contributions of the normalization data are included.

Moments Central moments	$P_1(\chi^2)$	$P_{1,\sigma,\rm cut}(\chi^2)$	$P_{1,\rm analysis}(\chi^2)$
μ'_1	1.00 ± 0.02	0.95 ± 0.02	1.00 ± 0.02
μ'_2	3.00 ± 0.16	2.59 ± 0.11	2.80 ± 0.12
μ'_3	15.0 ± 1.6	10.7 ± 0.7	11.8 ± 0.8
μ'_4	105 ± 23	56 ± 5	62 ± 6
μ_2	2.00 ± 0.12	1.67 ± 0.08	1.80 ± 0.08
μ_3	8.0 ± 1.3	5.1 ± 0.5	5.4 ± 0.5
μ_4	60 ± 18	26.8 ± 3.1	28.5 ± 3.1

In order to make this comparison quantitative, we give the moments, the central moments, and the corresponding errors for the distributions. For a distribution $P(t)$, with $t \geq 0$, one defines the moments μ'_n and the central moments μ_n by

$$\mu'_n = \int_0^\infty dt P(t)\, t^n \ , \tag{3.14a}$$

$$\mu_n = \int_0^\infty dt P(t)(t - \mu'_1)^n \ , \tag{3.14b}$$

respectively. The first moment is the mean. The second central moment is the variance. The third central moment indicates the lopsidedness (or skewness) of the distribution. The fourth central moment indicates the "kurtosis" of the distribution. The errors on the moments are given by

$$\sigma_{\mu'_n} = \left[\frac{\mu'_{2n} - (\mu'_n)^2}{N_{\rm dat}}\right]^{1/2} \ , \tag{3.15}$$

and similarly for the errors of the central moments σ_{μ_n}. The lowest moments and central moments with their errors are given in Table 3.10. The agreement between the moments of $P_1(\chi^2)$ and $P_{1,\rm analysis}(\chi^2)$ is reasonable, but not perfect.

In fact, for two reasons $P_1(\chi^2)$ is not the best distribution to compare with. First, while the first moment of $P_1(\chi^2)$ is $\mu'_1 = 1$, that of $P_{1,\rm analysis}(\chi^2)$ is $\mu'_1 = \chi^2_{\rm tot}/N_{\rm dat}$. Since ideally $\langle\chi^2_{\rm tot}\rangle = N_{\rm df}$, we should compare to a narrower distribution $P(\chi^2) = \beta^{-1}P_1(\beta^{-1}\chi^2)$ with $\beta = N_{\rm df}/N_{\rm dat}$. Second, the data points with individual $\chi^2_i > 9$

were rejected, which affects the tail of the distribution and the higher (central) moments. Therefore, it is better to compare $P_{1,\mathrm{analysis}}(\chi^2)$ to

$$P_{1,\sigma,\mathrm{cut}}(\chi^2) = \left[\sigma\sqrt{2}\gamma\left(\frac{1}{2},\frac{9}{2}\sigma^{-2}\right)\right]^{-1}(\chi^2)^{-1/2}\,e^{-\chi^2/(2\sigma^2)}\theta(9-\chi^2)\ , \qquad (3.16)$$

where $\gamma(s,z) = \int_0^z t^{s-1}e^{-t}dt$ is the lower incomplete gamma function and σ is a constant chosen to satisfy $\langle\chi^2\rangle = N_{\mathrm{df}}/N_{\mathrm{dat}}$. In our case, $N_{\mathrm{df}} = 3578$ and $N_{\mathrm{dat}} = 3749$ and so $N_{\mathrm{df}}/N_{\mathrm{dat}} = 0.954$; therefore, we have $\sigma = 0.989$ and $\gamma(\frac{1}{2},\frac{9}{2\sigma^2}) = 1.768$. The Heaviside step function $\theta(9-\chi^2)$ removes the tail with $\chi^2 > 9$. $P_{1,\sigma,\mathrm{cut}}(\chi^2)$ is also plotted in Figure 3.16 and its lowest moments and central moments with errors are given in Table 3.10 as well. The agreement between the (central) moments of $P_{1,\mathrm{analysis}}(\chi^2)$ and $P_{1,\sigma,\mathrm{cut}}(\chi^2)$ is good, which implies that the χ^2 distribution of the PWA is close to what is expected for statistical data.

Chapter 4

Polarization of an Antiproton Beam[‡]

4.1 Towards polarized antiprotons

The invention of stochastic cooling [142] made it possible to accumulate antiprotons in a high-quality beam. As a result, the $\bar{N}N$ interaction could be studied at the LEAR facility at CERN. Experimental data of good quality could be obtained down to antiproton momenta of about 200 MeV/c. The observables measured were mostly differential cross sections for antiproton-proton elastic and charge-exchange scattering. With a polarized proton target the analyzing power for elastic [116, 118, 119, 131] and charge-exchange [121, 126, 135, 143] scattering was measured for a number of antiproton momenta, as well as first data for the depolarization parameter in elastic [127] and charge-exchange [122, 136] scattering, and as well as the spin-transfer parameter in charge-exchange [137] scattering. It has always been a dream of the antiproton physics community to have available a high-quality polarized antiproton beam. In recent years definite plans have been proposed, for instance by the PAX collaboration [4, 5], for a physics program with polarized antiprotons. Experiments with a polarized antiproton beam and a polarized proton target would give full access to the complicated spin dependence of the $\bar{N}N$ interaction and could help to unveil the spin structure of the (anti)proton and test predictions of nonperturbative QCD. The filtering mechanism [63–66] is a possible way to obtain a polarized antiproton beam. Within a certain scattering angle, which is called the acceptance angle, the (elastic) scattered particles can

[‡]Chapters 4 and 5 are based on: D. Zhou and R. G. E. Timmermans, *Polarization observables in low-energy antiproton-proton scattering*, submitted for publication.

still remain in the beam and thus can be scattered again in the next revolution. If the cross sections are spin dependent, the number of particles which remain in the beam are different for different spin states and thus after some time the remaining beam built up some spin polarization. To obtain a polarized beam in this way is the so-called filtering mechanism. In this chapter, we will study how to obtain a noticeable polarization of an antiproton beam based on the PWA discussed in the previous chapters and by using the filtering mechanism [63–66]. The cross-section differences between the antiparallel- and parallel-spin case in the transverse and longitudinal situation with respect to the total charge-exchange cross section are shown for the charge-exchange scattering.

4.2 Spin-dependent cross sections

In this section, the spin-dependent cross sections are studied for $\bar{p}p$ scattering. The contributions to the cross sections from the Coulomb interaction and the nuclear interactions are taken into account. The contributions from the magnetic-moment interaction and vacuum polarization are ignored, because they are negligible.

As input we use the scattering amplitudes predicted by our PWA. The scattering amplitude in spin space for a certain momentum and angle is the sum of the electromagnetic and nuclear contributions. Because the filtering mechanism involves forward scattering of a circulating beam, care has to be taken with the treatment of electromagnetic effects [87]. The electromagnetic amplitude, in particular the standard Coulomb scattering amplitude, is infinite at zero scattering angle. In reality, of course, the Coulomb interaction is screened at very large distances. Since it is not known how to treat this long-range screening, the overall phase of the Coulomb amplitude is unknown. The same holds for the nuclear amplitude. This implies that electromagnetic effects cannot be separated completely from nuclear effects. The nuclear amplitude contains remnants of the electromagnetic interaction, and one cannot properly define e.g. the concept of a total hadronic cross section.

The use of a nonzero acceptance angle alleviates the problems associated with extreme forward scattering. Partially integrated elastic and charge-exchange cross sections can be calculated by integrating the differential cross sections for angles bigger than the acceptance angle. The annihilation amplitude, however, cannot be calculated theoretically. Instead, the annihilation cross section has to be obtained by using the optical theorem for the total $\bar{p}p$ cross section and subtracting the

elastic and charge-exchange cross sections. However, since the optical theorem again involves the forward scattering amplitude, it is strictly speaking not valid for scattering of charged particles [87]. With these caveats in mind, we first review briefly the formalism and then present our results.

The contributions to the cross section for $\bar{p}p$ scattering can be written as

$$\sigma = \sigma_C + \sigma_N + \sigma_I \ , \tag{4.1}$$

where σ_C is the contribution from the Coulomb interaction; the contribution from the nuclear (strong) interaction is

$$\sigma_N = \sigma_{N\mathrm{el}} + \sigma_{\mathrm{ce}} + \sigma_{\mathrm{ann}} \ , \tag{4.2}$$

with $\sigma_{N\mathrm{el}}$ the nuclear-elastic contribution (in the presence of Coulomb but without the contributions from the Coulomb and interference), σ_{ce} the charge-exchange contribution and σ_{ann} the annihilation contribution; and σ_I is the contribution from the interference between the Coulomb and the nuclear interaction. The elastic cross section (with the Coulomb contribution included) is given by

$$\sigma_{\mathrm{el}} = \sigma_C + \sigma_{N\mathrm{el}} + \sigma_I \ . \tag{4.3}$$

With some certain acceptance angle larger than zero, σ_C, σ_I, and of course $\sigma_{N\mathrm{el}}$, σ_{ce} can be calculated exactly. However, as mentioned before, this is not the case for the annihilation cross section σ_{ann} because the annihilation process is not understood. It turns out, however, that the contributions within the acceptance angles considered here to $\sigma_{N\mathrm{el}}$ and σ_{ce} are relatively small, and we assume that is the case for σ_{ann} as well. Therefore, as an approximation, the annihilation contribution can be obtained by $\sigma_{\mathrm{ann}} = \sigma_N - \sigma_{N\mathrm{el}} - \sigma_{\mathrm{ce}}$, where σ_N is obtained by the optical theorem which is independent of the acceptance angle. The optical theorem gives the relation between the total cross section and the imaginary part of the elastic scattering amplitude at zero scattering angle, which is

$$\sigma_{\mathrm{tot}} = \frac{4\pi}{p}\mathrm{Im}\left[M(\theta = 0)\right] \ , \tag{4.4}$$

where p is the momentum of the incoming particles and $M(\theta)$ is the elastic scattering amplitude at the scattering angle θ in the center-of-mass system.

In order to study the polarization, one needs to calculate the cross sections in spin space. First, let us define the cross-section differences between the antiparallel- and parallel-spin case in the transverse and longitudinal (with respect to the direction

of the incident particle) situation, given by

$$\Delta\sigma_{\perp} = \sigma_{\uparrow\downarrow} - \sigma_{\uparrow\uparrow} \ , \tag{4.5a}$$

$$\Delta\sigma_{\parallel} = \sigma_{\rightleftarrows} - \sigma_{\rightrightarrows} \ , \tag{4.5b}$$

where the double arrows mean antiparallel or parallel spins of the beam and target particles. The spin-dependent cross sections can then be written as (in Refs. [63, 64, 66, 144], it was written in a similar but different notation)

$$\sigma = \sigma_{\rm tot} - \frac{1}{2}\Delta\sigma_{\perp}(\boldsymbol{\zeta}_B\cdot\boldsymbol{\zeta}_T) - \frac{1}{2}(\boldsymbol{\zeta}_B\cdot\hat{\boldsymbol{p}})(\boldsymbol{\zeta}_T\cdot\hat{\boldsymbol{p}})(\Delta\sigma_{\parallel} - \Delta\sigma_{\perp}) \ , \tag{4.6}$$

where $\boldsymbol{\zeta}_B$ and $\boldsymbol{\zeta}_T$ are the unit polarization vectors of the beam and target, respectively; $\hat{\boldsymbol{p}}$ is the unit vector in the direction of the beam momentum; $\sigma_{\rm tot}$ is the integrated spin-independent cross section. If $\Sigma_{S\mu}$ denotes the integrated cross section with the total spin of the beam and target particles S with z-component μ, then one has

$$\sigma_{\rm tot} = \frac{1}{2}\Sigma_{11} + \frac{1}{4}(\Sigma_{10} + \Sigma_{00}) \ , \tag{4.7a}$$

$$\Delta\sigma_{\perp} = -\frac{1}{2}(\Sigma_{10} - \Sigma_{00}) \ , \tag{4.7b}$$

$$\Delta\sigma_{\parallel} = -\Sigma_{11} + \frac{1}{2}(\Sigma_{10} + \Sigma_{00}) \ . \tag{4.7c}$$

Therefore, once the $\Sigma_{S\mu}$'s are known, $\Delta\sigma_{\perp}$ and $\Delta\sigma_{\parallel}$ can be obtained. The amplitudes of the different contributions in spin space should be known in order to calculate $\Sigma_{S\mu}$. The Coulomb amplitudes are spin independent and the elastic scattering part is given by Eq. (2.11)

$$\langle s'm'|M_C(\theta)|s\,m\rangle = -\delta_{ss'}\delta_{mm'}\,\frac{\eta}{2p}\frac{e^{2i\sigma_0}}{(\sin^2\frac{1}{2}\theta)^{1+i\eta}} \ . \tag{4.8}$$

There is no Coulomb amplitude for the charge-exchange scattering. The nuclear amplitudes contain the contributions from the nuclear elastic, charge-exchange, and annihilation interactions. The nuclear elastic and charge-exchange amplitudes in spin space are in matrix notation given by

$$\langle s'm'|M^C_{C+N}(\theta)|s\,m\rangle = \sum_{\ell\,\ell'\,J}\sqrt{4\pi(2\ell+1)}\,i^{\ell-\ell'}\,C^{\ell\ s\ J}_{0\ m\ m}\,C^{\ell'\ s'\ J}_{m-m'\ m'\ m}\,Y^{\ell'}_{m-m'}(\theta)$$
$$\langle\ell's'|S_C^{1/2}\left(S^C_{C+N}-1\right)S_C^{1/2}|\ell\,s\rangle/(2ip) \ , \tag{4.9}$$

where $|\ell'-\ell| = 0,\ 2$; S^C_{C+N} is the nuclear S matrix in the presence of Coulomb force. It should be understood that S_C is an identity matrix for charge-exchange scattering. Given the amplitudes, the $\Sigma_{S\mu}$'s and therefore $\sigma_{\rm tot}$, $\Delta\sigma_{\perp}$, and $\Delta\sigma_{\parallel}$ can be calculated.

4.3 Polarization results

In this section, the polarization of an antiproton beam are studied by using the filtering mechanism [63–66]. The relations of the polarizations and the cross sections in spin space are given. The polarization results are presented with acceptance angles $\theta_{\rm acc}^{\rm lab} = 5$, 10, 20, and 30 mrad in the laboratory frame.

Once the cross sections in spin space are known, the polarizations of the beam can be obtained by the filtering mechanism. It has turned out that the polarization due to the filtering mechanism dominates [66] and the polarization due to the spin-flip mechanism can be ignored, which has also been verified by the experiment at COSY at Jülich [67]. Therefore, the effects due to the spin-flip mechanism are ignored.

Suppose $N_+(t)$ and $N_-(t)$ are the number of beam particles with spin "up" and spin "down," respectively, at the time t. The initial condition is $N_+(0) = N_-(0)$, since the beam is unpolarized initially. The number of beam particles as a function of time is given by

$$N(t) = \frac{1}{2}N(0)\left[e^{-\Omega_-^{\rm out}t} + e^{-\Omega_+^{\rm out}t}\right] \ , \tag{4.10}$$

where $\Omega_\pm^{\rm out}$ characterize how many particles with spin "up" or "down" are scattered out of the acceptance angle (for more details, see Ref. [66]). For the target with a noticeable polarization, the polarization of the beam is given by

$$P_B(t) = \frac{N_+(t) - N_-(t)}{N_+(t) + N_-(t)} = \tanh\left[\frac{\rm t}{2}(\Omega_-^{\rm out} - \Omega_+^{\rm out})\right] \ . \tag{4.11}$$

The relation of $\Omega_\pm^{\rm out}$ and the cross sections in spin space is given by

$$\Omega_\pm^{\rm out} = nf\left\{\sigma_{\rm tot} \mp \frac{1}{2}P_T\left[\Delta\sigma_\perp + (\zeta_T\cdot\hat{\boldsymbol{p}})^2(\Delta\sigma_\parallel - \Delta\sigma_\perp)\right]\right\} \ , \tag{4.12}$$

where n is the areal density of the target and f is the revolution frequency of the beam; P_T is the polarization of the target. If $\left|\Omega_-^{\rm out} - \Omega_+^{\rm out}\right| \ll \left|\Omega_-^{\rm out} + \Omega_+^{\rm out}\right|$, as in the case discussed in Refs. [63, 64, 66], the beam life time is given by

$$\tau_B = \frac{2}{\Omega_-^{\rm out} + \Omega_+^{\rm out}} = \frac{1}{nf\sigma_{\rm tot}} \ . \tag{4.13}$$

The figure of merit, defined by ${\rm FOM}(t) = P_B^2(t)N(t)$, is maximal at $t = t_0 = 2\tau_B$. The polarizations at t_0 are given by

$$P_B(t_0) = P_\perp(t_0) = P_T\frac{\Delta\sigma_\perp}{\sigma_{\rm tot}} \ , \qquad \text{when } \ \zeta_T\cdot\hat{\boldsymbol{p}} = 0 \ ; \tag{4.14a}$$

$$P_B(t_0) = P_\parallel(t_0) = P_T\frac{\Delta\sigma_\parallel}{\sigma_{\rm tot}} \ , \qquad \text{when } \ \zeta_T\cdot\hat{\boldsymbol{p}} = \pm 1 \ . \tag{4.14b}$$

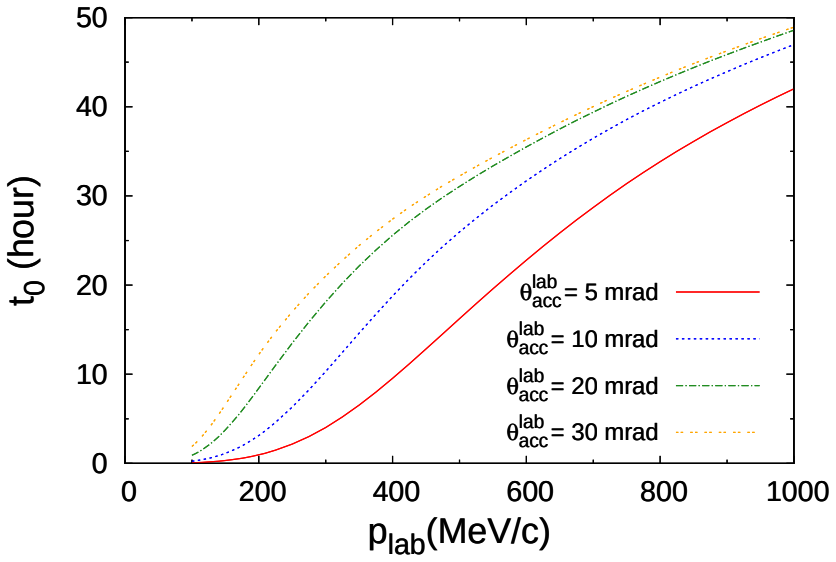

Figure 4.1: The t_0 with the areal density of the target $n = 10^{14}$ cm^{-2} and the revolution frequency of the beam $f = 10^6$ s^{-1} for acceptance angles $\theta^{\rm lab}_{\rm acc} = 5$, 10, 20, and 30 mrad in the laboratory frame. The solid red line indicates the result for $\theta^{\rm lab}_{\rm acc} = 5$ mrad; the dotted blue line indicates the result for $\theta^{\rm lab}_{\rm acc} = 10$ mrad; the dot-dashed green line indicates the result for $\theta^{\rm lab}_{\rm acc} = 20$ mrad; and the double-dotted orange line indicates the result for $\theta^{\rm lab}_{\rm acc} = 30$ mrad.

In Figure 4.1 the t_0 as a function of momentum in the laboratory frame is plotted with $n = 10^{14}$ cm^{-2} and $f = 10^6$ s^{-1} (these values are the same as the ones used in Refs. [63, 64]) for acceptance angles $\theta^{\rm lab}_{\rm acc} = 5$, 10, 20, and 30 mrad in the laboratory frame. One can see that $t_0 < 50$ hour for all of the acceptance angles considered here.

In Figure 4.2 the integrated cross sections, the integrated interference cross sections, and the beam polarizations are given at time t_0 for different acceptance angles (assuming $P_T = 1$). One can see that the interferences are important at lower energies. It can be concluded from the figures that a noticeable polarization can be achieved. For the target with polarization perpendicular to the direction of the incoming beam (transverse, $P_B = P_\perp$), the maximal beam polarization is around -15%, which of course depends on the acceptance angle. At momenta around $p_{\rm lab} = 350$ MeV/c, the polarization can reach about -20% with acceptance angle $\theta^{\rm lab}_{\rm acc} = 30$ mrad. Even with acceptance angle $\theta^{\rm lab}_{\rm acc} = 5$ mrad, there is about -10% polarization at momenta around $p_{\rm lab} = 550$ MeV/c. When the momen-

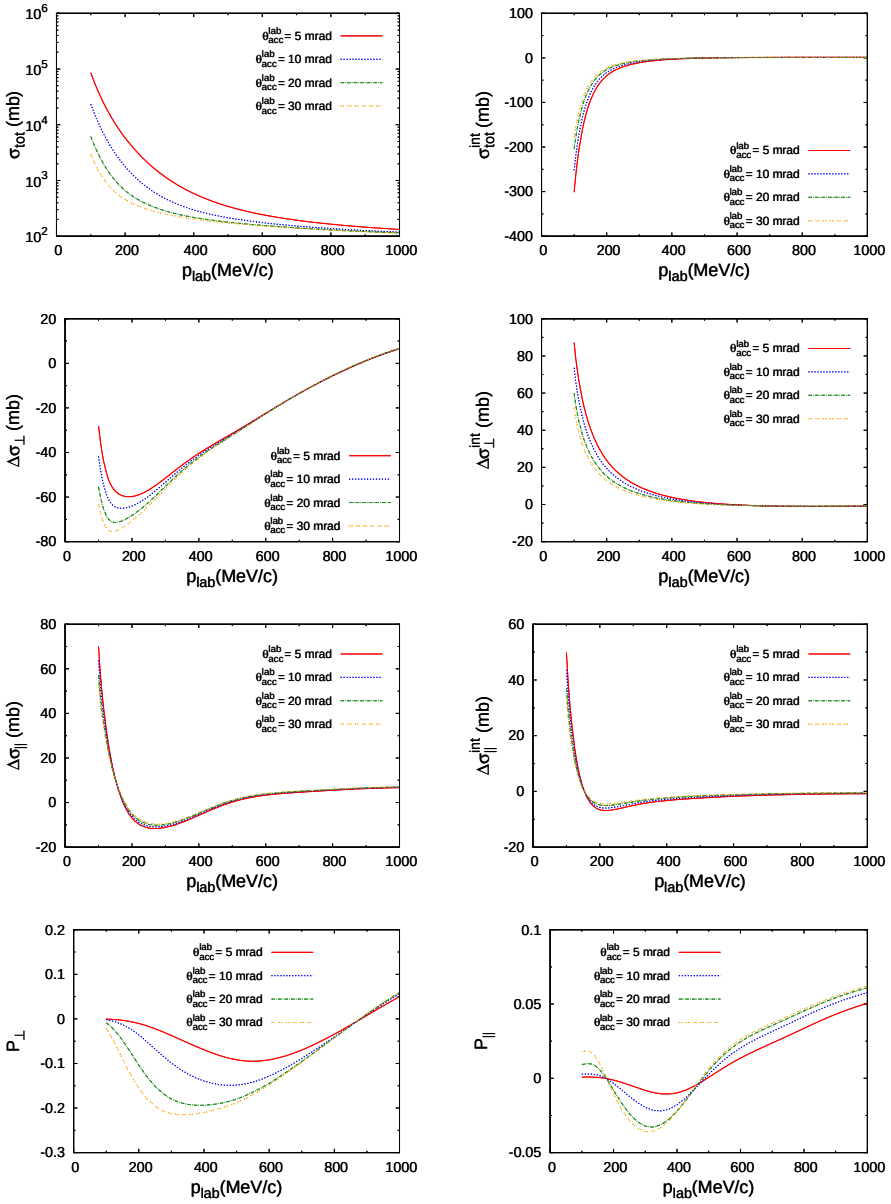

Figure 4.2: The cross sections $\sigma_{\rm tot}$, the interference cross sections $\sigma_{\rm tot}^{\rm int}$, the differences of the transverse and longitudinal cross sections $\Delta\sigma_\perp$, $\Delta\sigma_\parallel$, and the polarizations $P_\perp$, $P_\parallel$ at time t_0 for acceptance angles $\theta_{\rm acc}^{\rm lab} = 5$, 10, 20, and 30 mrad. The solid red lines indicate the results for $\theta_{\rm acc}^{\rm lab} = 5$ mrad; the dotted blue lines indicate the results for $\theta_{\rm acc}^{\rm lab} = 10$ mrad; the dot-dashed green lines indicate the results for $\theta_{\rm acc}^{\rm lab} = 20$ mrad; and the double-dotted orange lines indicate the results for $\theta_{\rm acc}^{\rm lab} = 30$ mrad.

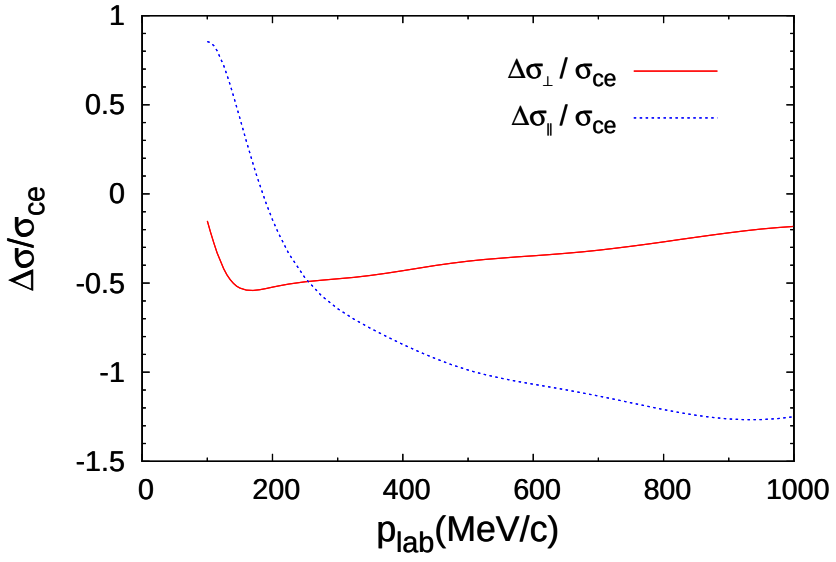

Figure 4.3: The cross-section differences between antiparallel- and parallel-spin case in the transverse and longitudinal situation ($\Delta\sigma_\perp$ and $\Delta\sigma_\parallel$) with respect to the total charge-exchange cross section $\sigma_{\rm ce}$ for the charge-exchange scattering. The solid red line indicates the result for the transverse case and the dotted blue line indicates the result for the longitudinal case.

tum reaches $p_{\rm lab} = 1000$ MeV/c, the polarization is around 5%. For the target with polarization collinear with the direction of the incoming beam (longitudinal, $P_B = P_\parallel$), the maximal beam polarization is around -2% at low energies and 5% at relative high energies. For low energies, at momenta around $p_{\rm lab} = 300$ MeV/c, the polarization can reach about -3% with acceptance angle $\theta^{\rm lab}_{\rm acc} = 30$ mrad; at momenta around $p_{\rm lab} = 350$ MeV/c, the polarization can reach about -1% with acceptance angle $\theta^{\rm lab}_{\rm acc} = 5$ mrad. For high energies, when the momentum is about $p_{\rm lab} = 1000$ MeV/c, the polarizations are between 5% and 6% when the acceptance angle goes from $\theta^{\rm lab}_{\rm acc} = 5$ to 30 mrad. Roughly speaking, the transverse polarization $P_\perp$ can reach higher values than the longitudinal polarization $P_\parallel$, at least in the energy range considered here. A noticeable polarization can be reached in a reasonable time for both $P_\perp$ and $P_\parallel$ in the energy range considered here. The signs of the polarizations imply that the beam polarization has the same direction as the target polarization if the sign is positive, while the beam polarization has the opposite direction as the target polarization if the sign is negative. One can always use a "spin flipper" to change the direction of the spin polarization of particles.

The polarizations of an antiproton beam were also obtained by other authors using different models, for instance by using the Paris $\bar{N}N$ model in Ref. [63], by using the Jülich $\bar{N}N$ models A(BOX) and D in Ref. [5], and by using the Nijmegen $\bar{N}N$ model in Ref. [64]. Though all of the models predict a significant polarization in a reasonable time, the detailed results of the different models are not the same. Sometimes the shapes of the curves are different; sometimes the polarization values have opposite signs around the peaks; and sometimes the positions and magnitudes of the peaks are different.

In Figure 4.3, the cross-section differences between antiparallel- and parallel-spin case in the transverse and longitudinal situation ($\Delta\sigma_{\perp}$ and $\Delta\sigma_{\parallel}$) with respect to the total charge-exchange cross section $\sigma_{\rm ce}$ are shown for the charge-exchange scattering. These very large spin effects, which are due to the tensor force of one- and two-pion exchange, might be tested if a polarized antiproton beam could be realized.

Chapter 5

Spin Observables of Antiproton-Proton Scattering

In this chapter, we follow the notations in Ref. [75] to describe and predict, based on the PWA discussed before, some of the $\bar{p}p$ spin observables for both elastic and charge-exchange scattering.

Let $\boldsymbol{P}_i$ and $\boldsymbol{P}_f$ be the momenta of the beam and scattered particle in the center-of-mass system, respectively. One defines the unit vectors

$$\hat{P} = \frac{\boldsymbol{P}_i + \boldsymbol{P}_f}{|\boldsymbol{P}_i + \boldsymbol{P}_f|} \ , \qquad \hat{K} = \frac{\boldsymbol{P}_f - \boldsymbol{P}_i}{|\boldsymbol{P}_f - \boldsymbol{P}_i|} \ , \qquad \hat{n} = \frac{\boldsymbol{P}_i \times \boldsymbol{P}_f}{|\boldsymbol{P}_i \times \boldsymbol{P}_f|} \ . \tag{5.1}$$

When the two particles in the scattering process have the same mass M, the relation between the scattering angle in the center-of-mass system θ and the scattering angle in the laboratory frame $\theta_{\rm lab}$ is given by

$$\tan\frac{\theta}{2} = \left(1 + \frac{E_{\rm lab}}{2Mc^2}\right)^{1/2} \tan\theta_{\rm lab} \ , \tag{5.2}$$

where $E_{\rm lab}$ is the kinetic energy of the beam particle in the laboratory frame. In the laboratory frame with the nonrelativistic limit, $\hat{P}$ represents the direction of the momentum of the scattered particle, and $\hat{K}$ represents the opposite direction of the momentum of the recoil particle. In the laboratory frame, the direction of the momentum of the scattered particle is denoted by the unit vector $\hat{p}$ and the opposite direction of the momentum of the recoil particle is denoted by the unit vector $\hat{k}$; the direction of the momentum of the incoming particle is denoted by the unit vector $\hat{z}$. The unit vector $\hat{n}$ has the same definition in the center-of-mass

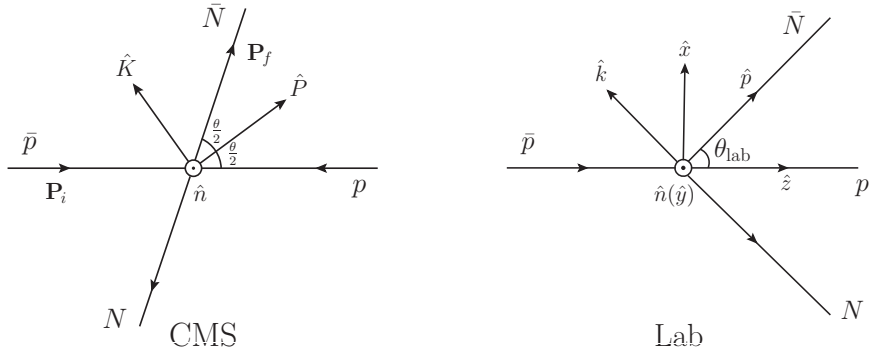

Figure 5.1: The sketch of vectors in the center-of-mass system (labeled by "CMS") and in the laboratory frame (labeled by "Lab"). The $\odot$ means the arrow points perpendicularly out of the page.

system and in the laboratory frame, and sometimes it is also denoted by $\hat{y}$ in the laboratory frame. The unit vector $\hat{x} = \hat{y} \times \hat{z}$. The sketch of these unit vectors can be seen from Figure 5.1.

When $\chi^{(n)}$ is a pure spin state, then the density matrix is given by

$$\rho_{ij} = \sum_n P_n \chi_i^{(n)} \chi_j^{(n)\dagger} \ , \tag{5.3}$$

where P_n is the relative probability for the system to be in the spin state $\chi^{(n)}$. Let S^μ be a spin operator, then its expectation value is given by

$$\langle S^\mu \rangle = \frac{\mathrm{Tr}(\rho S^\mu)}{\mathrm{Tr}\rho} \ , \tag{5.4}$$

where "Tr" means taking the trace of the argument. The final and initial spin expectation values can be related by the scattering amplitudes as

$$I \langle S^\mu \rangle_f = \frac{1}{4} \sum_\nu \mathrm{Tr}\left(M S^\nu M^\dagger S^\mu\right) \langle S^\nu \rangle_i \ , \tag{5.5}$$

where S^μ and S^ν are the final and initial spin operators, respectively; M is the scattering amplitude in the spin space; the differential cross section I is given by

$$I = \frac{1}{4} \sum_\nu \mathrm{Tr}\left(M S^\nu M^\dagger\right) \langle S^\nu \rangle_i \ . \tag{5.6}$$

All the spin observables can be calculated based on these formulas.

Here, we present some of the spin observables of rank-one and rank-two. These observables include analyzing power A_y (or polarization P); depolarization D_{yy}

(or depolarization D); spin transfer K_{yy} (or polarization-transfer parameter D_t); transverse-rotation parameters R and R'; longitudinal-rotation parameters A and A'; polarization-transfer parameters R_t, R'_t, A_t, and A'_t; spin-correlation parameters C_{nn}, C_{kp}, C_{pp}, C_{kk}, and A_{yy}, A_{zz}, A_{xx}, and A_{zx}. The meaning of these observables is demonstrated in Figure 5.2. Some of those figures are different from the ones in Ref. [75], but they are in fact equal based on some symmetry arguments, i.e., charge conjugation, parity, and time-reversal invariance.

The PWA results of these spin observables are plotted in Figures 5.3–5.20 for the laboratory momenta $p_{\rm lab} = 300$, 400, 500, 600, 700, and 800 MeV/c. The left column is for the elastic case and the right column is for the charge-exchange case. As before, the PWA results are given by the solid red lines and the dotted blue lines indicate the one-sigma uncertainty regions. These results are obtained by using the nonrelativistic version of the spin observables in terms of scattering amplitudes [75]. In the energy range considered here, it turns out that the differences between the nonrelativistic case and the relativistic case is very small. The results can be compared with future experimental data.

Figures 5.3–5.5 show the results of analyzing power A_y (or polarization P), depolarization D_{yy} (or depolarization D), and spin transfer K_{yy} (or polarization-transfer parameter D_t), respectively. Some of these observables have been measured at some energies as one can see from Table 3.1. The analyzing power A_y is zero at $\cos\theta = \pm 1$ for both the elastic and charge-exchange case. The elastic depolarization D_{yy} is close to 1 at very forward angles. The charge-exchange depolarization D_{yy} has a peak at forward angles. The charge-exchange spin transfer K_{yy} has also a peak at forward angles, though the peak is smaller than the one of the charge-exchange depolarization D_{yy}.

Figures 5.6–5.9 show the results of transverse-rotation parameters R and R', and polarization-transfer parameters R_t and R'_t, respectively. The absolute value of the transverse-rotation parameter R is normally very small at $\cos\theta = -1$ for both the elastic and charge-exchange case. The elastic transverse-rotation parameter R is close to 1 at very forward angles. The charge-exchange transverse-rotation parameter R is more or less flat except there is a dip-bump structure at forward angles which goes deeper as the energy increases. The absolute value of the transverse-rotation parameter R' is normally very small at $\cos\theta = 1$ for both the elastic and charge-exchange case. The absolute value of the polarization-transfer parameter R_t is very small at $\cos\theta = 1$ for both the elastic and charge-exchange case. The absolute value of the polarization-transfer parameter R'_t is normally very small at $\cos\theta = -1$ for both the elastic and charge-exchange case. The absolute value of

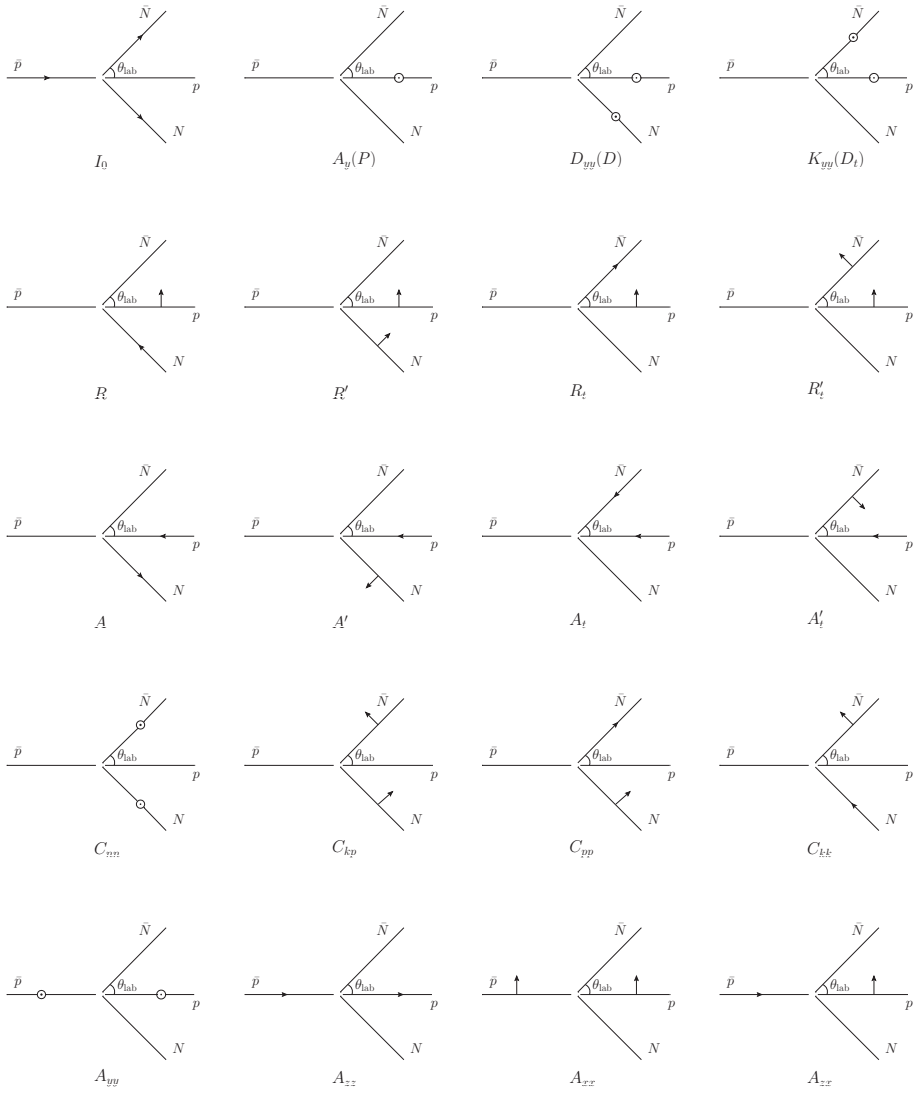

Figure 5.2: Some of the spin observables for $\bar{p}p$ elastic and charge-exchange scattering in the laboratory frame (the first figure is just the sketch of the $\bar{p}p$ scattering). The arrows indicate the directions of spins except that in the first figure (labeled by "I_0") where the arrows indicate the directions of momenta. In the nonrelativistic limit, the direction of the arrow of the spin of scattered particle is collinear with the direction of the momentum of recoil particle, and vice versa. The $\odot$ means the spin points perpendicularly out of the page.

the polarization-transfer parameter R'_t is normally very small at $\cos\theta = 1$ for the elastic case. The charge-exchange polarization-transfer parameter R'_t is large for very forward angles at low energies. This characteristic might be used to produce polarized antineutron beams.

Figures 5.10–5.13 show the results of longitudinal-rotation parameters A and A', and polarization-transfer parameters A_t and A'_t, respectively. The absolute value of the longitudinal-rotation parameter A is normally very small at $\cos\theta = 1$ for both the elastic and charge-exchange case. The longitudinal-rotation parameter A is close to -1 for very backward angles at low energies for the charge-exchange case. The absolute value of the longitudinal-rotation parameter A' is normally very small at $\cos\theta = -1$ for both the elastic and charge-exchange case. The elastic longitudinal-rotation parameter A' is close to 1 at very forward angles. The charge-exchange longitudinal-rotation parameter A' has a dip-bump structure at forward angles and the dip is close to -1 especially at higher energies. The absolute value of the polarization-transfer parameter A_t is normally very small at $\cos\theta = -1$ for both the elastic and charge-exchange case. The polarization-transfer parameter A_t is large for the very forward angles at low energies for the charge-exchange case. This characteristic might also be used to produce polarized antineutron beams, as was suggested in Ref. [22]. The absolute value of the polarization-transfer parameter A'_t is very small at $\cos\theta = 1$ for both the elastic and charge-exchange case. The charge-exchange polarization-transfer parameter A'_t is close to -1 for very backward angles at low energies. Unfortunately, this cannot be used to produce polarized antineutron beams because the differential cross section is very small at backward angles for the charge-exchange case.

Figures 5.14–5.17 show the results for the spin-correlation parameters C_{nn}, C_{kp}, C_{pp}, and C_{kk}, respectively. For the spin-correlation parameter C_{nn}, the maximal magnitude in the charge-exchange case is greater than the one in the elastic case, and at some energies the maximal magnitude is close to 1 in the charge-exchange case. The absolute value of the spin-correlation parameter C_{kp} is very small at $\cos\theta = 1$ and is normally very small at $\cos\theta = -1$ for both the elastic and charge-exchange case. The absolute value of the elastic spin-correlation parameter C_{pp} is very small at $\cos\theta = 1$. The charge-exchange spin-correlation parameters C_{pp} has a very big dip structure at the very forward angles. For the spin-correlation parameter C_{pp}, normally, the maximal magnitude in the charge-exchange case is also greater than the one in the elastic case, and at some energies the maximal magnitude is close to 1 in the charge-exchange case. The elastic spin-correlation parameter C_{kk} is more or less flat in the forward hemisphere except at very forward

angles where there is a small dip structure at low energies. The charge-exchange spin-correlation parameter C_{kk} always has a maximal magnitude which is very close to 1 at some angle in the energy range considered here.

Figures 5.18–5.20 show the results for the spin-correlation parameters A_{zz}, A_{xx}, and A_{zx}, respectively. The value of the spin-correlation parameter A_{yy} is the same as the one of C_{nn} if time reversal is a good symmetry. The absolute value of the elastic spin-correlation parameter A_{zz} is very small at $\cos\theta = 1$. The elastic spin-correlation parameter A_{zz} is close to -1 at low energies at $\cos\theta = -1$. The charge-exchange spin-correlation parameter A_{zz} has a very big dip structure at the very forward angles, and it also has a "plateau" in some angular range in most of the cases. For the spin-correlation parameter A_{zz}, normally, the maximal magnitude in the charge-exchange case is also greater than the one in the elastic case. The absolute value of the elastic spin-correlation parameter A_{xx} is very small at $\cos\theta = 1$. For the spin-correlation parameter A_{xx}, normally, the maximal magnitude in the charge-exchange case is also greater than the one in the elastic case. The absolute value of the spin-correlation parameter A_{zx} is very small at $\cos\theta = 1$ for both the elastic and charge-exchange case, and it is normally very small at $\cos\theta = -1$.

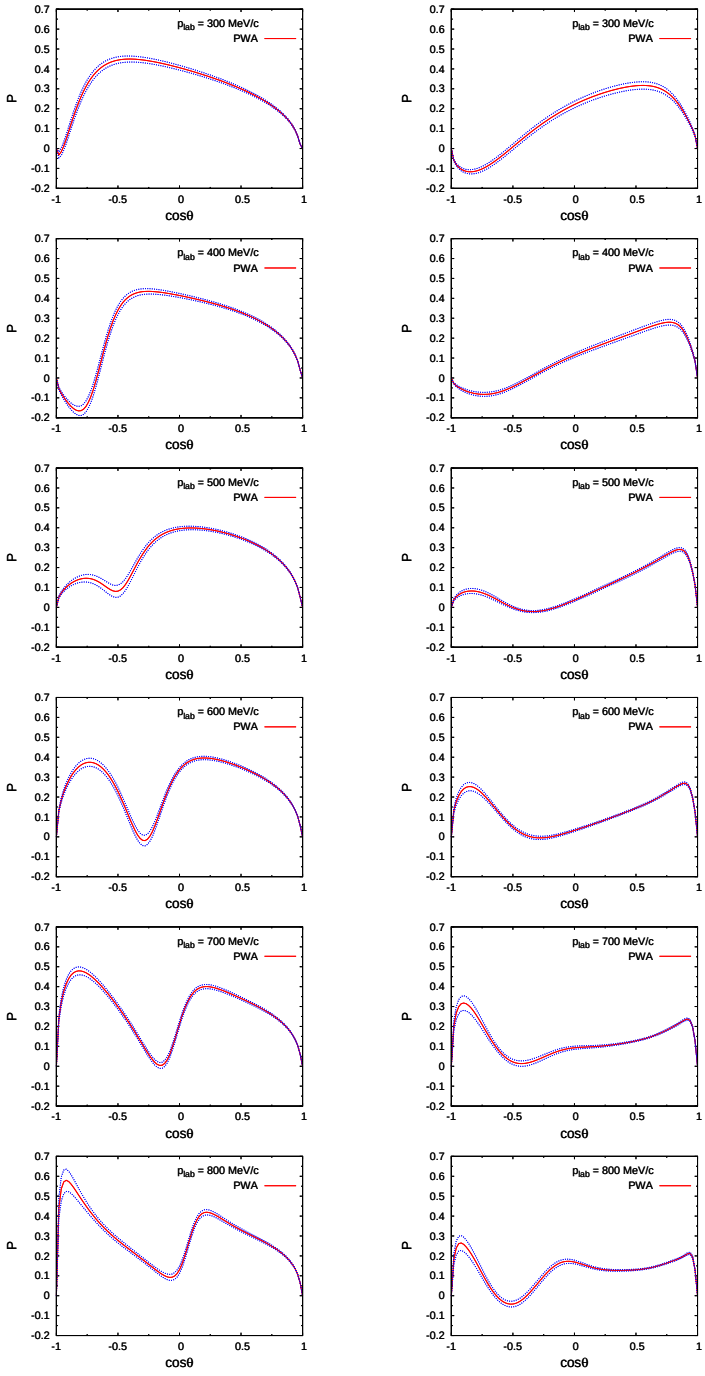

Figure 5.3: The polarization P for $\bar{p}p$ elastic and charge-exchange scattering.

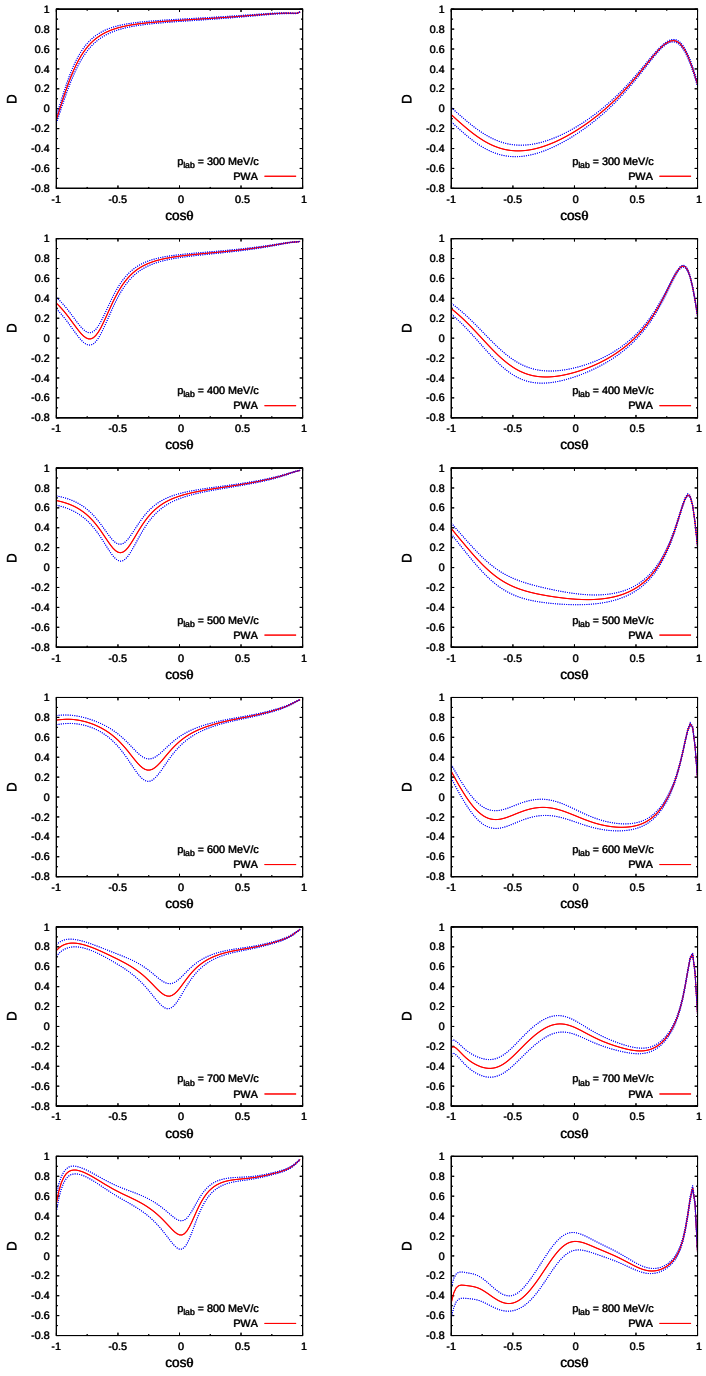

Figure 5.4: The depolarization D for $\bar{p}p$ elastic and charge-exchange scattering.

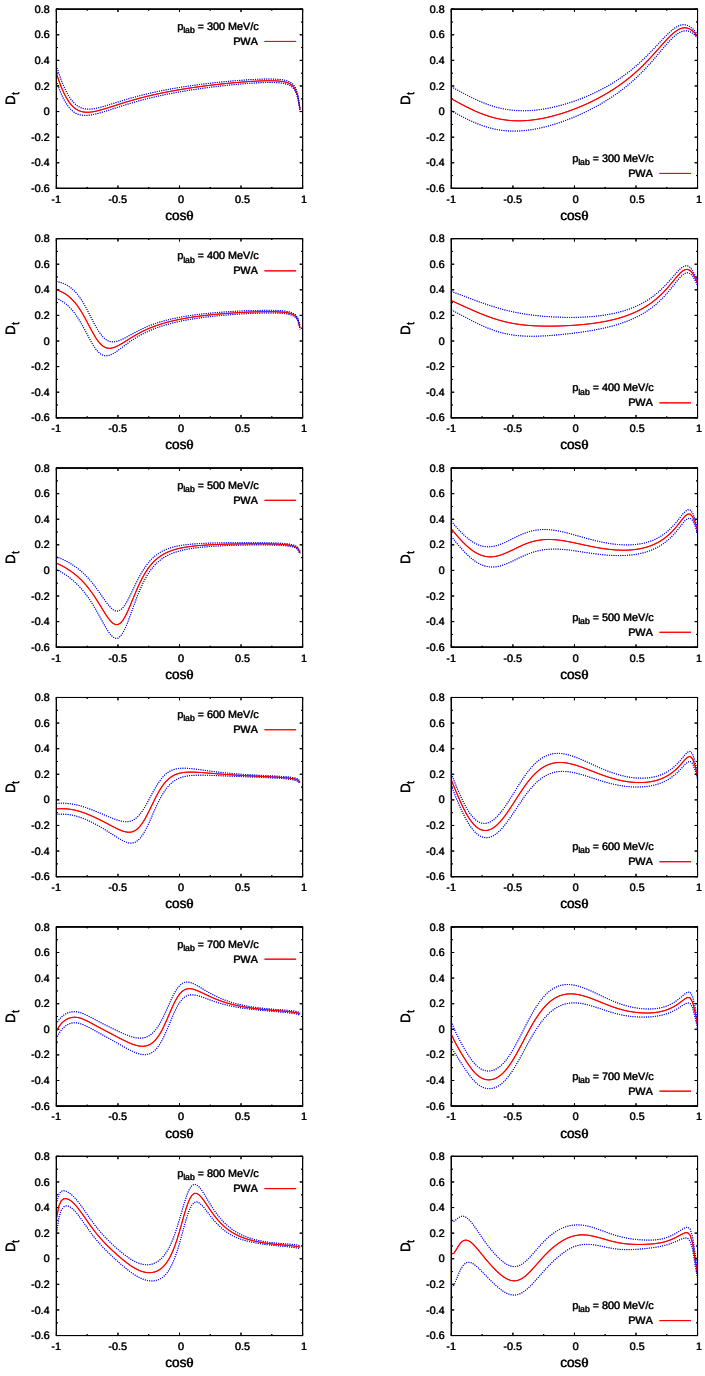

Figure 5.5: The polarization transfer D_t for $\bar{p}p$ elastic and charge-exchange scattering.

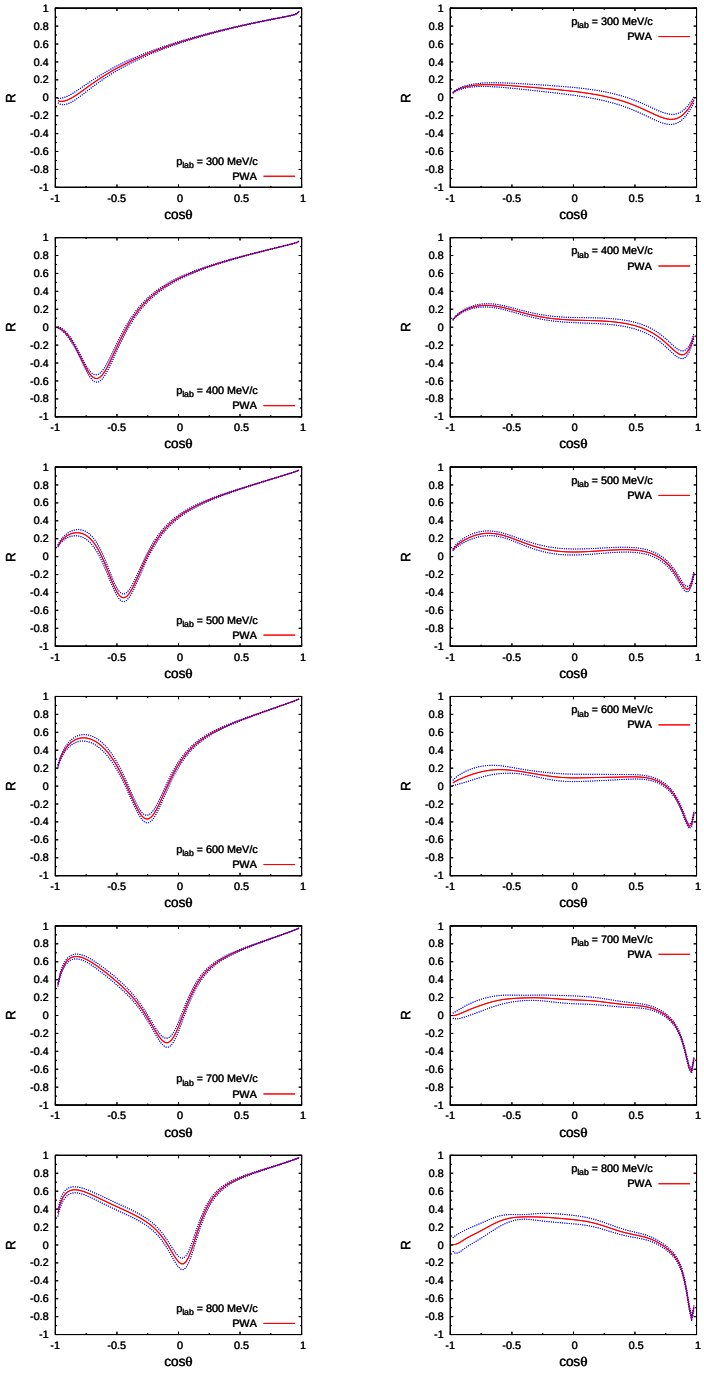

Figure 5.6: The transverse rotation R for $\bar{p}p$ elastic and charge-exchange scattering.

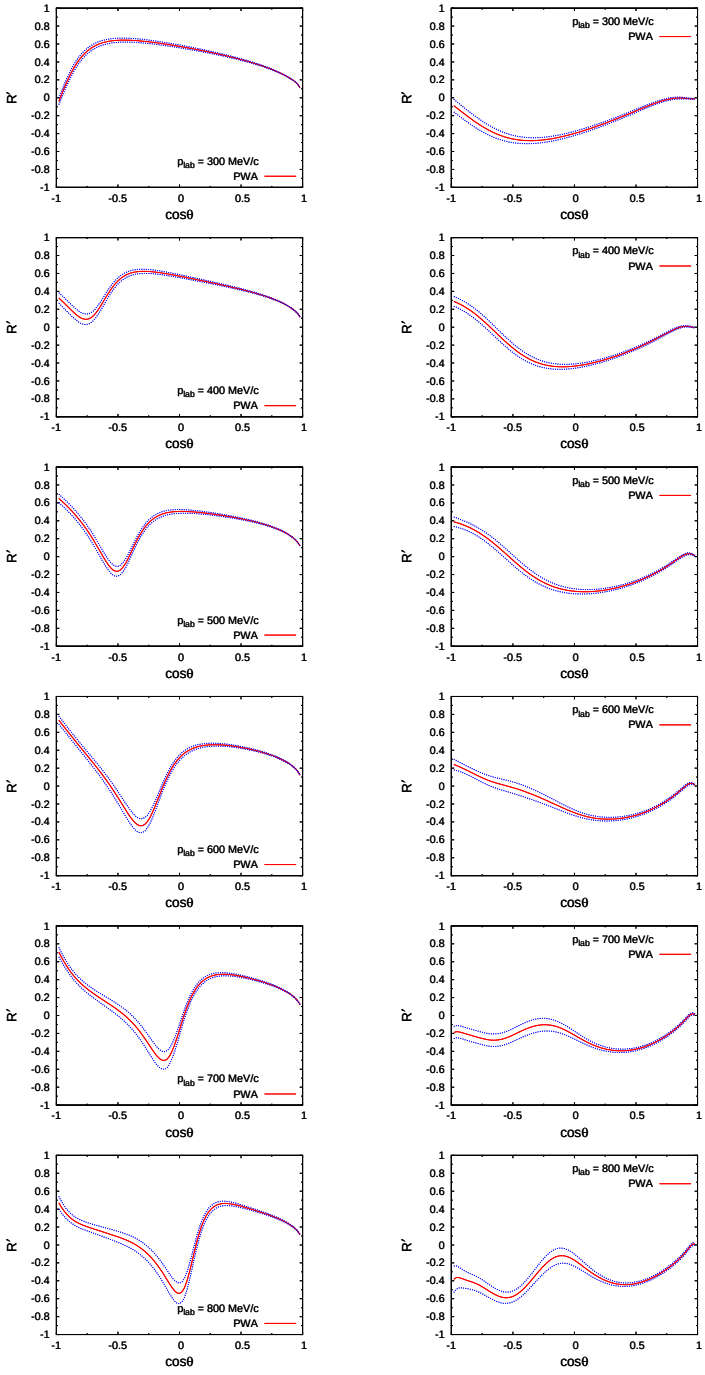

Figure 5.7: The transverse rotation R' for $\bar{p}p$ elastic and charge-exchange scattering.

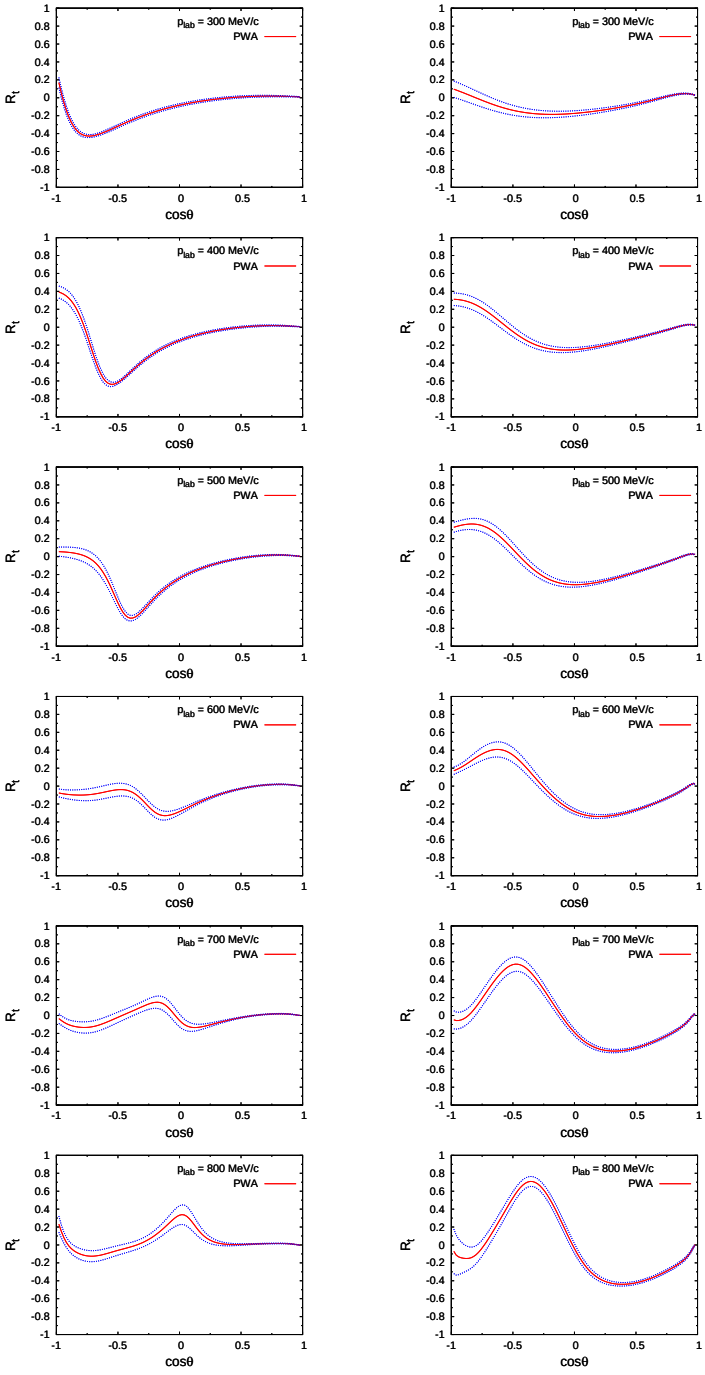

Figure 5.8: The polarization transfer R_t for $\bar{p}p$ elastic and charge-exchange scattering.

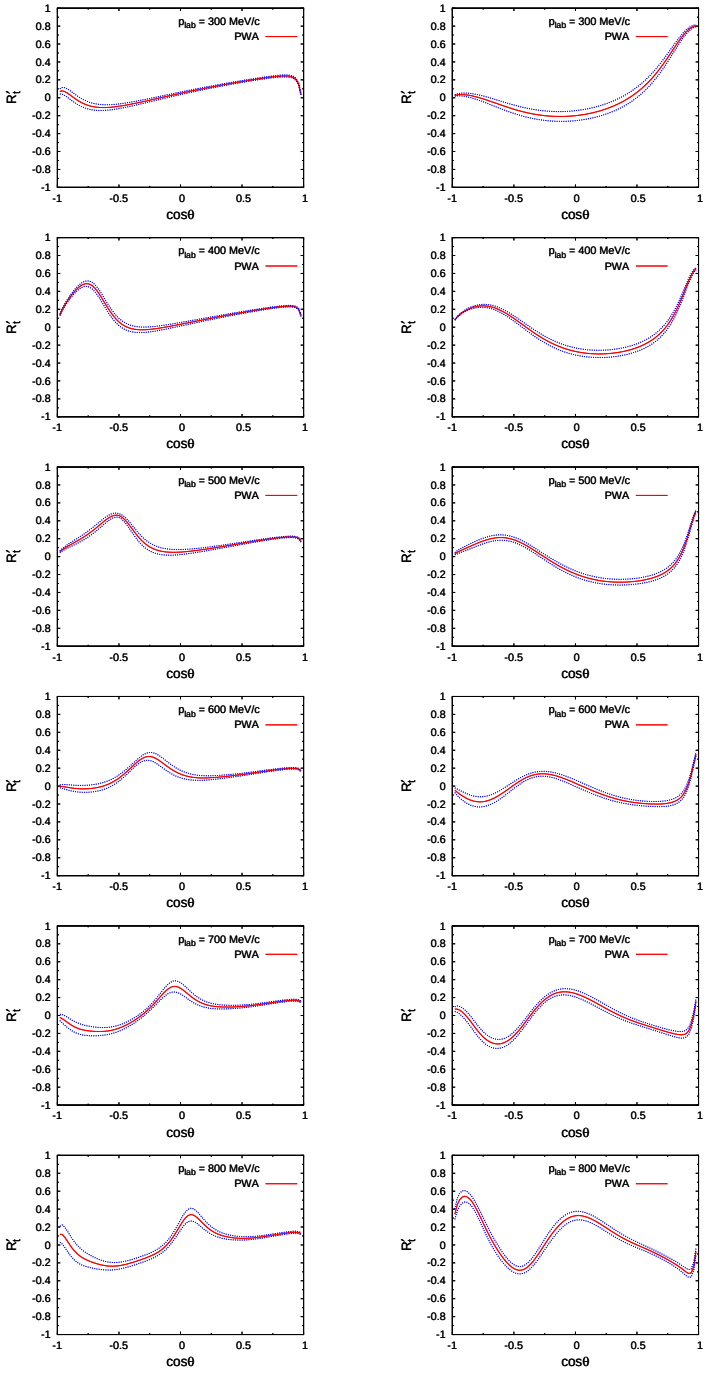

Figure 5.9: The polarization transfer R'_t for $\bar{p}p$ elastic and charge-exchange scattering.

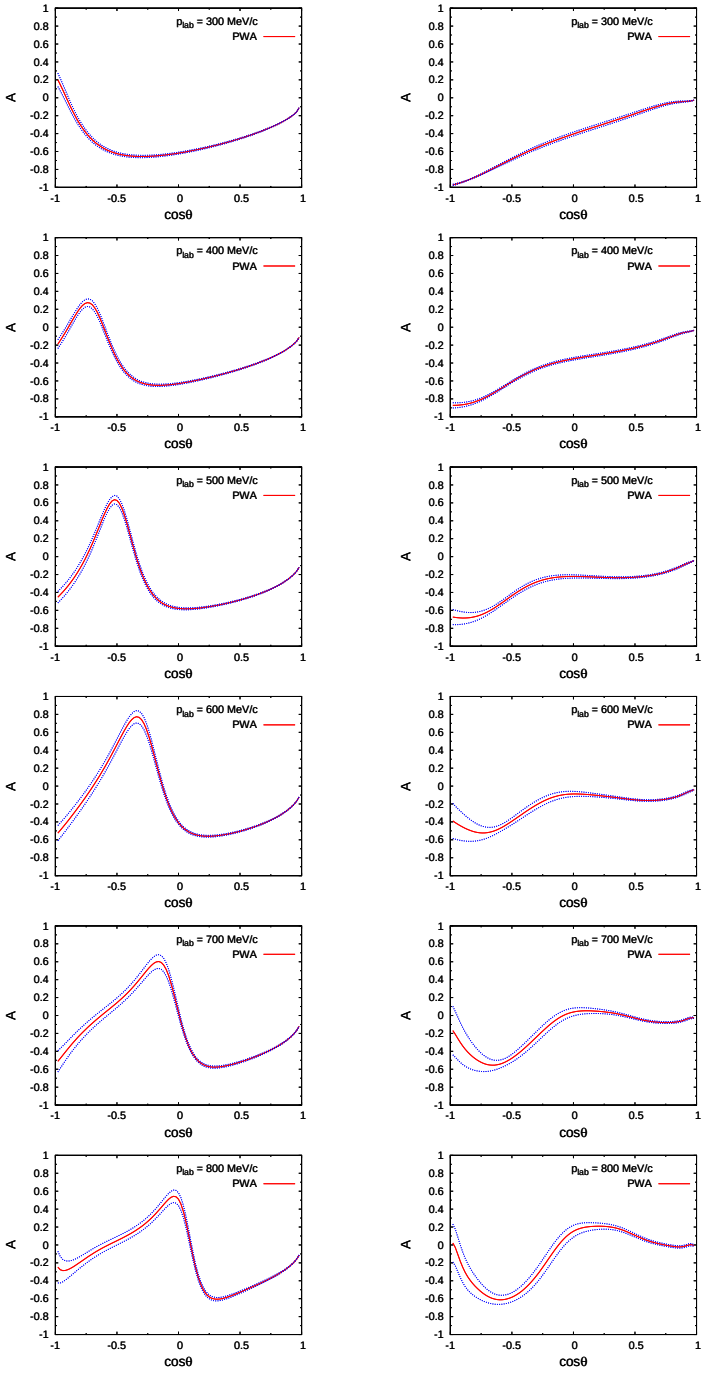

Figure 5.10: The longitudinal rotation A for $\bar{p}p$ elastic and charge-exchange scattering.

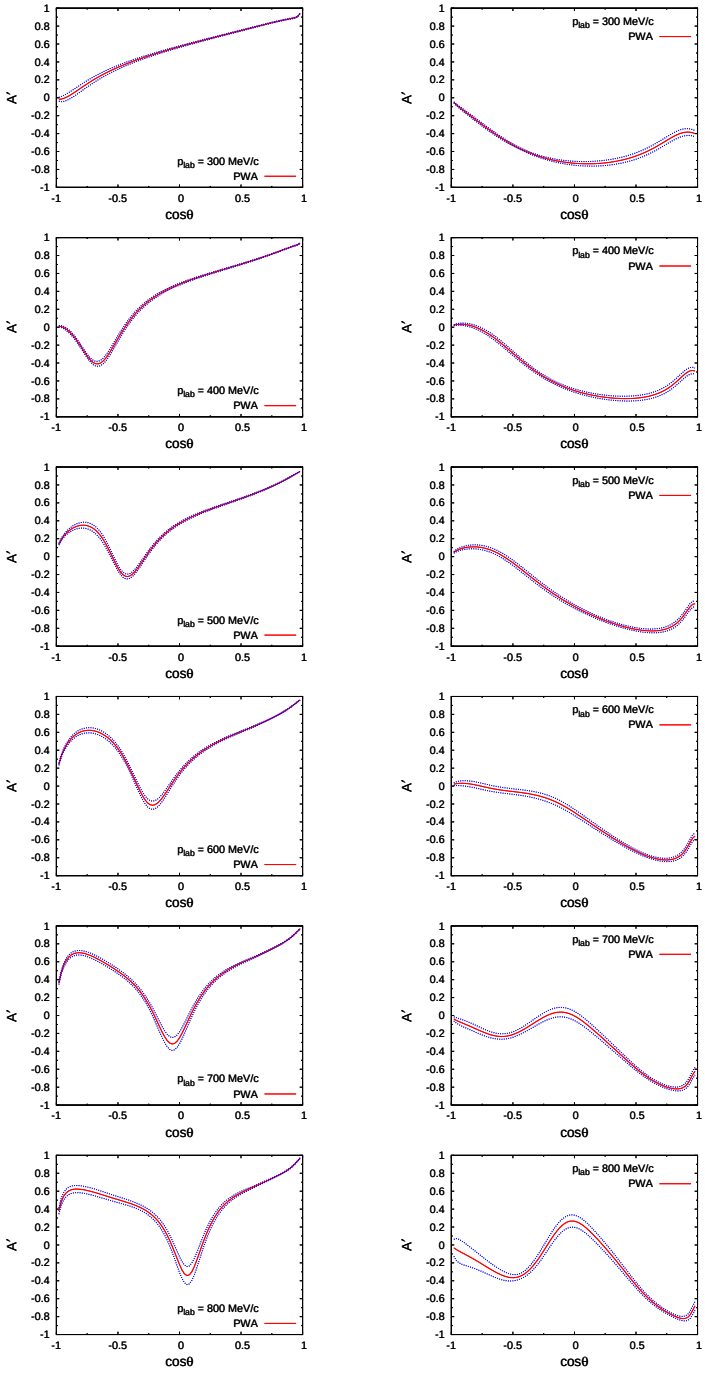

Figure 5.11: The longitudinal rotation A' for $\bar{p}p$ elastic and charge-exchange scattering.

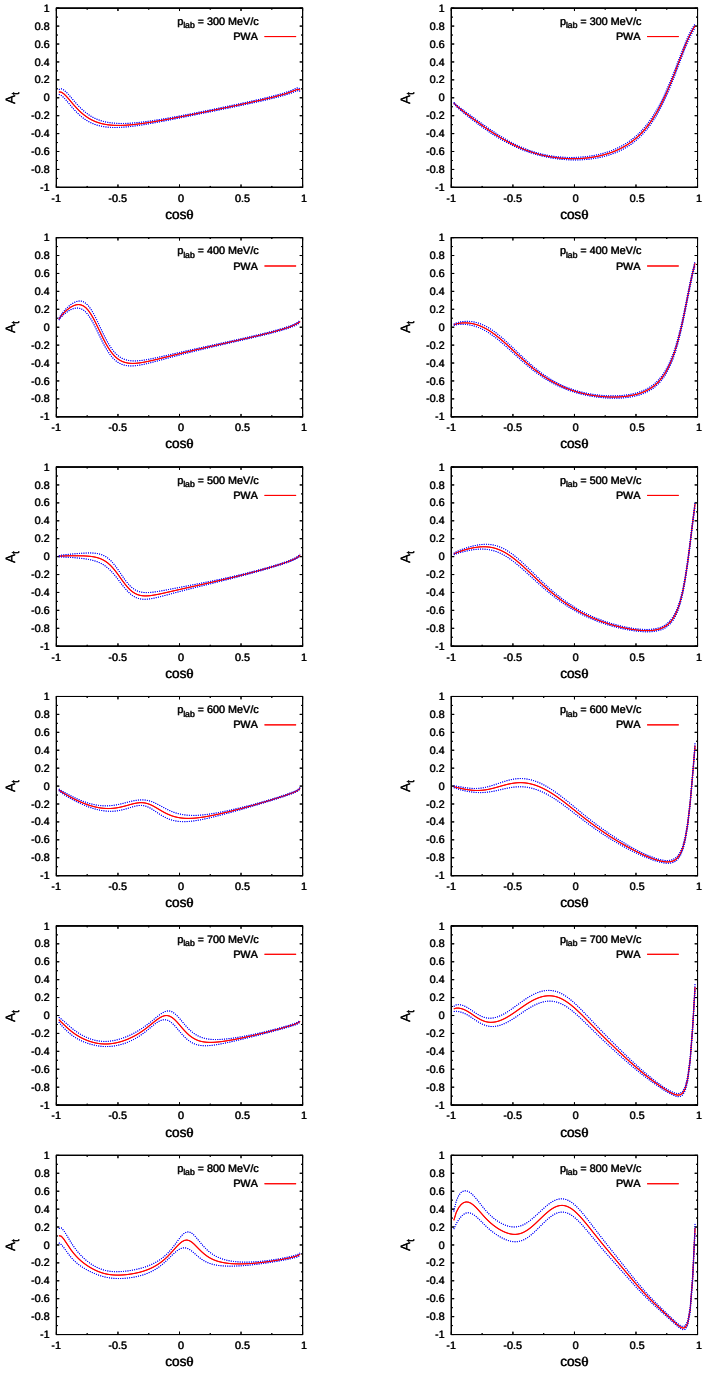

Figure 5.12: The polarization transfer A_t for $\bar{p}p$ elastic and charge-exchange scattering.

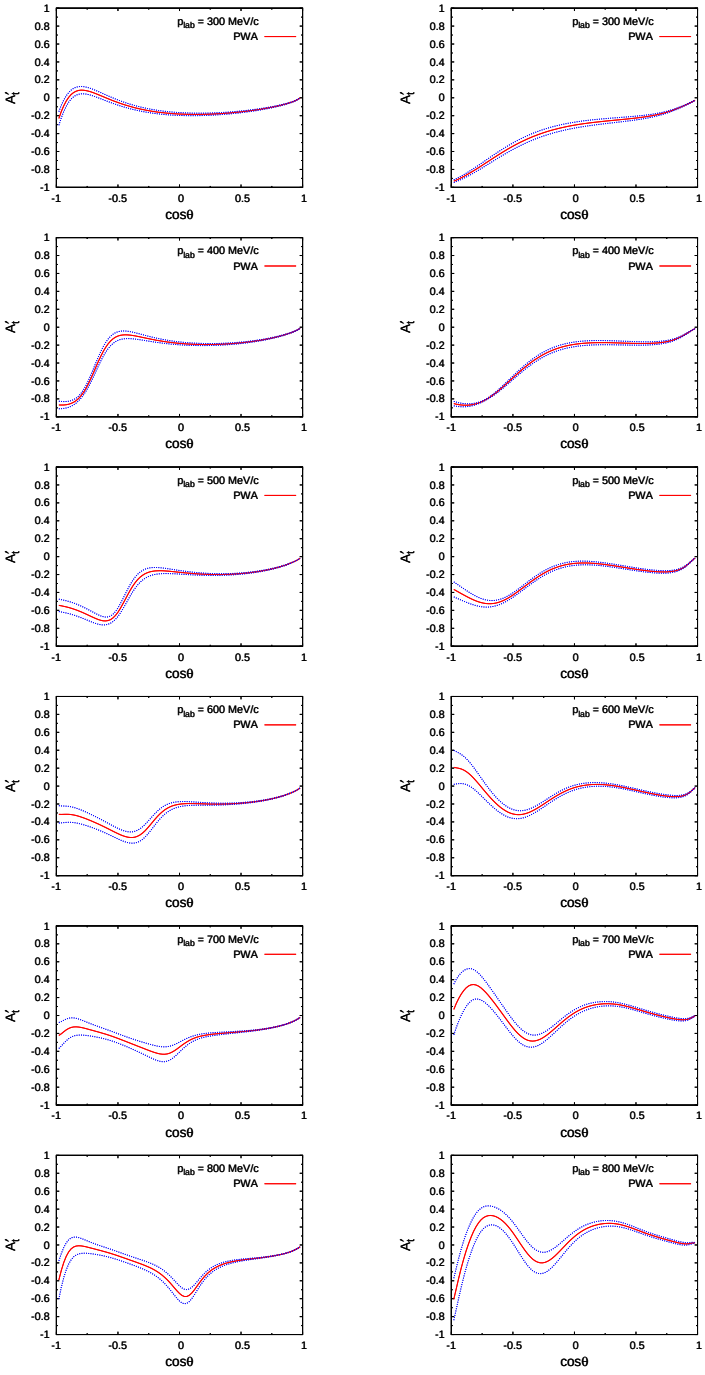

Figure 5.13: The polarization transfer A'_t for $\bar{p}p$ elastic and charge-exchange scattering.

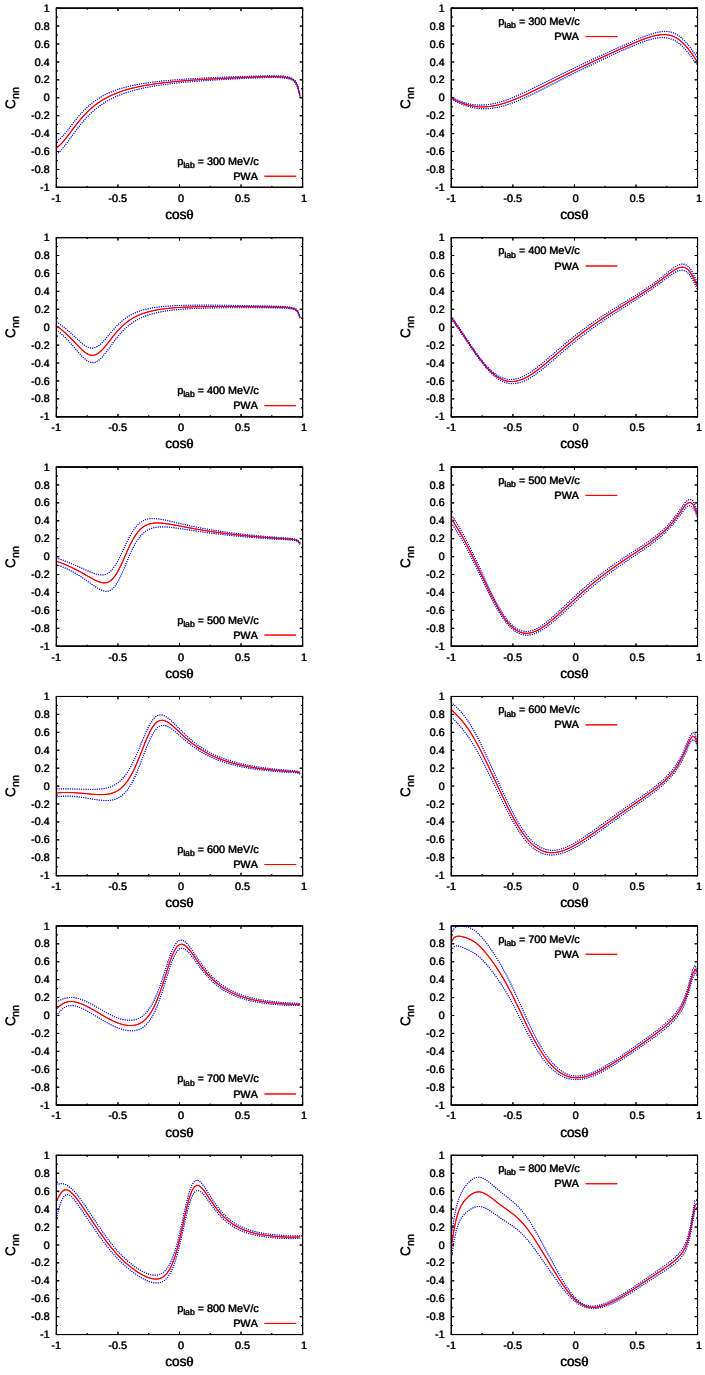

Figure 5.14: The spin correlation C_{nn} for $\bar{p}p$ elastic and charge-exchange scattering.

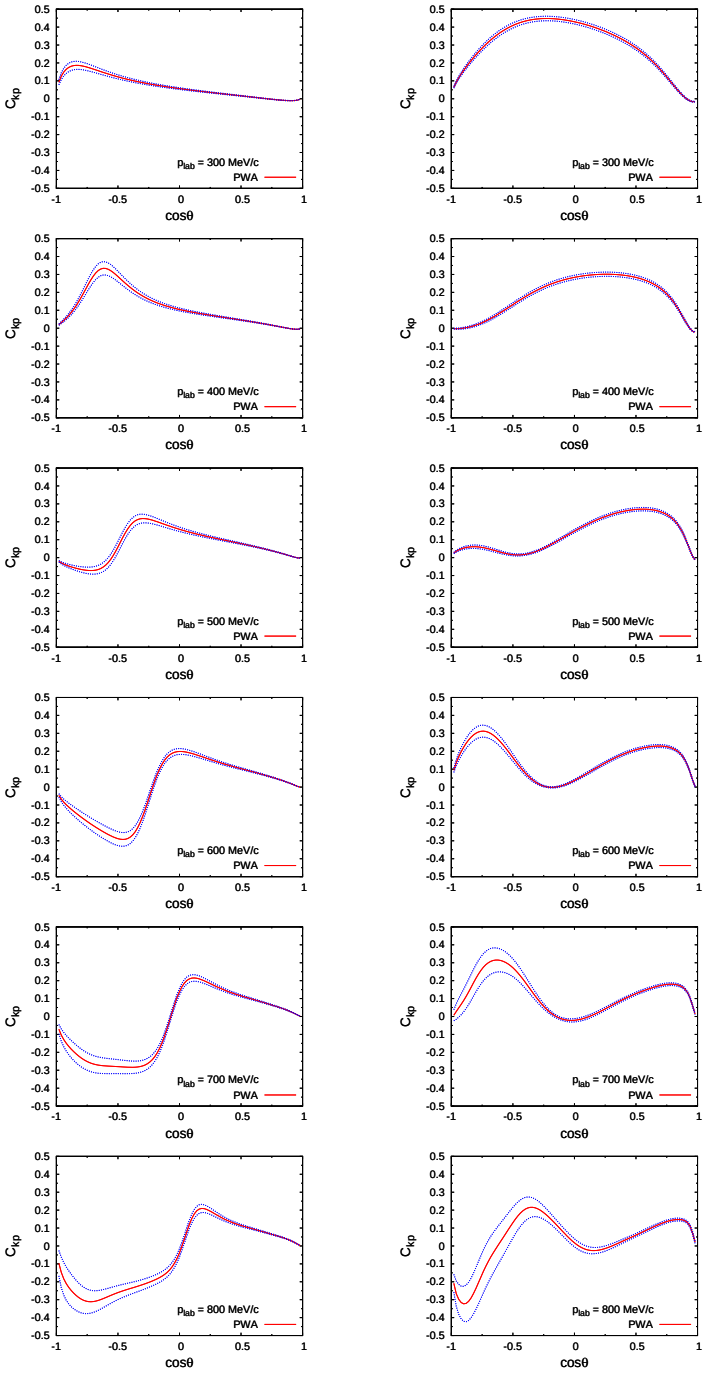

Figure 5.15: The spin correlation C_{kp} for $\bar{p}p$ elastic and charge-exchange scattering.

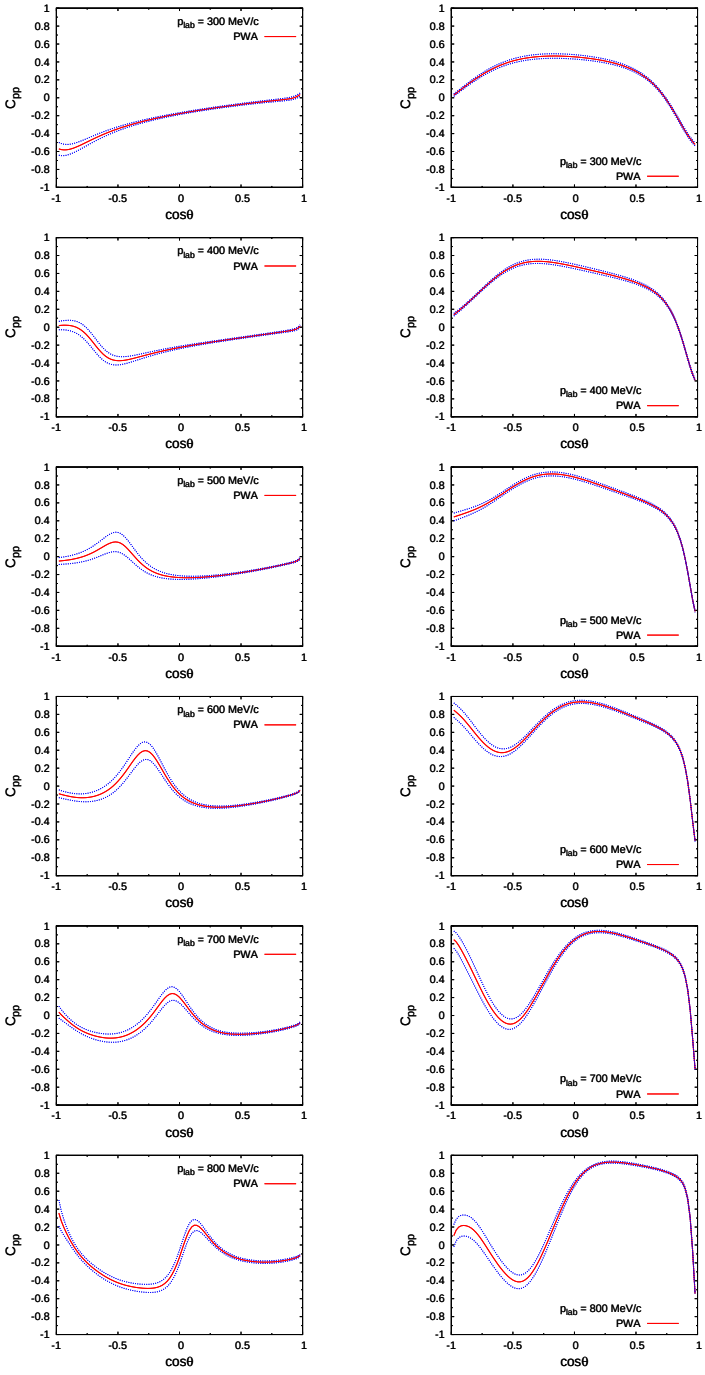

Figure 5.16: The spin correlation C_{pp} for $\bar{p}p$ elastic and charge-exchange scattering.

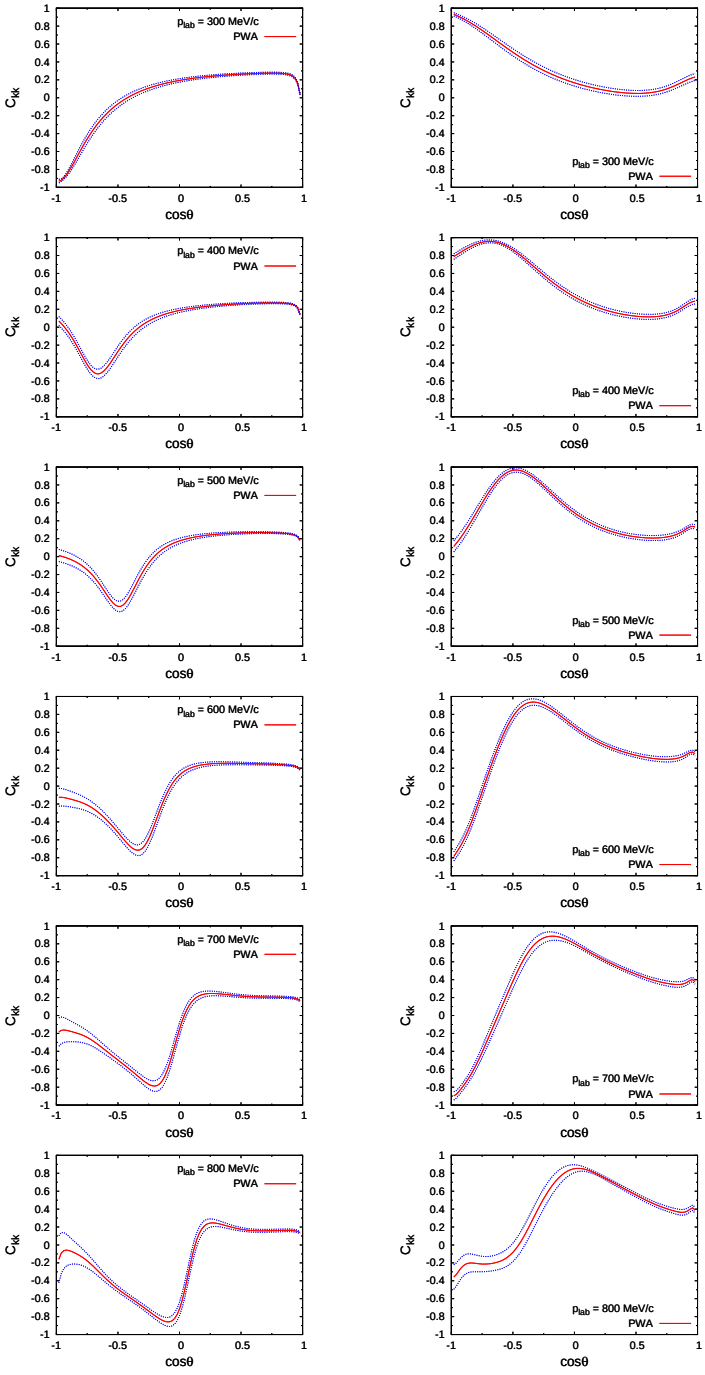

Figure 5.17: The spin correlation C_{kk} for $\bar{p}p$ elastic and charge-exchange scattering.

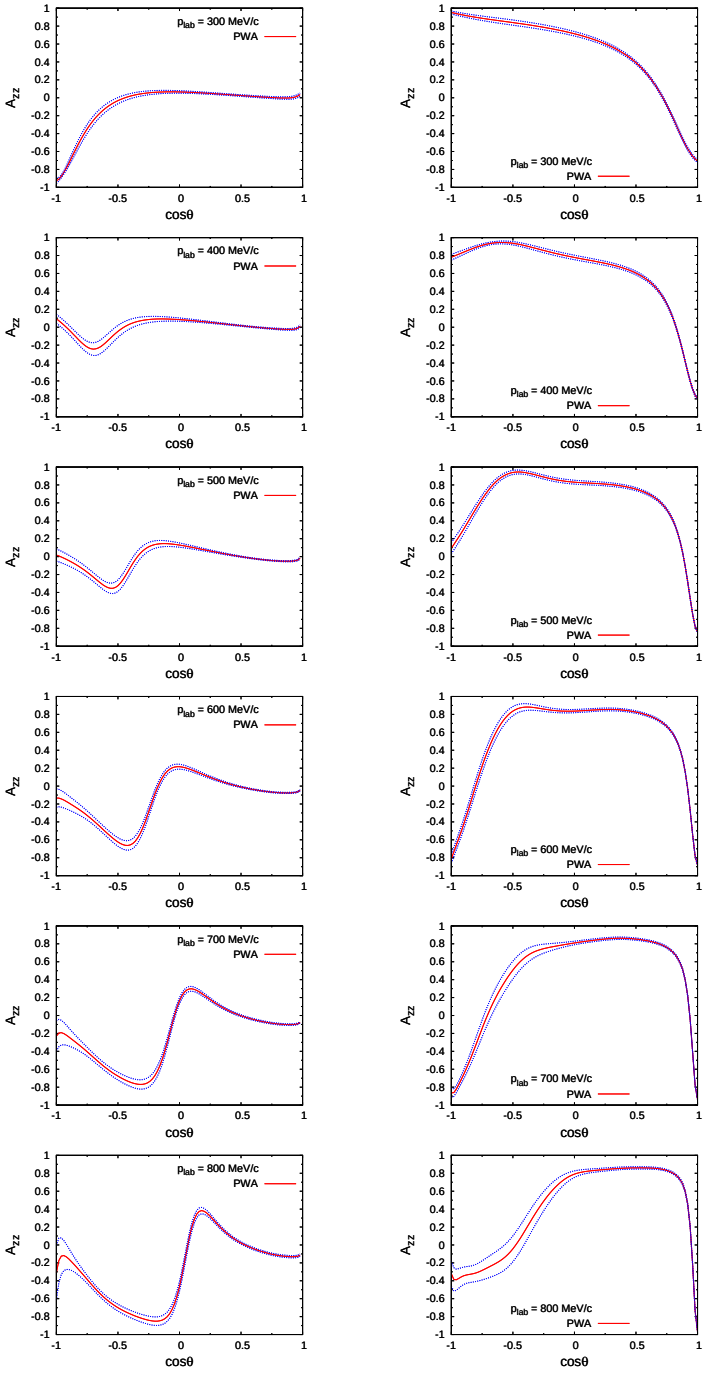

Figure 5.18: The spin correlation A_{zz} for $\bar{p}p$ elastic and charge-exchange scattering.

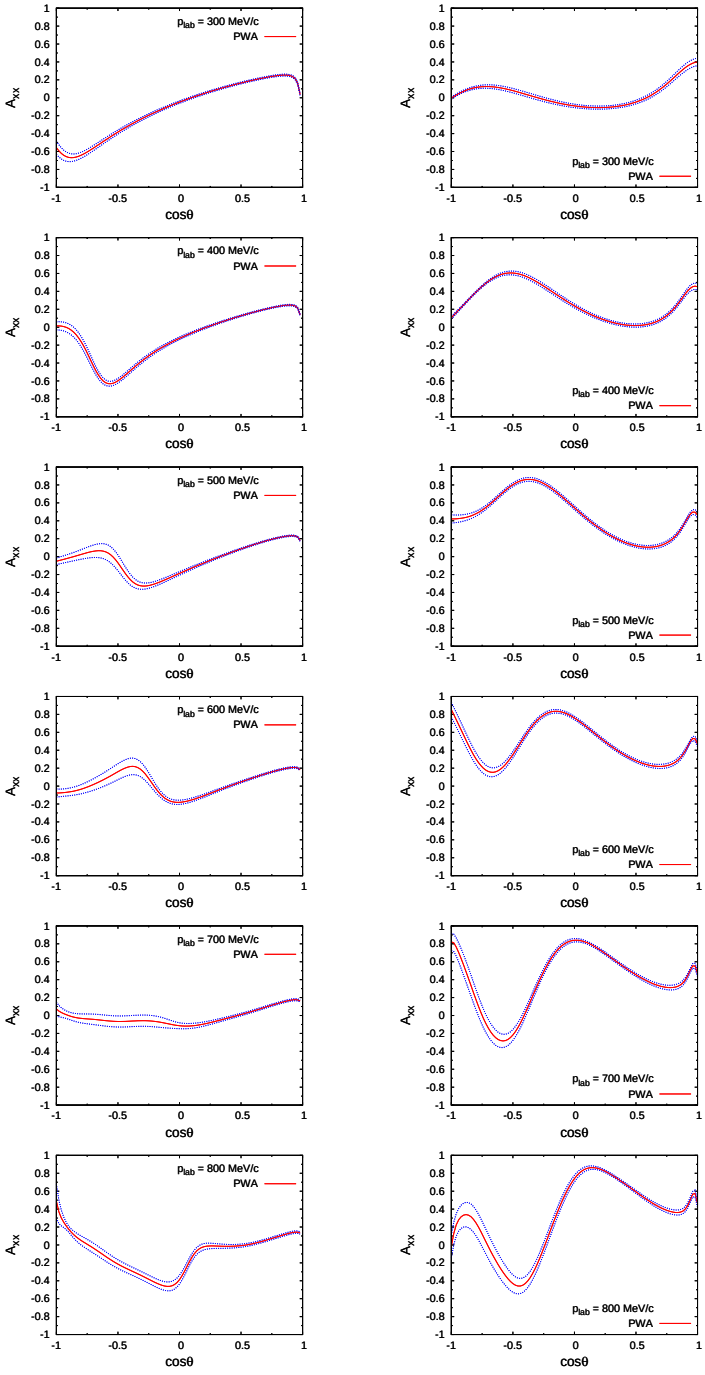

Figure 5.19: The spin correlation A_{xx} for $\bar{p}p$ elastic and charge-exchange scattering.

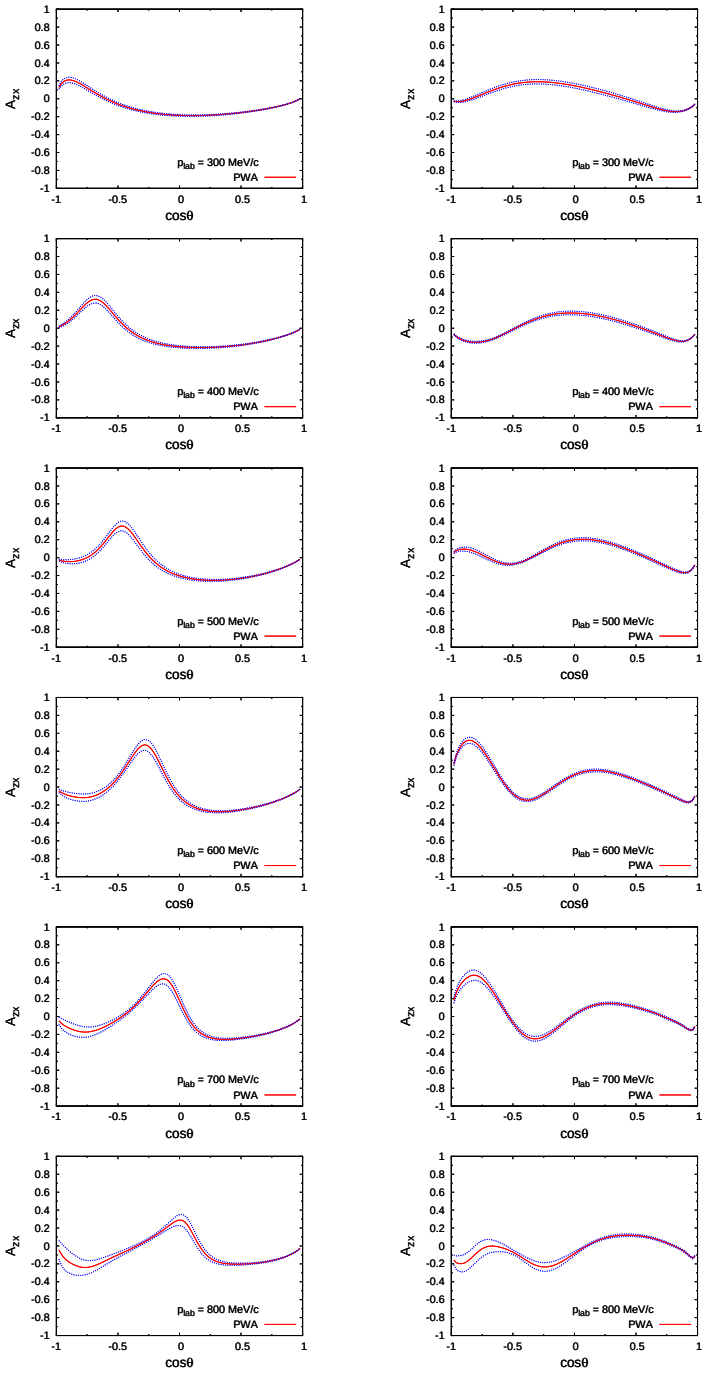

Figure 5.20: The spin correlation A_{zx} for $\bar{p}p$ elastic and charge-exchange scattering.

Summary

Motivated by renewed experimental interest in low-energy antiproton-proton scattering, we have presented a new energy-dependent partial-wave analysis of all antiproton-proton elastic ($\bar{p}p \to \bar{p}p$) and charge-exchange ($\bar{p}p \to \bar{n}n$) scattering data below 925 MeV/c antiproton laboratory momentum. The model independence and quality of the partial-wave analysis have been improved by using for the long-range interaction, next to the electromagnetic potential, the charge-conjugated one- and two-pion exchange potential derived from the effective chiral Lagrangian of quantum chromodynamics. The short-range interactions, including the coupling to the mesonic annihilation channels, are parametrized by a complex boundary condition at a radius of $r = 1.2$ fm. The database has been updated and includes now all high-quality differential cross sections and analyzing powers for charge-exchange scattering.

The final $\bar{p}p$ database contains $N_{\rm dat} = 3749$ scattering data, $N_{\rm obs} = 3636$ data points of scattering observables, $N_{\rm par} = 46$ model (P-matrix) parameters, $N_{\rm n} = 125$ normalization parameters (of which $N_{\rm ne} = 113$ have errors and $N_{\rm nf} = 12$ are "floated"). The number of degrees of freedom of the fit is $N_{\rm df} = 3578$.

The fit has resulted in a minimum χ^2 value of $\chi^2_{\rm min} = 3750.6$. (The total minimum χ^2 from the scattering observables is $\chi^2_{\rm obs} = 3672.0$, and the total minimum χ^2 from the normalizations is $\chi^2_{\rm norm} = 78.7$.) Therefore, the minimum χ^2 per datum is $\chi^2_{\rm min}/N_{\rm dat} = 1.000$, and the minimum χ^2 per degree of freedom is $\chi^2_{\rm min}/N_{\rm df} = 1.048$. When the model is perfect and the database is a perfect statistical ensemble, one expects $\langle \chi^2_{\rm min}/N_{\rm df} \rangle = 1.000 \pm 0.024$, hence our result for $\chi^2_{\rm min}/N_{\rm df}$ is only two standard deviations too high. The results of the partial-wave analysis agree well with the experimental data.

The S-matrix elements for the lowest partial waves have been presented for both the elastic and charge-exchange scattering at the laboratory momentum of the incoming antiproton $p_{\rm lab} = 100$, 200, 300, ..., 900, and 1000 MeV/c. The phase-

shift and inelastic parameters (together with the mixing parameters) for the lowest partial waves have been given as well for the same momenta assuming isospin symmetry. The Argrand diagrams have been shown for the lowest partial waves with the laboratory momentum running from 1 MeV/c to 1000 MeV/c assuming isospin symmetry. The quality of the fit implies in particular that the charge-conjugated chiral one-pion-exchange and two-pion-exchange potential provides an excellent long-range antiproton-proton interaction, which can be counted as a success for chiral effective field theory. The statistical quality of the final antiproton-proton database has been studied in more detail by investigating the distribution of the contributions of the individual data points to the total χ^2, and the result implies that the χ^2 distribution of the partial-wave analysis is close to what is expected for statistical data.

The polarization of an initially unpolarized antiproton beam which is scattered by a polarized proton target has been studied by using the chiral one- and two-pion potential together with the Coulomb potential and the filtering mechanism. The polarization results have been presented with acceptance angles $\theta_{\rm acc}^{\rm lab} = 5$, 10, 20, and 30 mrad in the laboratory frame, and for laboratory momentum of the incoming antiproton from 100 MeV/c to 1000 MeV/c. For the target with polarization perpendicular to the direction of the incoming beam (transversal, $P_B = P_\perp$), the maximal beam polarization is around -15%, which of course depends on the acceptance angle. At momenta around $p_{\rm lab} = 350$ MeV/c, the polarization can reach about -20% with acceptance angle $\theta_{\rm acc}^{\rm lab} = 30$ mrad. Even with acceptance angle $\theta_{\rm acc}^{\rm lab} = 5$ mrad, there is about -10% polarization at momenta around $p_{\rm lab} = 550$ MeV/c. When the momentum reaches $p_{\rm lab} = 1000$ MeV/c, the polarization is around 5%. For the target with polarization collinear with the direction of the incoming beam (longitudinal, $P_B = P_\parallel$), the maximal beam polarization is around -2% at low energies and 5% at relative high energies. For low energies, at momenta around $p_{\rm lab} = 300$ MeV/c, the polarization can reach about -3% with acceptance angle $\theta_{\rm acc}^{\rm lab} = 30$ mrad; at momenta around $p_{\rm lab} = 350$ MeV/c, the polarization can reach about -1% with acceptance angle $\theta_{\rm acc}^{\rm lab} = 5$ mrad. For high energies, when the momentum is about $p_{\rm lab} = 1000$ MeV/c, the polarizations are between 5% and 6% when the acceptance angle goes from $\theta_{\rm acc}^{\rm lab} = 5$ to 30 mrad. Roughly speaking, the transversal polarization $P_\perp$ can reach higher values than the longitudinal polarization $P_\parallel$, at least in the energy range considered here. For the transverse case, the maximal polarization reaches between -20% and 5%, while for the longitudinal case, the maximal polarization is between -3% and 6%. A noticeable polarization can be reached in a reasonable time for both $P_\perp$ and

$P_\parallel$ in the energy range considered here. The cross-section differences between the antiparallel- and parallel-spin case in the transverse and longitudinal situation with respect to the total charge-exchange cross section are shown for the charge-exchange scattering.

Some predictions for the spin observables up to rank-two have been given as well at the laboratory momenta $p_{\rm lab}$ = 300, 400, 500, 600, 700, and 800 MeV/c for both the elastic and charge-exchange scattering, and which can be tested by future experimental data. These observables include analyzing power A_y (or polarization P); depolarization D_{yy} (or depolarization D); spin transfer K_{yy} (or polarization-transfer parameter D_t); transverse-rotation parameters R and R'; longitudinal-rotation parameters A and A'; polarization-transfer parameters R_t, R'_t, A_t, and A'_t; spin-correlation parameters C_{nn}, C_{kp}, C_{pp}, C_{kk}, and A_{yy}, A_{zz}, A_{xx}, and A_{zx}. In the charge-exchange case, the values of the polarization-transfer parameters R'_t and A_t are large for the very forward angles at low energies. This characteristic may be exploited to produce polarized antineutron beams.

Further improvement of the partial-wave analysis is certainly possible, but it will require additional high-quality experimental data. Below 400 MeV/c, there are hardly scattering data available. Spin observables can further constrain the solution of the partial-wave analysis, provided they are precise enough. A better understanding of the annihilation process for $\bar{p}p$ scattering can also help. Finally, it will also be interesting to study how to generalize and adapt the method used here to higher energies.

Samenvatting

Met hernieuwde experimentele interesse in laag-energetische antiprotonproton-verstrooiing als motivatie, hebben wij een nieuwe energie-afhankelijke partiëlegolfanalyse ontwikkeld. Dit is een analyse van alle antiproton-proton elastische- ($\bar{p}p \to \bar{p}p$) en ladingsuitwisselings- ($\bar{p}p \to \bar{n}n$) verstrooiingsdata met een antiproton laboratoriummomentum lager dan 925 MeV/c. De modelonafhankelijkheid en kwaliteit van de partiëlegolfanalyse is verbeterd door voor de lange-afstandsinteractie, naast de electromagnetische potentiaal, ook de ladingsgeconjugeerde één- en twee-pionuitwisselingspotentiaal te gebruiken, die is afgeleid van de effectieve chirale Lagrangiaan van quantumchromodynamica. De korte-afstandsinteracties, inclusief de koppeling met de mesonische annihilatiekanalen, zijn geparametriseerd door een complexe randvoorwaarde bij een straal van $r = 1.2$ fm. De database bevat nu alle differentiële werkzame doorsnedes van hoge kwaliteit en polarizaties voor ladingsuitwisselingsverstrooiing.

De uiteindelijke $\bar{p}p$ database bevat $N_{\rm dat} = 3749$ verstrooiingsdata, $N_{\rm obs} = 3636$ datapunten van verstrooiingsobservabelen, $N_{\rm par} = 46$ modelparameters (P matrix), $N_{\rm n} = 125$ normalizatieparameters (waarvan $N_{\rm ne} = 113$ fouten hebben en $N_{\rm nf} = 12$ niet). Het aantal vrijheidsgraden van de fit is $N_{\rm df} = 3578$.

De fit resulteerde in een minimale χ^2 waarde van $\chi^2_{\rm min} = 3750.6$. (De totale minimale χ^2 van de verstrooiingsobservabelen is $\chi^2_{\rm obs} = 3672.0$, en de totale minimale χ^2 van de normalizaties is $\chi^2_{\rm norm} = 78.7$.) Dus de minimale χ^2 per datum is $\chi^2_{\rm min}/N_{\rm dat} = 1.000$ en de minimale χ^2 per vrijheidsgraad is $\chi^2_{\rm min}/N_{\rm df} = 1.048$. Als het model perfect is en de database een perfect statistisch ensemble is, verwacht men $\langle \chi^2_{\rm min}/N_{\rm df} \rangle = 1.000 \pm 0.024$, dus ons resultaat voor $\chi^2_{\rm min}/N_{\rm df}$ is slechts twee standaarddeviaties te hoog. De resultaten van de partiëlegolfanalyse komen goed overeen met de experimentele data.

De S-matrixelementen voor de laagste partiële golven zijn getoond voor zowel elastische- en ladingsuitwisselings-verstrooiing bij een laboratoriummomentum van

het inkomende antiproton van $p_{\rm lab} = 100$, 200, 300, ..., 900 en 1000 MeV/c. De faseverschuiving en inelastische parameters (alsmede de mengparameters) voor de laagste partiële golven zijn ook gegeven voor dezelfde momenta en met isospinsymmetrie als aanname. De Argranddiagrammen zijn getoond voor de laagste partiële golven met het laboratoriummomentum lopend van 1 MeV/c tot 1000 MeV/c en isospinsymmetrie als aanname. De kwaliteit van de fit impliceert in het bijzonder dat de ladingsgeconjugeerde chirale één- en twee-pionuitwisselingspotentiaal een uitstekende lange-afstands-antiprotonprotoninteractie verschaft, hetgeen als een success voor chirale effectieve veldentheorie beschouwd kan worden. De statistische kwaliteit van de uiteindelijke antiproton-proton database is in detail bestudeerd door de verdeling van de bijdragen van de individuele datapunten aan de totale χ^2 te onderzoeken. Het resultaat impliceert dat de χ^2 distributie van de partiëlegolfanalyse dichtbij de verwachting voor statistische data ligt.

De polarizatie van een antiprotonbundel die aanvankelijk ongepolarizeerd is en verstrooid wordt door een gepolarizeerd protondoel is bestudeerd door een chirale één- en twee-pionpotentiaal te gebruiken, samen met de Coulombpotentiaal en het filtermechanisme. De polarizatieresultaten zijn getoond met acceptantiehoeken $\theta_{\rm acc}^{\rm lab} = 5$, 10, 20 en 30 mrad in het laboratoriumframe, en voor het laboratoriummomentum van de inkomende antiproton tussen 100 MeV/c en 1000 MeV/c. De maximale bundelpolarizatie voor het doel met de polarizatie loodrecht op de richting van de inkomende bundel (transversaal, $P_B = P_\perp$) is rond -15%, hetgeen natuurlijk van de acceptantiehoek afhangt. Bij momenta rond $p_{\rm lab} = 350$ MeV/c, kan de polarizatie ongeveer -20% bereiken bij een acceptentiehoek van $\theta_{\rm acc}^{\rm lab} = 30$ mrad. Zelfs bij een acceptantiehoek van $\theta_{\rm acc}^{\rm lab} = 5$ mrad is er ongeveer -10% polarizatie bij momenta rond $p_{\rm lab} = 550$ MeV/c. Als het momentum $p_{\rm lab} = 1000$ MeV/c bereikt, is de polarizatie rond 5%. In het geval dat de polarizatie van het doel en de richting van de inkomende bundel collineair zijn (longitudinaal, $P_B = P_\parallel$), is de maximale bundelpolarizatie rond -2% bij lage energieën en 5% bij relatief hoge energieën. Bij lage energieën en momenta rond $p_{\rm lab} = 300$ MeV/c kan de polarizatie ongeveer -3% bereiken met een acceptantiehoek van $\theta_{\rm acc}^{\rm lab} = 30$ mrad, bij momenta rond $p_{\rm lab} = 350$ MeV/c kan de polarizatie ongeveer -1% bereiken, met een acceptatiehoek van $\theta_{\rm acc}^{\rm lab} = 5$ mrad. Voor hoge energieën, als het momentum ongeveer $p_{\rm lab} = 1000$ MeV/c is, zijn de polarizaties tussen 5% en 6% als de acceptantiehoek gaat van $\theta_{\rm acc}^{\rm lab} = 5$ tot 30 mrad. Grofweg kan men zeggen dat transversale polarizatie $P_\perp$ hogere waardes kan bereiken dan de longitudinale polarizatie $P_\parallel$, op zijn minst in het energiebereik dat hier bekeken is. Voor het transversale geval kan de maximale polarizatie tussen -20% en 5% bereiken, terwijl voor het longitudinale

geval de maximale polarizatie tussen -3% en 6% ligt. In het energiebereik dat hier bekeken werd kan een waarneembare polarizatie voor zowel $P_\perp$ en $P_\parallel$ bereikt worden in een redelijke tijd. De cross-sectieverschillen tussen de antiparallelle en parallelle spin gevallen in de transverale en longitudinale situatie ten opzichte van de totale ladingsuitwisselingscross-sectie, werden getoond voor ladingsuitwisselingsverstrooiing.

Er werden ook een aantal voorspellingen gedaan voor de spinobservabelen tot aan rang twee voor laboratoriummomenta van $p_{\rm lab} = 300$, 400, 500, 600, 700 en 800 MeV/c voor zowel elastische- als ladingsuitwisselings-verstrooiing. Deze kunnen getest worden met toekomstige experimentele data. Deze observabelen omvatten polarizatie A_y (of polarizatie P); depolarizatie D_{yy} (of depolarizatie D); spinoverdracht K_{yy} (of polarizatieoverdrachtsparameter D_t); transverale rotatieparameters R and R'; longitudinale rotatieparameters A and A'; polarizatieoverdrachtsparameters R_t, R'_t, A_t en A'_t; spin-correlatieparameters C_{nn}, C_{kp}, C_{pp}, C_{kk} en A_{yy}, A_{zz}, A_{xx} en A_{zx}. De waardes van de polarizatieoverdrachtsparameters R'_t en A_t zijn groot in het geval van ladingsuitwisseling met voorwaartse hoeken en bij lage energieën. Dit kenmerk zou gebruikt kunnen worden om gepolarizeerde antineutronenbundels te maken.

Verdere verbetering van de partiëlegolfanalyse is zeker mogelijk, maar daarvoor zijn extra experimentele data van hoge kwaliteit nodig. Onder 400 MeV/c zijn er nauwelijks verstrooiingsdata beschikbaar. Mits zij precies genoeg zijn, kunnen spinobservabelen de oplossing van de partiëlegolfanalyse nog meer vastleggen. Een beter begrip van de annihilatieprocessen voor $\bar{p}p$ verstrooiing kan ook helpen. Tenslotte is het ook interessant om te bestuderen hoe de methodes die hier gebruikt zijn aangepast en gegeneraliseerd kunnen worden voor hogere energieën.

Acknowledgments

It is impossible for me to finish this thesis without the help and encouragement, directly or indirectly, of many people. Now, it is a good opportunity for me to express my deep acknowledgments to these people.

First, I would like to thank my promotor Rob Timmermans for providing this project and other projects for me to study, for the nice ideas shared with me, for the nice discussions, and for the guidance throughout these years. Rob, you helped me a lot during the last years. I appreciate that very much. You are a very good teacher. I followed some of your lectures and they were very nice and I really enjoyed them. Of course, I thank you also for translating the title of this thesis into Dutch for me.

Many thanks to Olaf Scholten, Daniël Boer, Bira van Kolck, Lex Dieperink, and Renato Higa. I thank you all for the nice discussions about physics. You are always ready to help and I am really grateful for that.

Besides the discussions with the theorists, I also enjoyed the discussions about physics with other physicists. I am grateful for the nice discussions with Johan Messchendorp, Nasser Kalantar-Nayestanaki, Muhsin Harakeh, Herbert Löhner, Catherine Rigollet, and Gerco Onderwater. Johan, thank you also for providing me the experimental data of the photoproduction of eta and eta-prime.

Many thanks to the members of the theory meeting for the interesting talks and discussions. Many thanks also to the members of the FAIR subatomic meeting for the interesting talks, discussions, and of course for the nice cakes, cookies, and annual dinners as well. I learned something from your nice talks and from the discussions in the meetings.

I would like thank Jacob Noordmans for referring me to JaxoDraw which is a nice software for drawing Feynman diagrams; thank Fengping Jin for referring me to Gnuplot which is a nice tool to plot figures; thank Wilbert Kruithof for referring

me to JabRef which is a wonderful reference manager. All of these softwares are very helpful and saved me a lot of time. Fengping, thank you also for helping with the figures. Wilbert, thank you also for helping with the tables. Jacob, thank you also for translating the summaries of my thesis from English into Dutch and you did a really good job.

I am deeply grateful to Daniël Boer, Klaus Jungmann, and Mees de Roo for agreeing to be the members of my reading committee, for spending time on reading the manuscript of my thesis, and for many nice and valuable comments.

Keri and Jacob, thank you for being my paranymphs.

Ali, Amita, Auke, Ayan, Bijaya, Bodha, Duurt, Elmaddin, Ganesh, Gouri, Hong, Hossein, Jacob, Jordy, Kalpana, Keri, Krijn, Laura, Lotje, Manisha, Mayerlin, Olena, Olga and Sergey, Oscar, Praveen, Qader, Renato, Ruud, Sadia, Soumya, Sreekanth, Takashi, Vanni, and Wouter, thank you all for the nice time together, either for tennis, dinner, movie, ice skating, table tennis, concert, wadloop, party, or something else.

Kalpana, Soumya, Joanne, Josbert, Wilbert, and Duurt, thank you for being nice officemates and for the good working circumstance.

I would like to thank Hilde van der Meer. You are always very friendly and helpful. You helped me a lot with many things, for example the issues related to visa application, residence permit application, insurance, student card, etc, etc. I am really grateful for this.

Many thanks to Marjan Koopmans and Amarins Petitaux for taking care of things for me related to the FANTOM school, conferences, and paper work.

Many thanks also to Annet van der Woude, Simone de Meijer, Miranda Ruiter, Carla Hemmes, Robert Springer, Martine ter Wal, Eveline van der Werf, Harry Elenius, and Alfred Felzel for taking care of things for me. Harry, thank you also for binding the manuscripts of my thesis which I sent to the reading committee.

I would like to thank the people from the IT group, especially Ralf Pelster for the help when I had problems with my computer.

Many thanks to Anneke Toxopeus and Marco van der Vinne from the office of the International Service Desk. You were always helpful when I had some questions regarding to tax, visa, residence permit application, and some other things.

Byeong-Ui and Su-Jung, Jan and Greta, Anke, Esther, Trix, Giulia, Krina, Sezar, Arend, Katja, Hanna, Anne Kristin, Rieza, Fedir, Martijn, Paul, and all the other people from HOST, many thanks to all of you for the wonderful time together, for

the great evenings and weekends, for the dinners, for the sports, games, movies, and many other things. I really enjoyed the time together with you and learned a lot from you. I am sorry that I cannot put all of your names here, but I always feel warm in my heart when I think about you. It is a great pleasure to know you.

Shengjun and Zhao Shuang, Fengping and Enda, Wu Yu and Liu Ji, Gao Jia and Guo Zhe, Weiran, Jingyan, Chunling, and Xiaoming, thank you all for the wonderful time together in Groningen, either for the talks, sports, or games, and of course the dinners. I always felt like in China when I was with you. I always remember that in winter time when I came into your places from the cold outside, the wonderful and warm dinners (most of you are really good at cooking Chinese food) were ready and big smiles on your faces, at those moments I always felt that I was back home. I enjoyed a lot the time together with you.

I would like to thank my friends in China for the support. I am sure that you know who you are, though your names are not mentioned here. Every time, when I came back to China, I always got a warm and wonderful welcome from some of you. I am so lucky to have you as my friends.

Finally, I thank my family for supporting me all the time. My deepest thanks to my lovely grandparents and parents. Thank you for your great love and for everything that you have done for me. You are always the source of my spirit strength.

Bibliography

[1] The PANDA Collaboration, arXiv:0903.3905v1 [hep-ex] (2009).

[2] The FNAL-E581/704 Collaboration, Nucl. Instrum. Meth. A **290**, 269 (1990).

[3] The E581/704 Collaboration, Phys. Rev. D **55**, 1159 (1997).

[4] The PAX Collaboration, arXiv:hep-ex/0505054v1 (2005).

[5] The PAX Collaboration, arXiv:0904.2325v1 [nucl-ex] (2009).

[6] W. N. Cottingham and R. Vinh Mau, Phys. Rev. **130**, 735 (1963).

[7] W. N. Cottingham, M. Lacombe, B. Loiseau, J. M. Richard, and R. Vinh Mau, Phys. Rev. D **8**, 800 (1973).

[8] M. Lacombe, B. Loiseau, J.-M. Richard, R. Vinh Mau, P. Pires, and R. de Tourreil, Phys. Rev. D **12**, 1495 (1975).

[9] M. Lacombe, B. Loiseau, J. M. Richard, R. Vinh Mau, J. Côté, P. Pirès, and R. de Tourreil, Phys. Rev. C **21**, 861 (1980).

[10] M. M. Nagels, T. A. Rijken, and J. J. de Swart, Phys. Rev. D **17**, 768 (1978).

[11] R. Machleidt, K. Holinde, and C. Elster, Phys. Rept. **149**, 1 (1987).

[12] D. Schütte, Nucl. Phys. **221**, 450 (1974).

[13] K. Kotthoff, K. Holinde, R. Machleidt, and D. Schütte, Nucl. Phys. A **242**, 429 (1975).

[14] K. Kotthoff, R. Machleidt, and D. Schütte, Nucl. Phys. **264**, 484 (1976).

[15] J. S. Ball and G. F. Chew, Phys. Rev. **109**, 1385 (1958); J. S. Ball and J. R. Fulco, *ibid.* **113**, 647 (1959).

[16] M. S. Spergel, Il Nuovo Cimento A **47**, 410 (1967).

[17] O. D. Dalkarov and F. Myhrer, Il Nuovo Cimento A **40**, 152 (1977).

[18] R. J. N. Phillips, Rev. Mod. Phys. **39**, 681 (1967).

[19] R. A. Bryan and R. J. N. Phillips, Nucl. Phys. B **5**, 201 (1968); **7**, 481(E) (1968).

[20] F. Myhrer and A. Gersten, Il Nuovo Cimento A **37**, 21 (1977).

[21] C. B. Dover and J. M. Richard, Phys. Rev. C **21**, 1466 (1980).

[22] C. B. Dover and J. M. Richard, Phys. Rev. C **25**, 1952 (1982).

[23] M. Kohno and W. Weise, Nucl. Phys. A **454**, 429 (1986).

[24] T. Hippchen, K. Holinde, and W. Plessas, Phys. Rev. C **39**, 761 (1989).

[25] T. Hippchen, J. Haidenbauer, K. Holinde, and V. Mull, Phys. Rev. C **44**, 1323 (1991).

[26] V. Mull and K. Holinde, Phys. Rev. C **51**, 2360 (1995).

[27] J. Côté, M. Lacombe, B. Loiseau, B. Moussallam, and R. Vinh Mau, Phys. Rev. Lett. **48**, 1319 (1982).

[28] M. Lacombe, B. Loiseau, B. Moussallam, and R. Vinh Mau, Phys. Rev. C **29**, 1800 (1984).

[29] M. Pignone, M. Lacombe, B. Loiseau, and R. Vinh Mau, Phys. Rev. Lett. **67**, 2423 (1991).

[30] M. Pignone, M. Lacombe, B. Loiseau, and R. Vinh Mau, Phys. Rev. C **50**, 2710 (1994).

[31] B. El-Bennich, M. Lacombe, B. Loiseau, and R. Vinh Mau, Phys. Rev. C **59**, 2313 (1999).

[32] B. El-Bennich, M. Lacombe, B. Loiseau, and S. Wycech, Phys. Rev. C **79**, 054001 (2009).

[33] P. H. Timmers, W. A. van der Sanden, and J. J. de Swart, Phys. Rev. D **29**, 1928 (1984).

[34] P. H. Timmers, W. A. van der Sanden, and J. J. de Swart, Phys. Rev. D **31**, 99 (1985).

[35] G. Q. Liu and F. Tabakin, Phys. Rev. C **41**, 665 (1990).

[36] V. Mull, J. Haidenbauer, T. Hippchen, and K. Holinde, Phys. Rev. C **44**, 1337 (1991).

[37] J. Haidenbauer, K. Holinde, and A. W. Thomas, Phys. Rev. C **45**, 952 (1992).

[38] A. Pais and R. Jost, Phys. Rev. **87**, 871 (1952).

[39] T. D. Lee and C. N. Yang, Il Nuovo Cimento **3**, 749 (1956).

[40] C. Goebel, Phys. Rev. **103**, 258 (1956).

[41] M. M. Nagels, T. A. Rijken, and J. J. de Swart, Phys. Rev. D **12**, 744 (1975).

[42] R. G. E. Timmermans, Th. A. Rijken, and J. J. de Swart, Phys. Rev. Lett. **67**, 1074 (1991).

[43] R. Timmermans, Th. A. Rijken, and J. J. de Swart, Phys. Rev. C **50**, 48 (1994).

[44] R. Timmermans, Th. A. Rijken, and J. J. de Swart, Phys. Rev. C **52**, 1145 (1995).

[45] J. R. Bergervoet, P. C. van Campen, W. A. van der Sanden, and J. J. de Swart, Phys. Rev. C **38**, 15 (1988).

[46] J. R. Bergervoet, P. C. van Campen, R. A. M. Klomp, J.-L. de Kok, T. A. Rijken, V. G. J. Stoks, and J. J. de Swart, Phys. Rev. C **41**, 1435 (1990).

[47] V. G. J. Stoks, R. A. M. Klomp, M. C. M. Rentmeester, and J. J. de Swart, Phys. Rev. C **48**, 792 (1993).

[48] M. C. M. Rentmeester, R. G. E. Timmermans, J. L. Friar, and J. J. de Swart, Phys. Rev. Lett. **82**, 4992 (1999).

[49] M. C. M. Rentmeester, R. G. E. Timmermans, and J. J. de Swart, Phys. Rev. C **67**, 044001 (2003).

[50] D. Zhou and R. G. E. Timmermans, Phys. Rev. C **86**, 044003 (2012).

[51] D. Zhou and R. G. E. Timmermans, submitted for publication.

[52] S. Weinberg, Phys. Rev. **166**, 1568 (1968).

[53] S. Weinberg, Physica A **96**, 327 (1979).

[54] S. Coleman, J. Wess, and B. Zumino, Phys. Rev. **177**, 2239 (1969).

[55] C. Callan, S. Coleman, J. Wess, and B. Zumino, Phys. Rev. **177**, 2247 (1969).

[56] S. Weinberg, Phys. Lett. B **251**, 288 (1990).

[57] S. Weinberg, Nucl. Phys. B **363**, 3 (1991).

[58] C. Ordóñez and U. van Kolck, Phys. Lett. B **291**, 459 (1992).

[59] C. Ordóñez, L. Ray, and U. van Kolck, Phys. Rev. Lett. **72**, 1982 (1994).

[60] C. Ordóñez, L. Ray, and U. van Kolck, Phys. Rev. C **53**, 2086 (1996).

[61] N. Kaiser, R. Brockmann, and W. Weise, Nucl. Phys. A **625**, 758 (1997).

[62] V. G. J. Stoks, R. A. M. Klomp, C. P. F. Terheggen, and J. J. de Swart, Phys. Rev. C **49**, 2950 (1994).

[63] V. F. Dmitriev, A. I. Milstein, and V. M. Strakhovenko, Nucl. Instrum. Meth. B **266**, 1122 (2008).

[64] V. F. Dmitriev, A. I. Milstein, and S. G. Salnikov, Phys. Lett. B **690**, 427 (2010).

[65] P. L. Csonka, Nucl. Instrum. Meth. **63**, 247 (1968).

[66] A. I. Milstein and V. M. Strakhovenko, Phys. Rev. E **72**, 066503 (2005).

[67] D. Oellers, L. Barion, S. Barsov, U. Bechstedt, P. Benati, S. Bertelli, D. Chiladze, G. Ciullo, M. Contalbrigo, P. F. Dalpiaz, J. Dietrich, N. Dolfus, S. Dymov, R. Engels, W. Erven, A. Garishvili, R. Gebel, P. Goslawski, K. Grigoryev, H. Hadamek, A. Kacharava, A. Khoukaz, A. Kulikov, G. Langenberg, A. Lehrach, P. Lenisa, N. Lomidze, B. Lorentz, G. Macharashvili, R. Maier, S. Martin, S. Merzliakov, I. N. Meshkov, H. O. Meyer, M. Mielke, M. Mikirtychiants, S. Mikirtychiants, A. Nass, M. Nekipelov, N. N. Nikolaev, M. Nioradze, G. d'Orsaneo, M. Papenbrock, D. Prasuhn, F. Rathmann, J. Sarkadi, R. Schleichert, A. Smirnov, H. Seyfarth, J. Sowinski, D. Spoelgen, G. Stancari, M. Stancari, M. Statera, E. Steffens, H. J. Stein, H. Stockhorst, H. Straatmann, H. Ströher,

M. Tabidze, G. Tagliente, P. Thörngren Engblom, S. Trusov, A. Vasilyev, Chr. Weidemann, D. Welsch, P. Wieder, P. Wüstner, and P. Zupranski, Phys. Lett. B **674**, 269 (2009).

[68] F. Rathmann, C. Montag, D. Fick, J. Tonhäuser, W. Brückner, H.-G. Gaul, M. Grieser, B. Povh, M. Rall, E. Stevens, F. Stock, K. Zapfe, B. Braun, G. Graw, and W. Haeberli, Phys. Rev. Lett. **71**, 1379 (1993).

[69] B. A. Lippmann and J. Schwinger, Phys. Rev. **79**, 469 (1950).

[70] J. J. de Swart, J. R. M. Bergervoet, P. C. M. van Campen, and W. A. M. van der Sanden, THEF-NYM-85.04 (1985).

[71] V. G. J. Stoks and J. J. de Swart, Phys. Rev. C **42**, 1235 (1990).

[72] G. Breit, Phys. Rev. **99**, 1581 (1955).

[73] L. D. Knutson and D. Chiang, Phys. Rev. C **18**, 1958 (1978).

[74] A. Kievsky, M. Viviani, and L. E. Marcucci, Phys. Rev. C **69**, 014002 (2004).

[75] N. Hoshizaki, Prog. Theor. Phys. Suppl. **42**, 107 (1968).

[76] P. LaFrance, F. Lehar, B. Loiseau, and P. Winternitz, Helv. Phys. Acta **65**, 611 (1992).

[77] H. Feshbach and E. L. Lomon, Ann. Phys. **29**, 19 (1964).

[78] R. L. Jaffe and F. E. Low, Phys. Rev. D **19**, 2105 (1979); R. L. Jaffe, in *Asymptotic Realms of Physics*, edited by A. H. Guth, K. Huang, and R. L. Jaffe (MIT Press, Cambridge, MA, 1983), p. 100.

[79] Y. A. Simonov, Phys. Lett. B **107**, 1 (1981).

[80] P. J. Mulders, Phys. Rev. D **28**, 443 (1983).

[81] B. L. G. Bakker and P. J. Mulders, Adv. Nucl. Phys. **17**, 1 (1986).

[82] G. J. M. Austen and J. J. de Swart, Phys. Rev. Lett. **50**, 2039 (1983).

[83] S. Weinberg, Phys. Rev. Lett. **17**, 616 (1966).

[84] Y. Tomozawa, Il Nuovo Cimento A **46**, 707 (1966).

[85] S. Weinberg, Phys. Rev. Lett. **65**, 1177 (1990).

[86] V. Stoks, R. Timmermans, and J. J. de Swart, Phys. Rev. C **47**, 512 (1993).

[87] J. J. de Swart, M. C. M. Rentmeester, and R. G. E. Timmermans, Pion-Nucleon Newsletter **13**, 96 (1997).

[88] M. L. Goldberger and S. B. Treiman, Phys. Rev. **110**, 1478 (1958).

[89] R. G. E. Timmermans, T. A. Rijken, and J. J. de Swart, Nucl. Phys. A **479**, 383c (1988).

[90] J. J. de Swart, T. A. Rijken, P. M. Maessen, and R. Timmermans, Il Nuovo Cimento A **102**, 203 (1989).

[91] R. G. E. Timmermans, Th. A. Rijken, and J. J. de Swart, Phys. Lett. B **257**, 227 (1991).

[92] R. G. E. Timmermans, Th. A. Rijken, and J. J. de Swart, Phys. Rev. D **45**, 2288 (1992).

[93] R. P. Hamilton, T. P. Pun, R. D. Tripp, H. Nicholson, and D. M. Lazarus, Phys. Rev. Lett. **44**, 1179 (1980).

[94] W. Brückner, B. Cujec, H. Döbbeling, K. Dworschak, F. Güttner, H. Kneis, S. Majewski, M. Nomachi, S. Paul, B. Povh, R. D. Ransome, T.-A. Shibata, M. Treichel, and Th. Walcher, Zeit. Phys. A **335**, 217 (1990).

[95] W. Brückner, H. Döbbeling, F. Güttner, D. von Harrach, H. Kneis, S. Majewski, M. Nomachi, S. Paul, B. Povh, R. D. Ransome, T.-A. Shibata, M. Treichel, and Th. Walcher, Phys. Lett. B **166**, 113 (1986).

[96] W. Brückner, B. Cujec, H. Döbbeling, K. Dworschak, H. Kneis, S. Majewski, M. Nomachi, S. Paul, B. Povh, R. D. Ransome, T.-A. Shibata, M. Treichel, and Th. Walcher, Zeit. Phys. A **339**, 367 (1991).

[97] W. Brückner, H. Döbbeling, F. Güttner, D. von Harrach, H. Kneis, S. Majewski, M. Nomachi, S. Paul, B. Povh, R. D. Ransome, T.-A. Shibata, M. Treichel, and Th. Walcher, Phys. Lett. B **169**, 302 (1986).

[98] D. Spencer and D. N. Edwards, Nucl. Phys. B **19**, 501 (1970).

[99] W. Brückner, B. Cujec, H. Döbbeling, K. Dworschak, F. Güttner, H. Kneis, S. Majewski, M. Nomachi, S. Paul, B. Povh, R. D. Ransome, T.-A. Shibata, M. Treichel, and Th. Walcher, Phys. Lett. B **197**, 463 (1987); **199**, 596(E) (1987).

[100] D. V. Bugg, J. Hall, A. S. Clough, R. L. Shypit, K. Bos, J. C. Kluyver, R. A. Kunne, L. Linssen, R. Birsa, F. Bradamante, S. Dalla Torre-Colautti, A. Martin, A. Penzo, P. Schiavon, A. Villari, E. Heer, C. LeLuc, Y. Onel, and D. Rapin, Phys. Lett. B **194**, 563 (1987).

[101] L. Linssen, C. I. Beard, R. Birsa, K. Bos, F. Bradamante, D. V. Bugg, A. S. Clough, S. Dalla Torre-Colautti, M. Giorgi, J. R. Hall, J. C. Kluyver, R. A. Kunne, C. Lechanoine-LeLuc, A. Martin, Y. Onel, A. Penzo, D. Rapin, P. Schiavon, R. L. Shypit, and A. Villari, Nucl. Phys. A **469**, 726 (1987).

[102] M. Alston-Garnjost, R. Kenney, D. Pollard, R. Ross, R. Tripp, and H. Nicholson, Phys. Rev. Lett. **35**, 1685 (1975).

[103] B. Conforto, G. Fidecaro, H. Steiner, R. Bizzarri, P. Guidoni, F. Marcelja, G. Brautti, E. Castelli, M. Ceschia, and M. Sessa, Il Nuovo Cimento A **54**, 441 (1968).

[104] M. Cresti, L. Peruzzo, and G. Sartori, Phys. Lett. B **132**, 209 (1983).

[105] R. P. Hamilton, T. P. Pun, R. D. Tripp, D. M. Lazarus, and H. Nicholson, Phys. Rev. Lett. **44**, 1182 (1980).

[106] V. Ashford, M. E. Sainio, M. Sakitt, and J. Skelly, Phys. Rev. Lett. **54**, 518 (1985).

[107] S. Sakamoto, T. Hashimoto, F. Sai, and S. S. Yamamoto, Nucl. Phys. B **195**, 1 (1982).

[108] A. S. Clough, C. I. Beard, D. V. Bugg, J. A. Edgington, J. Hall, K. Bos, J. C. Kluyver, R. A. Kunne, L. Linssen, R. Birsa, F. Bradamante, S. Dalla Torre-Colautti, M. Giorgi, A. Martin, A. Penzo, P. Schiavon, A. Villari, S. Degli-Agosti, E. Heer, R. Hess, C. Lechanoine-LeLuc, Y. Onel, and D. Rapin, Phys. Lett. B **146**, 299 (1984).

[109] T. Kageyama, T. Fujii, K. Nakamura, F. Sai, S. Sakamoto, S. Sato, T. Takahashi, T. Tanimori, S. S. Yamamoto, and Y. Takada, Phys. Rev. D **35**, 2655 (1987).

[110] K. Nakamura, T. Fujii, T. Kageyama, F. Sai, S. Sakamoto, S. Sato, T. Takahashi, T. Tanimori, and S. S. Yamamoto, Phys. Rev. Lett. **53**, 885 (1984).

[111] T. Kamae, H. Aihara, J. Chiba, H. Fujii, T. Fujii, H. Iwasaki, K. Nakamura, T. Sumiyoshi, Y. Takada, T. Takeda, M. Yamauchi, H. Fukuma, and T. Takeshita, Phys. Rev. Lett. **44**, 1439 (1980).

[112] K. Nakamura, H. Aihara, J. Chiba, H. Fujii, T. Fujii, H. Iwasaki, T. Kamae, T. Sumiyoshi, Y. Takada, T. Takeda, M. Yamauchi, H. Fukuma, and T. Takeshita, Phys. Rev. D **29**, 349 (1984).

[113] M. Alston-Garnjost, R. P. Hamilton, R. W. Kenney, D. L. Pollard, R. D. Tripp, H. Nicholson, and D. M. Lazarus, Phys. Rev. Lett. **43**, 1901 (1979).

[114] H. Iwasaki, H. Aihara, J. Chiba, H. Fujii, T. Fujii, T. Kamae, K. Nakamura, T. Sumiyoshi, Y. Takada, T. Takeda, M. Yamauchi, and H. Fukuma, Phys. Lett. B **103**, 247 (1981).

[115] R. Bizzarri, B. Conforto, G. C. Gialanella, P. Guidoni, F. Marcelja, E. Castelli, M. Ceschia, and M. Sessa, Il Nuovo Cimento A **54**, 456 (1968).

[116] F. Perrot-Kunne, R. Bertini, M. Costa, H. Catz, A. Chaumeaux, J.-C. Faivre, E. Vercellin, J. Arvieux, J. Yonnet, B. van den Brandt, D. R. Gill, J. A. Konter, S. Mango, G. D. Wait, E. Boschitz, W. Gyles, W. List, C. Otterman, R. Tacik, and M. Wessler, Phys. Lett. B **261**, 188 (1991).

[117] T. Tsuboyama, Y. Kubota, F. Sai, S. Sakamoto, and S. S. Yamamoto, Phys. Rev. D **28**, 2135 (1983).

[118] R. A. Kunne, C. I. Beard, R. Birsa, K. Bos, F. Bradamante, D. V. Bugg, A. S. Clough, S. Dalla Torre-Colautti, S. Degli-Agosti, J. A. Edgington, J. R. Hall, E. Heer, R. Hess, J. C. Kluyver, C. Lechanoine-LeLuc, L. Linssen, A. Martin, T. O. Niinikoski, Y. Onel, A. Penzo, D. Rapin, J. M. Rieubland, A. Rijllart, P. Schiavon, R. L. Shypit, F. Tessarotto, A. Villari, and P. Wells, Phys. Lett. B **206**, 557 (1988).

[119] R. A. Kunne, C. I. Beard, R. Birsa, K. Bos, F. Bradamante, D. V. Bugg, A. S. Clough, S. Dalla Torre-Colautti, J. A. Edgington, J. R. Hall, E. Heer, R. Hess, J. C. Kluyver, C. Lechanoine-LeLuc, L. Linssen, A. Martin, T. O. Niinikoski, Y. Onel, A. Penzo, D. Rapin, J. M. Rieubland, A. Rijllart, P. Schiavon, R. L. Shypit, F. Tessarotto, A. Villari, and P. Wells, Nucl. Phys. B **323**, 1 (1989).

[120] A. Ahmidouch, E. Heer, R. Hess, C. Lechanoine-Leluc, Ch. Mascarini, D. Rapin, R. Birsa, F. Bradamante, A. Bressan, S. Dalla Torre-Colautti, M. Giorgi, M. Lamanna, A. Martin, A. Penzo, P. Schiavon, F. Tessarotto, M. P. Macciotta, A. Masoni, G. Puddu, S. Serci, J. Arvieux, R. Bertini, R. A. Kunne, H. Catz, J. C. Faivre, F. Perrot-Kunne, M. Agnello, F. Iazzi, B. Minetti, T. Bressani, E. Chiavassa, N. De Marco, A. Musso, and A. Piccotti, Phys. Lett. B **364**, 116 (1995).

[121] R. Birsa, F. Bradamante, A. Bressan, S. Dalla Torre-Colautti, M. Giorgi, M. Lamanna, A. Martin, A. Penzo, P. Schiavon, F. Tessarotto, M. P. Macciotta, A. Masoni, G. Puddu, S. Serci, T. Niinikoski, A. Rijllart, A. Ahmidouch, E. Heer, R. Hess, C. Lechanoine-Le Luc, C. Mascarini, D. Rapin, J. Arvieux, R. Bertini, H. Catz, J. C. Faivre, R. A. Kunne, F. Perrot-Kunne, M. Agnello, F. Iazzi, B. Minetti, T. Bressani, E. Chiavassa, N. De Marco, A. Musso, and A. Piccotti, Phys. Lett. B **273**, 533 (1991).

[122] A. Ahmidouch, E. Heer, R. Hess, C. Lechanoine-Leluc, C. Mascarini, D. Rapin, R. Birsa, F. Bradamante, A. Bressan, S. Dalla Torre-Colautti, M. Giorgi, M. Lamanna, A. Martin, A. Penzo, P. Schiavon, F. Tessarotto, M. P. Macciotta, A. Masoni, G. Puddu, S. Serci, T. Niinikoski, A. Rijllart, H. Catz, J. C. Faivre, F. Perrot-Kunne, J. Arvieux, R. Bertini, R. A. Kunne, M. Agnello, F. Iazzi, B. Minetti, T. Bressani, E. Chiavassa, N. De Marco, A. Musso, and A. Piccotti, Nucl. Phys. B **444**, 27 (1995).

[123] P. Schiavon, R. Birsa, K. Bos, F. Bradamante, A. S. Clough, S. Dalla Torre-Colautti, J. R. Hall, E. Heer, R. Hess, J. C. Kluyver, R. A. Kunne, C. Lechanoine-LeLuc, L. Linssen, A. Martin, Y. Onel, A. Penzo, D. Rapin, R. L. Shypit, F. Tessarotto, and A. Villari, Nucl. Phys. A **505**, 595 (1989).

[124] R. Birsa, F. Bradamante, A. Bressan, S. Dalla Torre-Colautti, M. Giorgi, M. Lamanna, A. Martin, A. Penzo, P. Schiavon, F. Tessarotto, A. M. Zanetti, A. De Falco, M. P. Macciotta, A. Masoni, G. Puddu, S. Serci, A. Ahmidouch, E. Heer, R. Hess, C. Mascarini, D. Rapin, J. Arvieux, R. Bertini, J. C. Faivre, R. A. Kunne, and M. Agnello, Phys. Lett. B **339**, 325 (1994); **405**, 389(E) (1997).

[125] A. Bressan, R. Birsa, F. Bradamante, S. Dalla Torre-Colautti, M. Giorgi, M. Lamanna, A. Martin, P. Schiavon, F. Tessarotto, A. M. Zanetti, M. P. Macciotta, A. Masoni, G. Puddu, S. Serci, A. Ahmidouch, R. Heer,

R. Hess, C. Lechanoine-Leluc, D. Rapin, J. Arvieux, R. Bertini, J. C. Faivre, R. A. Kunne, and M. Agnello, Nucl. Phys. A **625**, 10 (1997).

[126] R. Birsa, F. Bradamante, S. Dalla Torre-Colautti, M. Giorgi, M. Lamanna, A. Martin, A. Penzo, P. Schiavon, F. Tessarotto, M. P. Macciotta, A. Masoni, G. Puddu, S. Serci, T. Niinikoski, A. Rijllart, A. Ahmidouch, E. Heer, R. Hess, R. A. Kunne, C. Lechanoine-Le Luc, C. Mascarini, D. Rapin, J. Arvieux, R. Bertini, H. Catz, J. C. Faivre, F. Perrot-Kunne, M. Agnello, F. Iazzi, B. Minetti, T. Bressani, E. Chiavassa, N. De Marco, A. Musso, and A. Piccotti, Phys. Lett. B **246**, 267 (1990).

[127] R. A. Kunne, C. I. Beard, R. Birsa, K. Bos, F. Bradamante, D. V. Bugg, A. S. Clough, S. Dalla Torre-Colautti, J. A. Edgington, M. Giorgi, J. R. Hall, E. Heer, R. Hess, J. C. Kluyver, C. Lechanoine-Leluc, L. Linssen, A. Martin, T. O. Niinikoski, Y. Onel, A. Penzo, D. Rapin, J. M. Rieubland, A. Rijllart, P. Schiavon, R. L. Shypit, F. Tessarotto, and A. Villari, Phys. Lett. B **261**, 191 (1991).

[128] T. Ohsugi, M. Fujisaki, S. Kaneko, Y. Murata, K. Okamura, H. Kohno, M. Fukawa, R. Hamatsu, T. Hirose, S. Kitamura, T. Mamiya, T. Yamagata, T. Emura, I. Kita, and K. Takahashi, Il Nuovo Cimento A **17**, 456 (1973).

[129] E. Eisenhandler, W. R. Gibson, C. Hojvat, P. I. P. Kalmus, L. C. Y. Lee, T. W. Pritchard, E. C. Usher, D. T. Williams, M. Harrison, W. H. Range, M. A. R. Kemp, A. D. Rush, J. N. Woulds, G. T. J. Arnison, A. Astbury, D. P. Jones, and A. S. L. Parsons, Nucl. Phys. B **113**, 1 (1976).

[130] H. Kohno, S. Kaneko, Y. Murata, T. Ohsugi, K. Okamura, M. Fukawa, R. Hamatsu, T. Hirose, T. Mamiya, T. Yamagata, T. Emura, I. Kita, and K. Takahashi, Nucl. Phys. B **41**, 485 (1972).

[131] R. Bertini, M. Costa, F. Perrot, H. Catz, A. Chaumeaux, J. Cl. Faivre, E. Vercellin, J. Arvieux, J. Yonnet, B. van den Brandt, J. A. Konter, D. R. Gill, S. Mango, G. D. Wait, E. Boschitz, W. Gyles, W. List, C. Otterman, R. Tacik, M. Wessler, E. Descroix, J. Y. Grossiord, and A. Guichard, Phys. Lett. B **228**, 531 (1989).

[132] M. Kimura, M. Takanaka, R. Hamatsu, Y. Hattori, T. Hirose, S. Kitamura, T. Yamagata, T. Emura, I. Kita, K. Takahashi, H. Kohno, and S. Matsumoto, Il Nuovo Cimento A **71**, 438 (1982).

[133] M. Bogdanski, T. Emura, S. N. Ganguli, A. Gurtu, S. Hamada, R. Hamatsu, E. Jeannet, I. Kita, S. Kitamura, J. Kishiro, H. Kohno, M. Komatsu, P. K. Malhotra, S. Matsumoto, U. Mehtani, L. Montanet, R. Raghavan, A. Subramanian, K. Takahashi, and T. Yamagata, Phys. Lett. B **62**, 117 (1976).

[134] S. Banerjee, S. N. Ganguli, A. Gurtu, P. K. Malhorta, R. Raghavan, A. Subramanian, K. Sudhakar, M. M. Agarwal, J. M. Kohli, J. P. Lamba, I. S. Mittra, J. B. Singh, P. M. Sood, Dev Anand, P. V. K. S. Baba, G. L. Kaul, Y. Prakash, N. K. Rao, G. Singh, R. Hamatsu, T. Hirose, S. Kitamura, and T. Yamagata, Zeit. Phys. C **28**, 163 (1985).

[135] M. Lamanna, A. Ahmidouch, R. Birsa, F. Bradamante, A. Bressan, T. Bressani, S. Dalla Torre-Colautti, M. Giorgi, E. Heer, R. Hess, R. A. Kunne, C. Lechanoine-Le Luc, A. Martin, C. Mascarini, A. Masoni, A. Penzo, D. Rapin, P. Schiavon, and E. Tessarotto, Nucl. Phys. B **434**, 479 (1995).

[136] R. Birsa, F. Bradamante, A. Bressan, S. Dalla Torre-Colautti, M. Giorgi, M. Lamanna, A. Martin, A. Penzo, P. Schiavon, F. Tessarotto, M. P. Macciotta, A. Masoni, G. Puddu, S. Serci, T. Niinikoski, A. Rijllart, A. Ahmidouch, E. Heer, R. Hess, C. Lechanoine-Le Luc, C. Mascarini, D. Rapin, J. C. Faivre, F. Perrot-Kunne, J. Arvieux, R. Bertini, R. A. Kunne, F. Iazzi, B. Minetti, T. Bressani, E. Chiavassa, N. De Marco, A. Musso, and A. Piccotti, Phys. Lett. B **302**, 517 (1993).

[137] A. Ahmidouch, R. Bertini, R. Birsa, F. Bradamante, A. Bressan, S. Dalla Torre-Colautti, M. Giorgi, E. Heer, R. Hess, F. Iazzi, M. Lamanna, C. Lechanoine-Leluc, A. Martin, G. Puddu, D. Rapin, R. Schiavon, and F. Tessarotto, Phys. Lett. B **380**, 235 (1996).

[138] M. G. Albrow, S. Andersson/Almehed, B. Bošnjaković, C. Daum, F. C. Erné, Y. Kimura, J. P. Lagnaux, J. C. Sens, and F. Udo, Nucl. Phys. B **37**, 349 (1972).

[139] E. Leader, Phys. Lett. B **60**, 290 (1976).

[140] R. A. Bryan, Phys. Rev. C **24**, 2659 (1981); **30**, 305 (1984); **39**, 783 (1989).

[141] S. Klarsfeld, Phys. Lett. B **126**, 148 (1983).

[142] S. van der Meer, Rev. Mod. Phys. **57**, 689 (1985).

[143] R. Birsa, F. Bradamante, A. Bressan, S. Dalla Torre-Colautti, M. Giorgi, M. Lamanna, A. Martin, A. Penzo, P. Schiavon, F. Tessarotto, M. P. Macciotta, A. Masoni, G. Puddu, S. Serci, T. Niinikoski, A. Rijllart, A. Ahmidouch, E. Heer, R. Hess, C. Lechanoine-Le Luc, C. Mascarini, D. Rapin, H. Catz, J. C. Faivre, F. Perrot-Kunne, J. Arvieux, R. Bertini, R. A. Kunne, M. Agnello, F. Iazzi, B. Minetti, T. Bressani, E. Chiavassa, N. De Marco, A. Musso, and A. Piccotti, Nucl. Phys. B **403**, 25 (1993).

[144] S. M. Bilenky and R. M. Ryndin, Phys. Lett. **6**, 217 (1963).

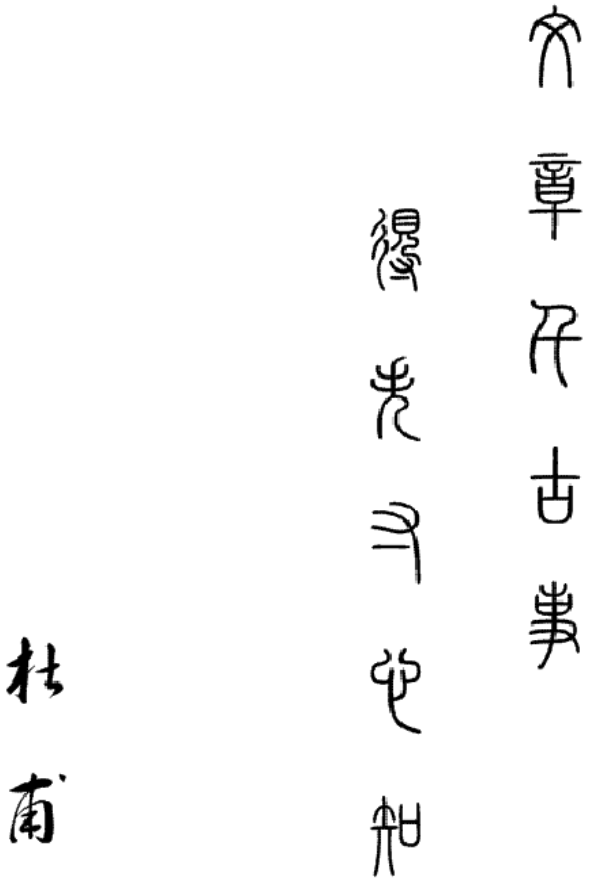

(712 - 770)

“A piece of literature is meant for a millennium,
but its ups and downs are known already in the author’s heart.”
(Adapted version of the translation by C. N. Yang from Du Fu (712 - 770).)

道可道

非常道

老子

(~600 BC - ?)

“A principle that can be stated cannot be an absolute principle.”
(Adapted version of the translation by T. D. Lee from Lao Zi (~600 BC - ?).)

反质子-质子散射的分波分析与自旋观测量

Partiëlegolfanalyse en Spinobservabelen van Antiprotonprotonverstrooiing